UNIVERSITA' DEGLI STUDI DI PARMA

Dottorato di ricerca in Scienze della Terra

Ciclo XXVII

SPECTROSCOPIC ANALYSIS OF TERRESTRIAL ANALOGUES FOR THE INTERPRETATION OF SURFACE COMPOSITION OF ROCKY BODIES IN THE SOLAR SYSTEM.

EFFECTS OF MINERAL MIXING AND PARTICLE SIZE.

Applications to Moon, Mars and implications for Mercury.

Coordinatore:
Chiar.mo Prof. Fulvio Celico

Tutor:
Chiar.ma Prof. Maria Sgavetti

Co-Tutor:
Dott. Cristian Carli
Chiar.mo Prof. Mario Tribaudino

Dottoranda: Giovanna Serventi

“Quando il primo bambino rise per la prima volta, la sua risata si sbriciolò in migliaia di frammenti che si sparpagliarono qua e là. Fu così che nacquero le fate.”

a Tommaso e Riccardo

Index

Note for the reader 5
1. Introduction 6
2. Reflectance spectroscopy 8
2.1 Crystal field theory 8
2.2 Vibrational processes 12
2.3 Reflectance spectrum characteristics 13
2.4 Interpretation of reflectance spectra: the Modified Gaussian Model 14
3. Planetary reflectance spectroscopy: what we know about the surface mineralogy of rocky planets 15
3.1 Moon 15
3.1.1 Lunar surface 15
3.1.2 Plagioclase on the Moon 15
3.1.3 The lunar regolith size 16
3.2 Mercury 16
3.3 Mars 18
4. Terrestrial analogues 20
4.1 Why terrestrial analogues? 20
4.2 Spectral parameters 20
4.2.1 Continuum 20
4.2.2 Band center 20
4.2.3 Band depth 21
4.2.4 Band width 21
4.3 Analysis of reflectance spectra: qualitative vs. quantitative analyses 21
5. Reflectance spectroscopy for the planetary surface interpretation: state of the art 22
5.1 Reflectance spectroscopy of single minerals 22
5.1.1 Plagioclase reflectance spectroscopy 22
5.1.2 Olivine reflectance spectroscopy 23
5.1.3 Pyroxene reflectance spectroscopy 24
5.1.4 Phyllosilicate reflectance spectroscopy 26
5.2 Reflectance spectroscopy of mineral mixtures 27
6. New contributions to plagioclase reflectance spectroscopy for planetary exploration 29
7. Plagioclase-bearing mixtures as terrestrial analogues 31
7.1 Criteria for the choice of the minerals 31
7.2 Sample preparation 31
7.3 Analytical methods 33
7.3.1 Spectroscopic measurements 33
7.3.2 Qualitative analyses 33
7.3.3 Quantitative analyses: the MGM algorithm 34

7.3.3.1 Continuum 34
7.3.3.2 Gaussians 35
8. Spectral reflectance of plagioclase bearing mixtures: 63-125 μm and 125-250 μm mixtures 37
8.1 37
8.1 Spectral characteristics of the end-members: qualitative analyses 37
8.1.1 Fe, Mg end-members 37
8.1.1.1 E1 37
8.1.1.2 E2 38
8.1.1.3 E3 38
8.1.1.4 E4 38
8.1.1.5 E5 38
8.1.1.6 Comparison between mafic end-members 38
8.1.2 PL end-members 39
8.2 Spectral characteristics of the mixtures:qualitative analyses 40
8.2.1 E1+PL1 mixtures 41
8.2.2 E2+PL mixtures 43
8.2.3 E3+PL mixtures 44
8.2.4 E4+PL mixtures 45
8.2.5 E5+PL mixtures 46
8.3 End-member deconvolution 48
8.3.1 Mafic end-members 48
8.3.2 Plagioclase deconvolution 50
8.4 Mixtures deconvolution 52
8.4.1 E1+PL mixtures 52
8.4.2 E2+PL mixtures 55
8.4.3 E3+PL mixtures 57
8.4.4 E4+PL mixtures 59
8.4.5 E5+PL mixtures 61
8.4.6 Comparison between the mixtures 63
9. Spectral reflectance of plagioclase bearing mixtures: <10 μm mixtures 66
9.1 Particle size effects on reflectance spectra 66
9.2 End-members reflectance spectroscopy and deconvolution 66
9.3 Mixture reflectance spectroscopy and deconvolution 68
10. Spectral reflectance of plagioclase-dominated mixtures: 36-63 μm mixtures 70
10.1 Overall spectral shape variations 70
10.2 Quantitative spectral analyses: MGM deconvolution 71
10.2.1 End-members 71
10.2.2 Mixtures 72

10.2.2.1 E5+PL 72
10.2.2.2 E1+PL 74
10.2.2.3 E4+PL 76
10.2.2.4 Comparison 78
11. New contributions to plagioclase reflectance spectroscopy: concluding remarks 79
12. Lessons from the Earth: how to interpret the mineralogy of a planetary surface 81
12.1 The cases of Proclus crater and Nili Fossae 81
12.2 Data 81
12.3 Methods 81
12.3.1 End-member selection 82
12.3.2 SAM 82
12.3.3 MGM 82
12.3.4 Comparison with terrestrial analogues 82
13. Proclus Crater: a "fresh" view into the composition of lunar Highlands 83
13.1 Introduction 83
13.2 Data and methods 83
13.2.1 End-member selection 83
13.3 Spectral classification of Proclus crater 85
13.3.1 Mineralogical mapping 85
13.3.2 Mineralogical interpretation of the units 87
14. Spectral classification and mineralogical characterization of Nili Fossae 93
14.1 Spectral mapping 93
14.1.1 End-member selection 93
14.1.2 SAM classification and rule images 95
14.2 Spectral deconvolution 96
14.2.1 MGM results 96
14.2.2 Gaussian interpretation 98
14.3 Discussion and mineralogical interpretation of Nili Fossae 99
14.3.1 Spectral unit A 99
14.3.2 Spectral unit B 99
14.3.3 Spectral unit C 99
14.3.5 Spectral unit E 100
15. Lessons from the Earth: concluding remarks 101
16. General conclusions and implication for Mercury 103
References 104

Note for the reader

Chapters 4, 7, 8, 9, 10, 11, 12 and 13 have been written in the form of scientific papers.
All the results described in the thesis have been already presented at international conferences.

Chapter 4 from:
Laboratory analysis (reflectance spectroscopy) of terrestrial analogues, published on the Encyclopedia of lunar science, pp. 1-9

Chapters 7 and 8 from:
Spectral variability of plagioclase-mafic mixtures 1): effects of chemistry and modal abundance in reflectance spectra of rocks and mineral mixtures, published on Icarus, 226, 282-298. Paper selected for the "virtual issue on the surface composition of the moon", Icarus
Spectral variability of plagioclase-mafic mixtures 3): quantitative analysis applying the MGM algorithm, published on Icarus, 254, 34-55

Chapter 9 from:
The role of very fine particle size in the reflectance spectroscopy of plagioclase-bearing mixtures: new understanding for the interpretation of the finest sizes of the lunar regolith. To be submitted on Icarus

Chapter 10 from:
Deconvolution of mixtures with high plagioclase content for the remote interpretation of lunar plagioclase-rich regions. Accepted on Icarus

Chapter 12 from:
Proclus Crater: a "fresh" view into the composition of lunar Highlands. To be submitted on Earth and Planetary Science Letters

Chapter 13 from:
*Removal of atmospheric features in near infrared spectra by means of principal component analysis and target transformation on Mars: II. Application. Spectral classification and MGM analysis of Nili Fossae after Surface Atmosphere Separation (SAS).*To be submitted on Icarus

In chapters 7-10 and 12-14 we use acronyms as follows:
Plagioclase: PL
Pyroxene: PX
Orthopyroxene: OPX
Clinopyroxene: CPX
Olivine: OL
Others acronyms have been explicated through the text.

1. Introduction

Among the Solar System's bodies, Moon, Mercury and Mars are at present, or have been in the recent years, object of space missions aimed, among other topics, also at improving our knowledge about surface composition.

The Moon is the natural satellite of the Earth and its surface is composed mainly of plagioclase, pyroxene, and olivine (Papike et al., 1991). Plagioclase, the principal constituent of the lunar surface, is widespread both in nearside and in farside. The lunar surface consists of a regolith layer that covers the underlying bedrocks (McKay et al., 1970); the lunar regolith, due to the absence of atmosphere on the Moon, is different from the regolith formed on the Earth. In particular, it is the result of different processes, e.g., impact of meteoroids and bombardments from the sun and the stars.

Mercury is the innermost planet in the Solar System, and its proximity to the Sun made difficult its exploration. The recent Mercury Surface, Space, ENvironment, Geochemistry, and Ranging (MESSENGER, Solomon et al., 2001) mission, with different kinds of spectrometers onboard, evidenced a global depletion of FeO on the hermean surface. The featureless spectra can thus be explained with the presence of Mg-pyroxene, Mg-olivine and plagioclase (Izenberg et al., 2008; McClintock et al., 2008). A general enrichment in Na has been related to Na-richer plagioclase than plagioclase on the Moon (Evans et al., 2012).

Pyroxenes are widespread on martian surface, as well as iron oxides, while olivine and hydrate minerals have been detected in restricted regions (Bandfield et al., 2002); the recent Compact <reconnaissance Imaging Spectrometer for Mars (CRISM, Murchie et al., 2007) results also showed the presence of locally distributed anorthosites (Carter and Poulet, 2013). Differently from the Moon and Mercury, Mars surface is mainly mafic and oxidized, and characterized by the presence of hydrated minerals and has an atmosphere dominated by CO_2.

Between the techniques to detect planet's mineralogical composition, visible and near-infrared reflectance spectroscopy is a powerful tool, because crystal field absorption bands are related to particular transitional metals in well-defined crystal structures, e.g., Fe^{2+} in M1 and M2 sites of olivine or pyroxene (Burns, 1993). Thanks to the improvements in the spectrometers onboard the recent missions, a more detailed interpretation of the planetary surfaces can now be delineated. However, quantitative interpretation of planetary surface mineralogies could not always be a simple task. In fact, several factors such as the mineral chemistry, the presence of different minerals that absorb in a narrow spectral range, the regolith with a variable particle size range, the space weathering, the atmosphere composition etc., act in unpredictable ways on the reflectance spectra on a planetary surface (Serventi et al., 2014).

One method for the interpretation of reflectance spectra of unknown materials involves the study of a number of spectra acquired in the laboratory under different conditions, such as different mineral abundances or different particle sizes, in order to derive empirical trends. This is the methodology that has been followed in this PhD thesis: the single factors previously listed have been analyzed, creating, in the laboratory, a set of terrestrial analogues with well-defined composition and size.

In the literature, mafic minerals, as well as their mixtures, have been widely characterized from a spectroscopic point of view (Cloutis et al., 1986; Sunshine and Pieters, 1993; 1998; Klima et al., 2007; 2011; Clenet et al., 2011; Isacsoon et al., 2011). On the contrary, plagioclase has been poorly analyzed. However, the recent discoveries about the plagioclase absorption band on the Moon make it fundamental to study plagioclase in more detail.

The goal of the thesis is to improve the knowledge of the composition of planetary surfaces, also implementing spectral libraries with plagioclase-bearing mixtures. In particular, plagioclase with different iron content and mixtures composed with different content of plagioclase and mafic

minerals have been spectroscopically analyzed at different particle sizes and with different mineral relative percentages.
The trends derived from terrestrial analogues here analyzed and from analogues in the literature have been applied for the interpretation of hyperspectral images of both plagioclase-rich (Moon) and plagioclase-poor (Mars) bodies. Important consideration about Mercury can also be proposed in the view of new results from the future missions.

2. Reflectance spectroscopy

Reflectance spectroscopy has become a very valuable tool both in terrestrial and in planetary close range and remote sensing, for the identification of minerals; diagnostic absorption features of rock-forming minerals (e.g., pyroxenes, olivine and plagioclase) are located in the visible and near infrared (VNIR, 400-1300 nm) region of the spectrum. Spectral features in the VNIR are related to the presence of transition elements with partially filled d-orbitals in the mineral crystal structure. Fe is one of the most important transition elements for reflectance spectroscopy.
Reflectance spectral features in the VNIR primarily result from electronic processes, while vibrational processes occur at slightly longer wavelength (Shortwave Infrared, SWIR, 1000-2500 nm). Electronic processes include crystal field (CF) transition, inter-valence charge transfer (IVCT) and oxygen to metal charge transfer. In Section 2.1 and 2.2 we summarize the basic characteristics of the two interaction processes. Particular focus is given to the CF transitions of the principal rock-forming minerals, because they explain the rock-forming mineral absorption bands.

2.1 Crystal field theory

The CF theory can be applied to elements of the first transition series and describes the interaction between the orbital energy level of transitional metal ion with the surrounding, negatively charged anions, called ligands.

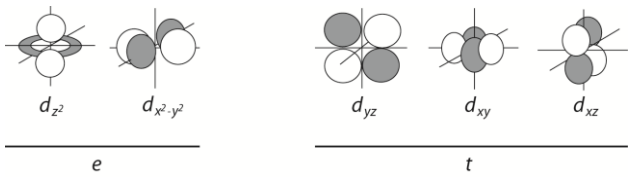

Fig. 2.1 Spatial configuration of the d orbitals. e: double degenerate; t: triple degenerate (from Burns, 1993).

Transition elements are characterized by partly filled d orbitals with the same energy (Fig. 2.1); thus, in an isolated transition metal ion, electrons have the same probability to occupy one of the five d orbitals (1 in Fig. 2.2b). Interactions between the cations and anions of the metal ion produce a lowering of the energy of the metal ion (2 in Fig. 2.2b).When the ion is located in a crystal structure (i.e., octahedral coordination with six ligands situated along the Cartesian axes, Fig. 2.2a; 4 in Fig. 2.2b) the orbitals are repelled by the negative ligands of the coordination environment and the energy of the metal ion is raised. In an octahedral coordination, the e_g orbitals (e: double degenerate; g: the wavefunctions of the orbitals are symmetrical with respect to the center of inversion of the coordination polyhedral) point towards the ligands, and the electrons in these orbitals are repelled to a greater extent than those in t_{2g} orbitals (t: triple degenerate). For this reason, the e_g orbitals are raised in energy relative to the t_{2g} orbitals (5 in Fig. 2.2b2). One consequence of splitting and removal of the degeneracy is that d orbitals are no longer filled with electrons in an arbitrary way but in order of increasing energy, first t_{2g} and then e_g. It is possible to have a high spin-HS configuration if the Hund's rule is obeyed (i.e., orbitals are arranged with parallel spin), while, if the energy of the CF transition exceeds the spin pairing energy, the electrons are displayed in the low energy orbitals, with a low spin-LS configuration (Wildner et al., 2004).
The energy separation between the orbitals is called the CF splitting parameter (Δ); the splitting obeys to a center of gravity rule. In octahedral environments (Δ_0) the three orbitals t_{2g} are lowered by $0.4\Delta_0$, and this stabilizes the metal ion by $0.4\Delta_0$, while the e_g orbital are raised, thus diminishing the stability, by $0.6\Delta_0$ (Fig. 2.2b). The resultant stabilization energy is called CF

stabilization energy (CFSE) and depends on the number of electrons in the stabilized and destabilized orbitals (Burns, 1993; Wildner et al., 2004).

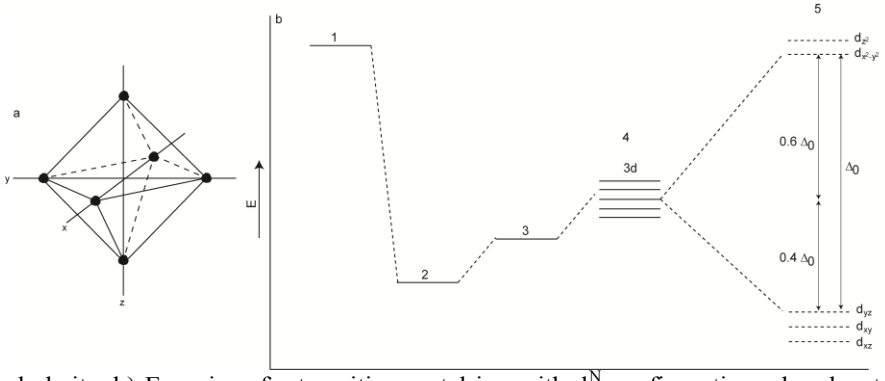

Fig. 2.2a) Octahedral site. b) Energies of a transition metal ion with d^N configuration when located in a octahedral coordination. 1: energy of the free cation; 2: electrostatic attraction cation-anions; 3: repulsion anions-electrons; 4: repulsion anions-3d electrons; 5: splitting of 3d orbitals. Δ_0 is the CF splitting parameter for an octahedral coordination (from Burns, 1993).

The value of Δ is controlled by different factors (Burns, 1993):

1) The type of cation: Δ is higher for trivalent cations than divalent cations;
2) The type of ligands of the coordination polyhedron;
3) The interatomic distance between transition ion and ligands: Δ is inversely correlated to the fifth power of the interatomic distance. In olivine, large Fe^{2+} can replace the small Mg^{2+} causing a relaxing in the lattice parameters and a decrease in the Δ value;
4) The pressure and temperature; and
5) The symmetry of the ligand environment: Δ decreases from an octahedral environment to a tetrahedral one.

Above we have considered high-symmetric octahedral coordination, but most of the rock-forming minerals have low symmetry coordination, and the coordination polyhedrons are distorted (effect Jahn-Teller). This produces additional splitting of the already splitted orbitals (Fig. 2.3).

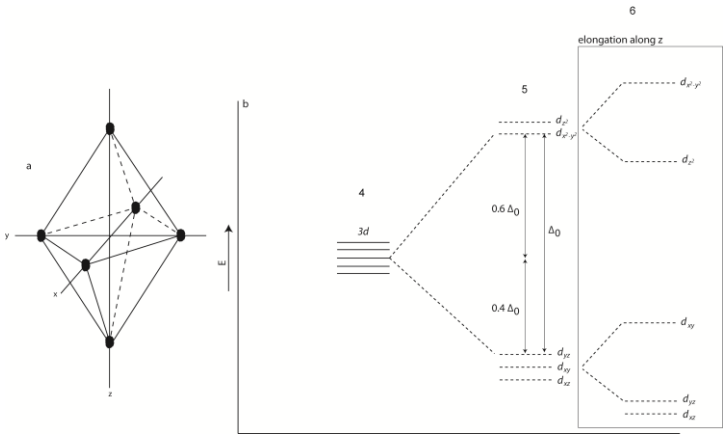

Fig. 2.3 Splitting of the 3d energy levels in a distorted octahedral environment, elongated along the z-axis (from Burns, 1993).

Distorted coordination has important implications for the reflectance spectroscopy of many rock-forming minerals. In particular, a distorted coordination induces cation ordering in many silicates, such as the Fe^{2+} enrichment in the M2 site of pyroxenes, and the different splitting of the 3d

orbitals in highly distorted minerals (i.e., pyroxenes and olivine) produces different absorption bands at different energies, thus permitting the identification of a mineral from its spectrum.
CF splitting is responsible for electronic transitions from the ground d orbital level to excited ones, when an energy corresponding to Δ is absorbed (Burns, 1993). These transitions generate broad absorption bands, and the number of absorption can be theoretically derived from the CF theory. However, experimental electronic absorption spectra of minerals exhibited other bands not predicted from the CF theory: this is explainable by the fact that the transitional metal ion is not a one-electron system but a multi-electrons one.
The total energy of a nd^N electron system is the full Hamiltonian H that includes:

$$H=H_{spher}+H_{ee}+H_{CF}+H_{SO}+H_{SS} \quad (2.1)$$

where H_{spher} is the Hamiltonian in a spherical approximation, H_{ee} indicates the electron-electron repulsion, H_{CF} denotes the CF interactions, H_{SO} represents the spin-orbital interaction, and H_{SS} accounts for the electronic spin-spin interaction.
Orbitals in a nd^N electron system are represented by the Russell-Saunders series that yields the total orbital momentum L and the total spin S, and explains H_{ee}. The spectroscopic terms are labeled ^{2S+1}L and the total degeneracy is the product of the spin multiplicity (2S+1) and the orbital multiplicity (2L+1). Tab. 2.1 shows the spectroscopic ground terms for the d^N configuration and the total degeneracy (Wildner et al., 2004); the ground term can be found following the Hund's rule and it must possess the maximum spin multiplicity. Tab. 2.2 shows the ground and the excited terms of the d orbitals (Wildner et al., 2004).

	m_l								
d^N	-2	-1	0	1	2	$L=\Sigma m_l$	2L+1	$S=\Sigma m_s$	2S+1	Ground term degeneracy
d^1	↑					2	5	½	2	^2D (10)
d^2	↑	↑				3	7	1	3	^3F (21)
d^3	↑	↑	↑			3	7	3/2	4	^4F (28)
d^4	↑	↑	↑	↑		2	5	2	5	^5D (25)
d^5	↑	↑	↑	↑	↑	0	1	5/2	6	^6S (6)
d^6	↑↓	↑	↑	↑	↑	2	5	2	5	^5D (25)
d^7	↑↓	↑↓	↑	↑	↑	3	7	3/2	4	^4F (28)
d^8	↑↓	↑↓	↑↓	↑	↑	3	7	1	3	^3F (21)
d^9	↑↓	↑↓	↑↓	↑↓	↑	2	5	1/2	2	^2D (10)

Tab. 2.1 Ground terms and degeneracy for each d orbital (from Wildern et al., 2004).

d^N, d^{10-N}	Free-ion spectroscopic terms ^{2S+1}L	Deg_{tot}
d^1, d^9	^2D	10
d^2, d^8	^3F, ^3P, ^1G, ^1D, ^1S	45
d^3, d^7	^4F, ^4P, ^2H, ^1G, ^2F, ^3F, ^2D_a, ^2D_b, ^2P	120
d^4, d^6	^5D, ^3H, ^3G, ^3F_a, ^3F_b, ^3D, ^3P_a, ^3P_b, ^1I, ^1G_a, ^1G_b, ^1F, ^1D_a, ^1D_b, ^1S_a, ^1S_b,	210
d^5	^6S, ^4G, ^4F, ^4D, ^4P, ^2I, ^2H, ^2G_a, ^2G_b, ^2F_a, ^2F_b, ^2D_a, ^2D_b, ^2D_C, ^2P, ^2S	252

Tab. 2.2 Free ion spectroscopic terms for all the d^N configuration and total degeneration (from Wildern et al., 2004).

The H_{CF} acts only on the orbital parts of the wavefunctions and not on the spin parts and depends on the coordination of the polyhedral in which the d orbitals are located. Fig. 2.4 shows the CF splitting of the ground term with maximum spin-multiplicity in an octahedral coordination. All the terms listed in Tab. 2.2 undergo CF splitting (Wildner et al., 2004).

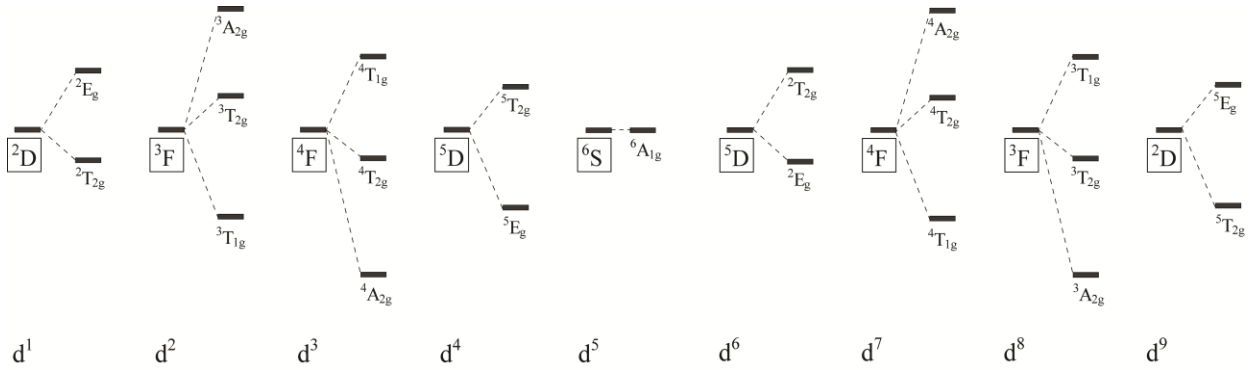

Fig. 2.4 Splitting of the ground terms for all the d^N configurations in an octahedral coordination (from Wildern et al., 2004).

H_{SO} and H_{SS} lead to further splitting of the ^{2S+1}L multiplets of the CF energy levels.
The Tanabe-Sugano diagrams (Fig. 2.5) provide a detailed presentation of the behavior of the energy level in the CF versus its strength, and display the CF levels arising from both ground term and excited terms. Vertical line in Fig. 2.5 d-g represents a change in the ground state and a transition from a high-spin configuration to a low-spin one. In distorted octahedral environments (e.g., pyroxenes) the energy level diagrams are complicated. Generally, the diagrams provide qualitative energy separation between splitted 3d orbitals and give information about the number and position of absorption bands in a CF spectrum. The slope of the energy level in the Tanabe-Sugano diagram can be related to the band width: lines with high, positive slope generate broad absorption bands, while narrow bands correspond to almost horizontal lines (Burns, 1993; Wildner et al., 2004).

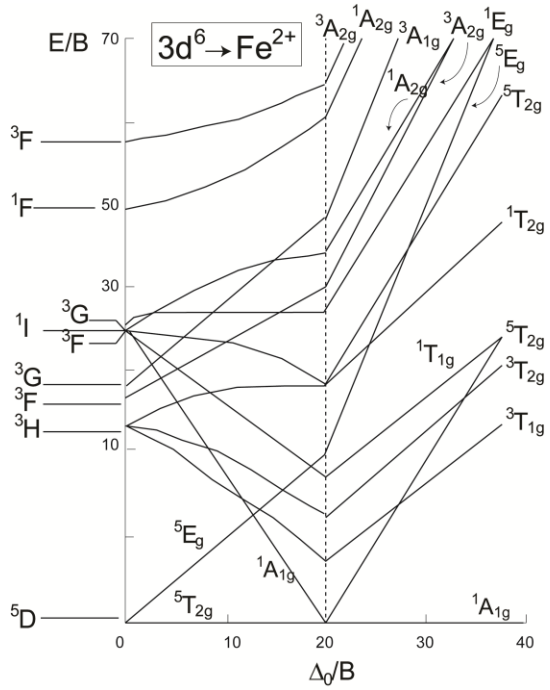

Fig. 2.5 Tanabe-Sugano diagrams for the $3d^6$ configuration (from Burns, 1993); B,C: Racah parameters.

However, a number of the transitions in the diagram have a low probability of occur: a transition follows selection rules. A transition is possible between states that differ in parity (Laporte rule), for example between d and p orbitals; transitions between d-d or s-p orbitals, on the contrary, are

forbidden. The rule can be weakened by (1) the acentricity of the polyhedron, and (2) the vibronic coupling, the coupling of vibrational and electronic wave functions with opposite parities. Transitions also follow the spin-multiplicity rule, where transitions between states with different spin multiplicity are forbidden. Furthermore, transitions representing a change in the electronic configuration involving two electrons are forbidden.
Generally, spin-allowed transitions are more intense than spin-forbidden ones.

2.2 Vibrational processes

When a molecule is placed in an electromagnetic field (light) a transfer of energy from the field to the molecule will be reached when:

$$\Delta E = h\upsilon \qquad (2.2)$$

where ΔE is the difference of energy between the ground and the excited state, h is the Planck's constant and υ is the frequency of the light.
The vibrational energy levels of an ideal harmonic oscillator are shown in Fig. 2.6a, where the horizontal lines are equally spaced. The v=0 $\rightarrow$ v=1 transition is the fundamental and dominates the Infrared (IR) spectrum, while transitions originated from excited levels are weaker. Fig. 2.6b shows the effects occurring when considering anharmonic oscillators: the horizontal lines are not equally spaced, overtone transitions can occur between energy levels differing by two or more vibrational quantum number units and combination vibrations are also possible (Bokobza, 2002).
A molecule containing N atoms has 3N degrees of freedom, where three are translations along the axes and three are due to the rotation of the molecule. Linear molecules have only two rotational degrees of freedom. The remaining vibrational degrees of freedom are 3N-6 in non-linear molecules and 3N-5 in linear molecules.
The vibrational modes can be divided in: (1) v stretching vibration characterized by changing bond lengths, and (2) δ planar bending vibrations, where bond length is unchanged and bond angles change, and occurring at lower frequencies than stretching vibrations. During vibrations, the symmetry of the atomic group can change (asymmetric vibrations) or maintained (symmetric vibrations).

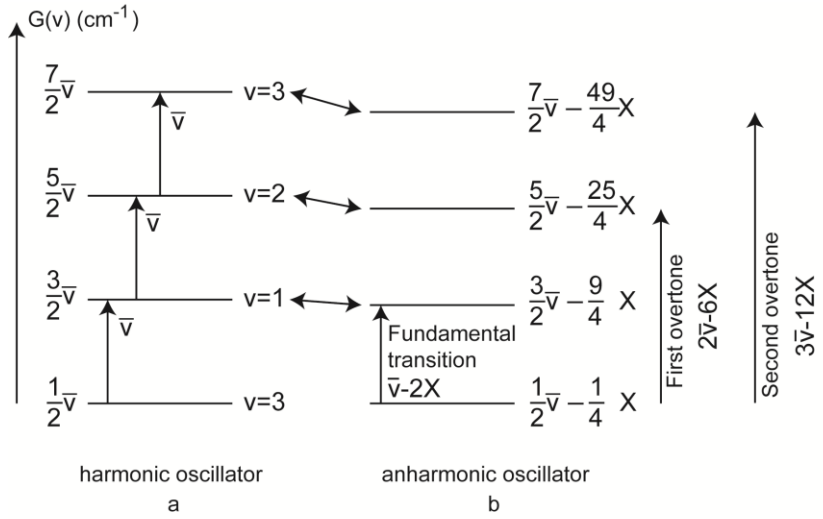

Fig. 2.6 Vibrational energy level diagrams and associated transitions for harmonic (a) and anharmonic (b) oscillators (from Bokobza, 2002)

Fig. 2.7 shows the fundamental vibrations for the H_2O and CO_2 molecules (Bokobza, 2002; Beran et al., 2004).

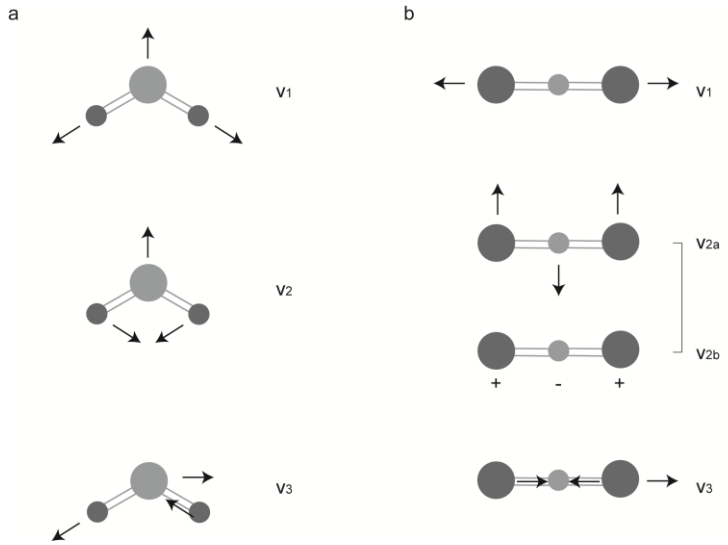

Fig. 2.7 Vibrations of the H_2O (a) and CO_2 (b) molecules. Both molecules are characterized by two stretching vibration, υ_1 symmetric and υ_3 anti-symmetric. υ_2 represents the bending vibration for the water molecule, while the linear CO_2 molecule shows two bending vibrations perpendicular one another, υ_{2a} and υ_{2b}. (from Beran et al., 2004)

2.3 Reflectance spectrum characteristics

Generally, a reflectance spectrum is characterized by a series of absorption bands superimposed onto a continuum, as shown in Fig. 2.8.

The continuum represents the spectrum albedo and reflectance, and can be described by: 1) a mathematical function described with two parameters, the intercept c0 and the slope c1 (as in the Modified Gaussian Model, Sunshine et al., 1990; fig. 2.8a top solid line) and is expressed in the log of the reflectance and as function of the wavenumber; 2) segments that join the spectrum reflectance maxima (as in Clark and Roush, 1984; fig. 2.8b top dashed line).

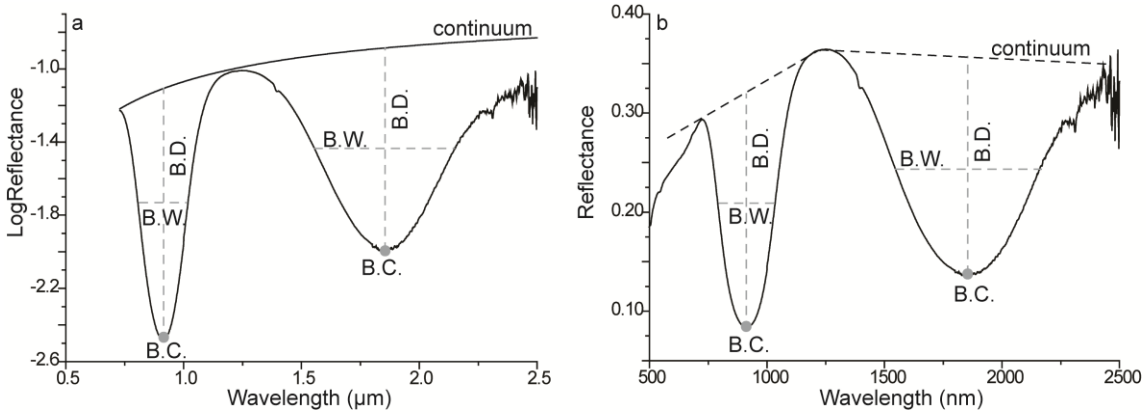

Fig. 2.8 Figure shows spectral parameters that describe a reflectance spectrum. B.C.: band center; B.D.: band depth; and B.W.: band width. a) continuum is a function of wavenumber and expressed as the logarithm of the reflectance. It is described by two parameters, the intercept c0 and the slope c1; b) continuum is considered as the sum of segments that join reflectance maxima (from Serventi et al., 2014).

An absorption band is described using three spectral parameters, band depth (B.D. in fig.2.8), band center (B.C. in fig.2.8) and band width (B.W. in fig.2.8).

The band depth is the distance between the band center and the continuum line and depends on the probability of the light to encounter the spectrally active species (e.g., iron); it gives important information about the spectral species concentration.
The band center is directly related to the transition energy (Burns, 1993) and is characteristic of well-defined mineral phases.
The band width, expressed as the full width at half maximum (FWHM), is related to vibronic processes (Burns, 1993) and is a function of the stability of the transition: bands are narrower if the energy variation in the transition is constant. Band width is also influenced by the superposition of closely-spaced bands from a single transitional metal ion located in a low-symmetry coordination site.
Fig. 2.8 also shows the difference between electronic and vibrational processes: the former produces large and deep absorption bands (at ca. 900 and 1800 nm), while vibrational processes give raise to very narrow bands (at ca. 1400 and 2300 nm).
In literature, several works discussed the band depth and center of mafic minerals, as pyroxenes (Sunshine and Pieters, 1993) and olivine (Sunshine and Pieters, 1998). On the contrary, few data can be found about the plagioclase spectral parameters.

2.4 Interpretation of reflectance spectra: the Modified Gaussian Model

The Modified Gaussian Model (MGM, Sunshine et al., 1990) is a method that resolves spectra in their physical component absorption bands. In electronic absorptions the energy of absorptions is a function of the distortion and the average ligand-ion bond length. In a CF site, the bond length will vary due to random vibrations and variations in the crystal site: the bond length is the random variable for electronic absorptions and is Gaussian distributed. Since the bond length determines the energy of absorption, a Gaussian distribution of bond length can be mapped into a modified Gaussian distribution of absorption energies:

$$m(x) = s * e^{\frac{-(x^n-\mu^n)^2}{2\sigma^2}} \quad (2.3)$$

where n=1 corresponds to the smallest root mean square-RMS residual error when fitting the 900 nm pyroxene absorption band. Interested readers can find further details in Sunshine et al. (1990).

3. Planetary reflectance spectroscopy: what we know about the surface mineralogy of rocky planets

In this section we report a short description about the surface composition of three rocky planetary bodies: Moon, Mercury and Mars. Moon and Mercury are characterized by the absence of atmosphere so that the surface is subject to the space weathering that constantly comminutes, melts and overturns the components of the regolith. In general, the lunar surface is mainly anorthositic and dominated by plagioclase; less is known about the hermean surface mineralogy, but plagioclase is one of the most suitable candidates.

Differently from the Moon and Mercury, Mars is characterized by a relative tenuous atmosphere whose spectral characteristics are contained in remote sensed data of the surface: water, OH^- and $(CO_3)^2$ in minerals absorb in the same spectral region of water and CO_2 in the atmosphere. Primarily, Mars surface is characterized by a mafic composition, even if areas dominated by plagioclase have been recently discovered (Carter and Poulet, 2013), and by the presence of oxides and hydrate mineralogies.

3.1 Moon

3.1.1 Lunar surface

The Moon is one of the most studied planetary bodies across the Solar System and has been widely studied through both telescopic observations from the Earth and remote sensing from orbit.

The lunar surface is characterized by Maria and Highlands. The Maria show basaltic compositions (pyroxenes, Mg-olivine, Ca-plagioclase and opaque) that can be sub-divided in low-Ti, high-Ti and high-Al Maria (Pieters, 1978; Taylor et al., 1991). The Highlands, the principal constituent of the lunar surface, comprise (1) the ferroan anorthosites composed with high plagioclase content and Mg-pyroxene, (2) the Mg-suite characterized by a high $Mg/(Mg+Fe^{2+})$ ratio, and (3) KREEP characterized by a high content of K, P and rare earth elements (Taylor et al., 1991; Taylor et al., 2007).

Silicate minerals, such as orthopyroxene and clinopyroxene, olivine and plagioclase have been recognized and defined as the most important constituents of the lunar surface, associated with oxides and rare apatite (e.g., Papike et al., 1991). Olivine and pyroxene show clear spectral signature and well defined crystal field absorption bands in the VNIR (Burns, 1993), while plagioclase is difficult to recognize, due to very low iron content in its crystal structure.

3.1.2 Plagioclase on the Moon

Lunar crust is composed with a very large anorthositic complex (Warren, 1985) and the plagioclase is widespread on the surface, both in Maria and in Highland regions (Hiesenger and Head, 2006 and references therein). Lunar meteorites, returned sample and remote sensed data, both Earth-based and from orbit, permitted the analysis of the lunar surface mineralogical composition. In particular, several missions spectroscopically measured the lunar surface, including Clementine (McEwen and Pieters, 1997), Kaguya/SELENE (Kato et al., 2008; Ohtake et al., 2008) and Chandrayaan-1 (Pieters et al., 2009; Boardman et al., 2011; Green et al., 2011).

Studying the Apollo samples, it has been observed that a large portion of pristine rocks were characterized by a low Mg/ (Mg+Fe) ratio (Warren, 1985), and classified as ferroan anorthosite (FAN). FAN contains up to 90% plagioclase, and low content of mafic minerals, e.g., orthopyroxene, clinopyroxene and olivine.

Early investigations based on Earth-based telescopic data (Spudis et al., 1984; Bussey and Spudis, 2000; Hawke et al., 2003) revealed featureless, high albedo material inferred to be

associated with shocked anorthosites, because high pressure weakens the plagioclase absorption band (Adams et al., 1979).
Tompkins and Pieters (1999) show the spectral data acquired by the UltraViolet-Visible (UVVIS) camera (0.4-1.0 μm), onboard Clementine mission, from 109 impact craters, with central peaks or peak rings whose composition and mineralogy are expected to reflect deeper crustal compositions. Spectra from Clementine do not show clear absorptions in the 1250 nm region, typical of Fe^{2+} in plagioclase; therefore, the presence of plagioclase has been inferred from the presence of weak or absent mafic absorption bands and high albedo spectra. In general, the authors concluded that the lunar crust is extremely anorthositic, with a plagioclase content ~81%.
In 2007, the Japanese SELENE spacecraft has been launched, carrying onboard the Spectral Profiler (SP), consisting of a VNIR (0.5-2.6 μm) spectrometer with a high spectral resolution of 6-8 nm. The spectrometer detected the presence of an absorption band at ca. 1250-1300 nm, consistent with Fe^{2+} transition in crystalline plagioclase, in central peaks of impact craters (Matsunaga et al., 2008). Based on these data, Ohtake et al. (2009) defined the pure anorthosites (PAN) as regions with more than 98% plagioclase, regions identified in Tycho, Tsiolkovsky and Jackson craters and in Orientale basin (Ohtake et al., 2009). Furthermore, Ogawa et al. (2011) detected spectra of high-Ca pyroxene and plagioclase widely distributed in and around the bright-rayed craters, and Yamamoto et al. (2012) showed the presence of both plagioclase and olivine in the Copernicus crater.
Recently, the Indian Chandrayaan-1 mission, with the Moon Mineralogy Mapper (M^3) imaging spectrometer onboard, analyzed the lunar surface with a very high spectral resolution (spectral range: 405-3000 nm; spectral resolution: 10 nm). Analyzing M^3 results, Cheek at al. (2012; 2013) confirmed the presence of PAN in the Orientale Basin and in Tsiolkovsky crater, and Kramer et al. (2013) recognized PAN, orthopyroxene and olivine in the Schrödinger Basin.
FAN and PAN rocks, composed with plagioclase content >90% and minor amounts of mafic minerals, were probably formed by the crystallization and segregation of plagioclase inside a magma ocean of the Moon, and the remaining liquid may have produced mafic-rich anorthosite (Smith et al., 1970; Wood et al., 1970; Warren, 1985; Brown and Elkins-Tanton, 2009).Knowing the plagioclase abundance is fundamental to understand the origin and evolution of the Moon from the magma ocean model.

3.1.3 The lunar regolith size

The lunar surface consists of a regolith layer that covers the underlying bedrocks, with the exception of steep-sided crater walls, central peaks and lava channels (McKay et al., 1974), as shown by the lunar landings and observations. The lunar regolith, due to the absence of atmosphere on the Moon, is different from the regolith formed on the Earth; it is the result of different processes, e.g., impact of meteoroids and bombardments from the sun and the stars. Lunar regolith is very fine grained (<1cm) and derives from mechanical disintegration of lunar rocks, both basaltic and anorthositic. The average lunar soil grain size is generally between 60 and 80 μm (Papike et al., 1991). However, sizes <10 μm, that comprises ca. 5-20% of the soil, have been recognized and petrologically classified (Laul et al., 1978; 1979; 1980). Coarse sizes of the regolith are very similar in chemistry, while the finest fractions, <10 μm, are different and more feldspathic. A possible explanation can be due to simple comminution processes and the easy of fracturing of plagioclase with respect to mafic minerals.

3.2 Mercury

Mercury is a terrestrial, airless planet, whose surface is composed of fine regolith constantly melted, comminuted, sputtered, vaporized and overturned (Domingue et al., 2009). Mercury is

called the iron planet (Solomon, 2003), due to its large and heavy iron-rich core representing 60% of the total planet's mass or more (Solomon et al., 2001). In contrast with this, spectral evidences suggested the lack of FeO in silicates on hermean surface (Vilas et al., 1984; Vilas, 1985; Vilas 1988; Sprague et al., 1994; Blewett et al., 1997, 2002).

Recently, the Mercury Dual Imaging System (MDIS), on the MESSENGER mission, provided near-global observations of the hermean surface, while the Mercury Atmospheric Surface Composition Spectrometer (MASCS, McClintock and Lankton, 2007) analyzed the 200-1400 nm spectral range with high spectral resolution (an average of 5 nm).

Denevi et al. (2013) recognized different units on the hermean surface on the basis of color and morphology: (1)smooth plains characterized by a low density of impact crater and variable reflectance and slope (from high-reflectance and red slope to low-reflectance and blue-slope), (2) intermediate terrains more cratered than smooth plains with reflectance similar to the global mean, and (3) low-reflectance materials concentrated in crater and basin ejecta and characterized by a reflectance 40% below the global mean and shallow spectral slope.

Spectra from Mercury are characterized by a lower reflectance and a steeper slope with respect to the lunar spectra, probably due either to a different composition or to a different degree of space weathering. Spectra are also characterized by a very low spectral contrast confirming the absence of clearly resolvable absorption bands in the 1000 nm region (Cloutis et al., 2008; McClintock et al., 2008; Solomon et al., 2008). Absorption processes in this spectral region are due to Fe^{2+} in octahedral M1 or M2 sites in silicates (Burns, 1993), like orthopyroxene, clinopyroxene and olivine; therefore, the absence of this absorption structure in the Mercury's surface spectra is generally explained by low-iron content in silicates (Robinson et al., 2008; Blewett et al., 2009).

Nevertheless, spectra from the second MESSENGER's flyby showed a possible CF absorption band at 1100-1200 nm (Izenberg et al., 2008); in previous Earth-based data of Mercury, this feature was interpreted to be due to Fe^{2+} in calcic pyroxene (Warell et al., 2006). The analysis of MESSENGER spectra (Izenberg et al., 2008; McClintock et al., 2008) indicated plagioclase, high-calcium iron-poor pyroxenes, low-iron orthopyroxenes like enstatite, and low-iron olivines such as forsterite, as a mineral assemblage that can explain the featureless spectra on Mercury.

Izenberg et al. (2014) employed a method that recognized four different spectral units, called (1) average, (2) dark blue, (3) red and (4) bright units. The method is based on three spectral parameters, all involving the ratio of spectra with the global mean spectrum to accentuate spectral differences. In particular: (1) average units comprise the majority of the hermean surface; (2) dark blue units show spectra that are darker and bluer than the planetary mean spectrum, and include the areas classified as low-reflectance materials; (3) red unit spectra are characterized by a higher reflectance and a redder slope compared to the planetary mean spectrum, and corresponds to pyroclastic deposits and parts of the smooth plains; and (4) bright units spectra are the brightest and with the highest reflectance values, and are characteristic of the hollows and areas with the highest surface reflectance (fresh impact craters). From the characteristics of each spectral unit, the authors concluded that Mercury is dominated by low-iron minerals and that silicate minerals are Fe-poor (ca. 1.8 wt. % FeO), such as enstatite and plagioclase. The general darkening compared to the Moon is explained by the presence of opaque minerals, intense space weathering and thermal cycling.

The MESSENGER mission also carried onboard the X-ray Spectrometer (XRS, Schlemm et al., 2007) and the Gamma-ray Spectrometer (GRS, Goldsten et al., 2007), that helped to improve the knowledge about the composition of the hermean surface. Stockstill-Cahill et al. (2012) and Weider et al. (2012), relaying on the XRS results, concluded that the hermean surface composition is similar to a terrestrial magnesian basalt, with Mg-rich orthopyroxene and olivine (enstatite and forsterite) and plagioclase, while Evans et al. (2012), analyzing the GRS results,

confirm the low total Fe abundance and the presence of Mg-rich silicates, also suggesting that plagioclase has an albitic composition.
In the future, the BepiColombo mission (Benkhoff et al., 2010) will provide data about the Hermean surface composition in a larger VNIR spectral range (400-2000 nm) than MESSENGER and with high spectral (256 channels with 6.25 nm spectral sampling) and spatial resolutions (100m at Periherm).

3.3 Mars

Telescopic observation and early missions (as Mars Global Surveyor Thermal Emission Spectrometer (TES, Christensen et al., 1992) and Mars Odyssey Thermal Emission Imaging System (THEMIS, Christensen et al., 2004)) gave significant overview of the global surface composition of Mars. Bandfield et al. (2002) detected high-Ca pyroxene in the low-albedo regions while iron oxides dominated the high-albedo regions. The authors also recognized the presence of olivine in well-defined areas and calcic plagioclase in the low-albedo regions; low-Ca pyroxene was recognized in very low concentrations. The Observatoire pour la Minèralogie, l'Eau, les Glaces, et l'Activitè (OMEGA, Bibring et al., 2004) confirmed the mineralogy but also identified secondary minerals, such as phyllosilicates, sulphates and Fe^{3+} O-H phases. OMEGA imaging spectrometer measures radiance in the 0.35-5.2 μm spectral range (Bibring et al., 2004; 2005) and has a spectral resolution of 14 nm. The spectral sampling for the VNIR is 7 nm, and for the SWIR spectrometers is14 nm and 20 nm, respectively. The OMEGA spatial resolution varies between 300 m and 4 km, depending on altitude of observation. Poulet et al. (2007) reports the distribution of minerals using the OMEGA observations in the VNIR. In particular: (1) ferric oxides, widespread all over the surface but mainly in the brightest regions, indicates that Mars surface is oxidized; (2) pyroxenes have been recognized in equatorial and southern low-albedo regions, particularly in Syrtis Major; (3) Mg-olivine has been detected in Nili Fossae, Terra Meridiani, Syrtis Major, Ganges Chasma but also in some low-albedo areas, while Fe-olivine has a very limited distribution; and (4) hydrated minerals are detected only in four areas, Terra Meridiani, Mawrth Vallis, Nili Fossae and Aram chaos. Generally, the low-albedo regions have a pyroxene-rich composition while the bright regions are comparable to anhydrous nanophase ferric oxides. The recognition of hydrate minerals is of extreme importance to trace the past environment on Mars.
Carter and Poulet (2013), using the CRISM results, detected eight sites in the southern highlands of Mars with a spectral signature consistent with iron-bearing plagioclase. The spectra also show vibrational bands typical of hydrated mineralogies.

3.3.1 Hydrated mineralogy on Mars

The presence of hydrated minerals on Mars was suggested on the basis of in-situ analyses, returned meteorites and remote sensed infrared observations, and provides a record of water-related processes. The identification of hydrated silicate with OMEGA is based on the detection of the 1900 nm band due to water of hydration and by metal-OH vibrations at 2200-2400 nm. Phyllosilicates have been detected in very restricted areas, commonly in association with dark deposits and eroded outcrops. In dark deposits, the absorption features suggest the presence of Fe/Mg smectites but no montmorillonite. In the outcrops, Fe-rich clays were recognized.
The formation of clays is controlled by bedrock composition and topography, climate-derived parameters, availability of water, time and kinetics of mineral reactions. In terms of bedrock origin, Fe-rich smectites such as nontronites are typical of the alteration of mafic material such as gabbros or basalts, while the Al-rich phyllosilicate could either indicate a higher alteration or originate from the alteration of more acidic crustal rocks containing Al-rich minerals. Smectites

in the martian surface suggests a contact of igneous minerals with liquid water, with alteration of igneous minerals into clays. Martian clays are likely to record an alteration occurred over geologic timescales with liquid water present at thermodynamic equilibrium. However, the formation of clays on Mars by impact and volcanic hydrothermal activity has been discussed by several authors (e.g., Brown et al., 2010; Ehlmann et al., 2011). Such processes, which do not require liquid water to be stable at the surface, could account for the hydrated silicates identified at least in some specific areas.

4. Terrestrial analogues

4.1 Why terrestrial analogues?

Thanks to the improvements in the recent missions, a more detailed interpretation of the planetary surface can now be delineated. On a planetary surface, several factors such as the mineral chemistry, the presence of different minerals that absorb in a narrow spectral range, the particle size, the space weathering etc., act in unpredictable ways on the reflectance spectra (Serventi et al., 2014). The combined effects of these factors can be directly studied using terrestrial analogues.

Terrestrial analogues can be prepared as a set of synthetic samples with systematically varying compositional and particle size characteristics, in order to analyze separately the different factors, as well as the effects of spectral band superposition and convergence.

The analogues analyzed in this PhD thesis consist of synthetic mixtures of powdered minerals with known composition and known modal abundance, analyzed at different particle sizes, from very fine to coarse, and reflectance spectra of each analogue have been acquired and analyzed.

As stated in section 2.3, a reflectance spectrum is characterized by a series of absorption bands superimposed onto a continuum. The continuum represents the spectrum reflectance and slope.

An absorption band is described using three spectral parameters, band center, band depth and band width; (1) the band center or the band minimum, represents the energy of the transition; (2) the band depth, the distance between band center and continuum, is the probability of the transition; and (3) the band width is related to vibronic processes (Burns, 1993).

Compositional information can be obtained by the band center and band depth: the band center position, related to the energy of the transition, is diagnostic of a particular mineral and of a well-defined crystal site, while band depth gives important information about mineral modal abundance and size.

4.2 Spectral parameters

4.2.1 Continuum

The continuum can be described in terms of reflectance values and slope. Reflectance values shift from negative values to 0: negative values represent strongly absorbing minerals (e.g., iron oxides), while transparent minerals (e.g., plagioclase) are characterized by values close to 0. The spectral slope can be red (wavelengths in the VIS have lower reflectance values than wavelengths in the NIR) or blue (wavelengths in the VIS have higher reflectance values than wavelengths in the NIR). Red slopes may indicate material affected by space weathering (e.g., reflectance spectra from the lunar surface), while blue slope could be representative of slabs of rocks (Carli and Sgavetti, 2011).

4.2.2 Band center

As stated in the previous section, the band center is directly related to the transition energy (Burns, 1993) and is characteristic of well-defined mineral phases. Several papers discussed the band center behavior of mafic minerals, e.g. Sunshine and Pieters (1993; 1998), Klima et al. (2007; 2011); on the contrary, less is known about the behavior of plagioclase absorption band. Generally, band center of single minerals is influenced by the Fe^{2+}content in the mineral crystal structure: a higher content of Fe^{2+} shifts the band center towards longer wavelengths.

Minerals with different chemical composition may produce distinct absorption bands within a narrow spectral range: this is reflected in a so called “composite band” (Serventi et al., 2013), where it is difficult to separate the different minerals (e.g., the pyroxene 900 nm and the olivine 900 nm absorptions, the olivine 1200 nm and the plagioclase absorptions).

4.2.3 Band depth

Band depth depends on the probability of the light to encounter the spectrally active species (e.g., iron) and it gives important information about the spectral species concentration, both as mineral chemistry and as mineral modal abundance in a rock or in a regolith. In literature, several works discussed the band depth of mafic minerals, as pyroxenes (Sunshine and Pieters, 1993) and olivine (Sunshine and Pieters, 1998). Few data can be found about the plagioclase band depth.
Band depth can be influenced by different factors: (1) the iron content in the absorbing phases; (2) the presence of minerals absorbing in the same spectral region; (3) the size of the mineral grains that controls the light path length within the mineral, and, therefore, the probability of encountering the spectrally active species (generally, fining the particle size produces reflectance spectra with high reflectance and reduced spectral contrast, while very coarse sizes can saturate the absorption bands (Clark, 1999), producing a flattening in the absorption band bottom); and (4) the number of absorbing phases. Carli and Sgavetti, 2011, showed how the presence of different active minerals can generate featureless spectra. In particular, the authors shown that increasing the number of minerals the spectral contrast decreases, and in their Fig. 3 they pointed out how the plagioclase band is masked by the other mineral phases even if plagioclase is the dominant phase of the mixture.

4.2.4 Band width

Differently from band center and band depth, the band width is less related to the iron content; however, band width has to be considered in the analysis of a reflectance spectrum.
First of all, electronic processes and vibrational modes can be differentiate from the band width: electronic transitions generate wide absorptions, while vibrational processes produce narrower bands. Furthermore, the band width can be useful to determine the presence of composite bands (e.g., the composite band from orthopyroxene and clinopyroxene is wider than the single pyroxene band).

4.3 Analysis of reflectance spectra: qualitative vs. quantitative analyses

In this thesis, reflectance spectra were first analyzed using ORIGIN® software, and were then deconvolved applying the MGM algorithm. With ORIGIN, we want to qualitatively described the spectral shape variations in terms of reflectance values, slope and absorption characteristics, while applying the MGM algorithm we deconvolve the absorption bands trying to define variation trends for each spectral parameter both vs. the volumetric iron content due to the plagioclase in the mixture and vs. the PL content.

5. Reflectance spectroscopy for the planetary surface interpretation: state of the art

Here we report the general spectral characteristics of mineral phases mainly recognized or expected on planetary surfaces, as well as the spectral effects of mineral mixtures in regolith.

5.1 Reflectance spectroscopy of single minerals

5.1.1 Plagioclase reflectance spectroscopy

Plagioclase contains only low amounts of iron; however, the spectra of plagioclase show absorption bands centered at ca. 8.500 and 4.500 cm^{-1} (1170 and 2200 nm, respectively), with intensities correlated with the iron content (Bell and Mao, 1972; 1973, Hofmeister and Rossman, 1983; Burns, 1993). The bands originate from crystal field transitions in Fe^{2+} substituting Ca^{2+} ions in seven-coordinated sites with average metal-oxygen distance of 250 pm (Bell and Mao, 1972; Adams and Goulland, 1978).

Plagioclase is a solid solution between anorthite (Ca) and albite (Na); Adams (1975) suggested that the wavelength of the absorption band center changes as the plagioclase structure changes through the solid solution series (see Fig. 5.1). Bell and Mao (1972; 1973) demonstrated that plagioclase position shifts as a linear function of increasing concentration of FeO. Fig. 5.1 shows that, in reflectance spectroscopy, plagioclase is characterized by an absorption band between 1100 and 1300 nm: the band reaches the longest wavelength at about An_{65}, while for more calcic sample, characterized by a lower iron content, the center moves towards shorter wavelengths (Adams and Goulland, 1978).

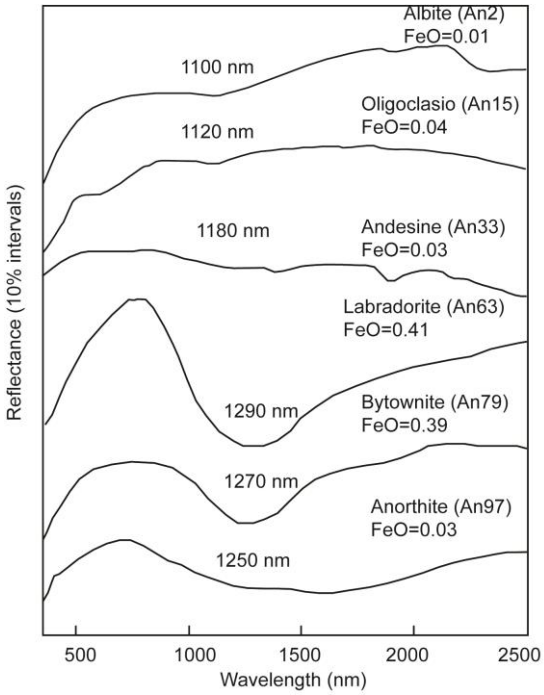

Fig. 5.1 Reflectance spectra of a set of plagioclase with different An and Fe content (from Adams and Goulland, 1978). The plagioclase band deepens and shifts towards longer wavelengths from An_2 to An_{63}, while for Ca-richer composition, the band is shallower and shifted towards the VIS region. In particular, the An_{63} shows the deepest and at longest wavelength absorption band.

In the recent years, Cheek et al. (2011) demonstrated how in a set of synthetic An_{85} plagioclase with different iron content, the 1250 nm depth increases with increasing the iron content, till a maximum value (ca. 0.4 wt.% FeO) after which band depth remain quite constant (Fig. 5.2).

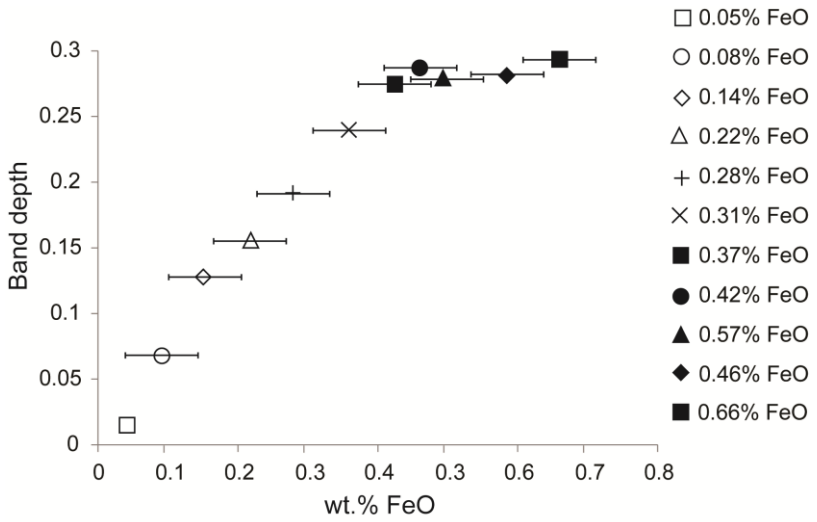

Fig. 5.2 The figure shows that the plagioclase absorption deepens with increasing the iron content till ca. 0.4 wt.% FeO, while for FeO>0.4 wt.% the band depth is quite constant (from Cheek et al., 2011).

5.1.2 Olivine reflectance spectroscopy

Olivine structure contains two divalent cations in two six-fold (octahedral) coordination sites with different symmetries: the M1 site resembles a tetragonally elongated octahedron, while the larger M2 site approximates a trigonally distorted octahedron. The different symmetry of the two sites produces contrasting crystal field transition in Fe^{2+} ion, thus generating differences in the absorption spectra.

Olivine has an orthorhombic symmetry and when the light is transmitted through oriented crystal structure it produces three different spectral profiles. The α and β polarized spectra have absorption maxima near 11.000 and 8.000 cm^{-1}, while the γ spectrum band maxima are at 9.300 and 8.000 cm^{-1}. In the forsterite-fayalite series, absorption maxima shifts to shorter wavelengths with decreasing iron content, reflecting a diminished metal-oxygen distance in Mg-olivine. The absorption bands at 11.000 and 8.000 cm^{-1} (that correspond to a wavelength of 900 and 1250 nm, respectively) are assigned to the split of the e_g orbitals of Fe^{2+} in M1 site, while the 9.300 cm^{-1} band (corresponding to 1075 nm) represents a transition to the e_g orbitals of Fe^{2+} in M2 site.

Fig. 5.3 indicates the principal transition in the spectra of fayalite.

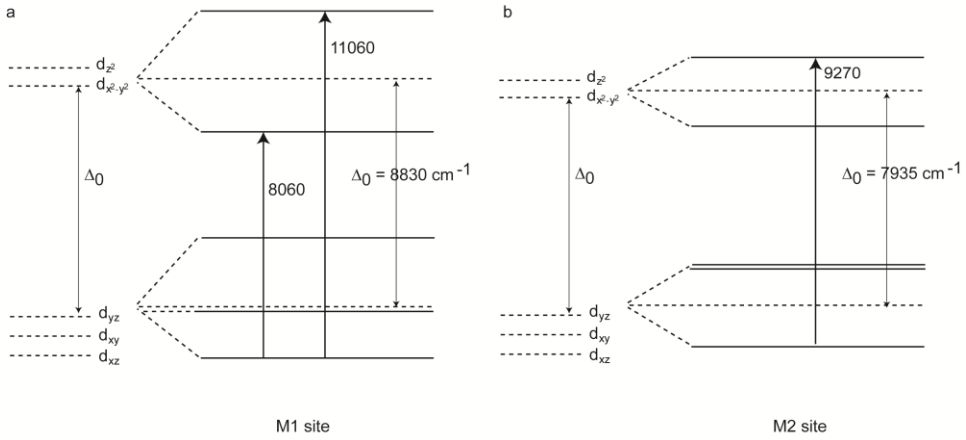

Fig, 5.3 a) Fe^{2+} crystal field transition in olivine M1 site; b) Fe^{2+} crystal field transition in olivine M2 site (from Burns, 1993).

In reflectance spectroscopy, olivine is characterized by a complex, broad absorption centered at ca. 1050 nm (Fig. 5.4); MGM deconvolution resolves the olivine absorption with three absorptions due to the Fe^{2+} transitions in the olivine M1 and M2 sites at ca. 900, 1000 and 1200 nm (Burns, 1993; Sunshine et al., 1998; see arrows in Fig. 5.4). Olivine band center shifts towards longer wavelengths with increasing the iron content (from forsteritic to fayalitic compositions).

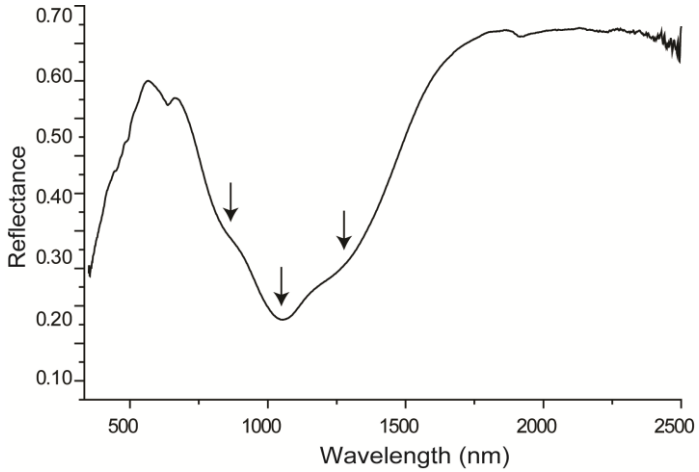

Fig. 5.4 Reflectance spectrum of olivine Fo_{90}. Olivine is characterized by a broad absorption band centered at 1050 nm that can be fitted with three different bands (see arrows in Fig.).

5.1.3 Pyroxene reflectance spectroscopy

Depending on the crystal structure and on the Mg-Ca-Fe content, pyroxenes can be divided in orthopyroxene (from enstatite to ferrosilite) with orthorhombic symmetry, and clinopyroxene, with monoclinic symmetry (where Mg is substituted by Ca).

Pyroxenes, like olivine, contain two coordination sites, M1 and M2, with different symmetries, but differently from olivine, Fe^{2+} shows a strong cation ordering so that there are major compositional variations of VNIR spectra. The crystal structure of pyroxene is characterized by single chains of corner-sharing [SiO_4] tetrahedral, that share two of its oxygen with adjacent tetrahedral (bridging oxygen); bridging and non-bridging oxygens constitute the ligands of the coordination polyhedral of cations in M2 very distorted sites. The M1 site, composed only of non-bridging oxygens, is only slightly distorted from octahedral symmetry and cations are not centrally located.

In orthopyroxenes, Fe^{2+} shows strong preferences for the M2 coordination site; in clinopyroxenes, Fe^{2+} ions fill the Ca vacancies in M2. The crystal field spectra of orthopyroxenes and subcalcic pyroxenes are dominated by the transitions of Fe^{2+} in the M2 site. In high-Ca pyroxenes, where Ca occupies the M2 site, Fe^{2+} is located in the less distorted M1 site. The crystal field spectrum of hedenbergite shows two absorptions at 10.200 and 8.475 cm^{-1} (980 and 1180 nm, respectively), due to the splitting of the t_{2g} orbitals. When Fe^{2+} fills the vacancies left by Ca in M2, additional, more intense bands are produced at 9.600 and 4.400 cm^{-1} (1040 and 2270 nm).

Regarding orthopyroxene, the α polarized spectrum has an absorption maximum near 10.700cm^{-1} (930 nm), β spectrum at 11.100cm^{-1} and between 5.400-4.900 cm^{-1}(900 and 1850-2040 nm), while the γ spectrum band maxima are at 11.000, 8.500 and 5.300 cm^{-1}(900, 1170 and 1890 nm, respectively). The 10.700-11.000$cm^{-1}$and 4.900-5.400cm^{-1} band intensities show a correlation with the Fe^{2+} concentration.

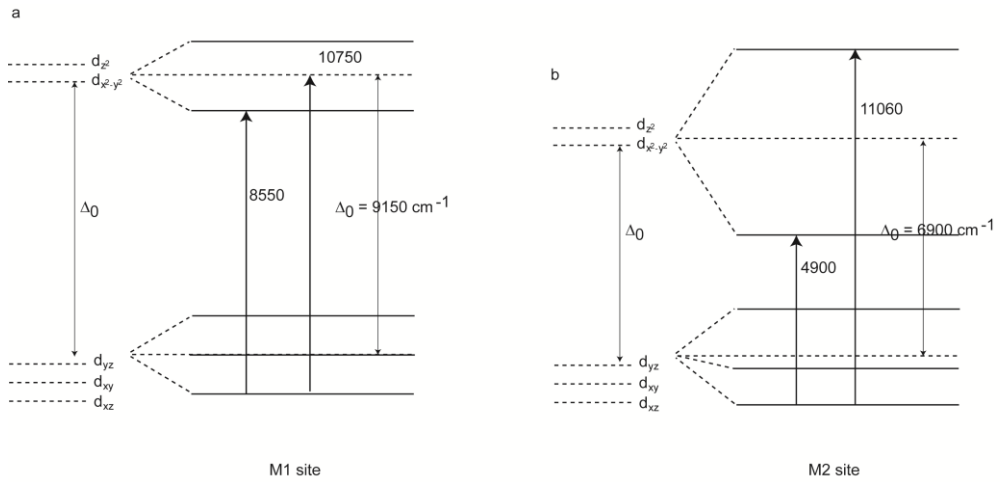

Fig. 5.5 a) Fe^{2+} crystal field transition in orthopyroxene M1 site; b) Fe^{2+} crystal field transition in orthopyroxene M2 site (from Burns, 1993).

It follows that pyroxene spectroscopy shows a great variability; Fig. 5.6 shows the reflectance spectra of three pyroxenes with different composition:

1) OPX is an orthopyroxene, En_{82} with 10.67 wt.% FeO (solid, black line in Fig. 5.6);
2) CPX-a is the spectrum of a clinopyroxene, En_{44}-Wo_{50} with 2.61 wt. % FeO (grey line in Fig. 5.6); and
3) CPX-b represents a clinopyroxene, En_{33}-Wo_{49} with 10.0 wt.% FeO (dotted, black line in Fig. 5.6).

Generally, orthopyroxene and type b-clinopyroxene are characterized by two absorption bands, b1 and b2, due to the Fe^{2+} transition in pyroxene M2 site. The figure shows that increasing the Ca content, band centers shift towards longer wavelength (e.g., Band I shifts from 900 to 1050 nm, and Band II from 1850 to 2300 nm). Also a higher FeO% content shifts the band center towards longer wavelengths (Burns, 1993; Sunshine and Pieters, 1993).

On the other hand, type a-clinopyroxene is characterized by two absorption bands at 1050 (Band I) and 1250 nm (Band III) due to the Fe^{2+} transition in the pyroxene M1 site (M2 site is occupied by Ca). Clinopyroxene are also characterized by an absorption band at 700 nm, due to the Fe^{2+}-Fe^{3+} IVCT.

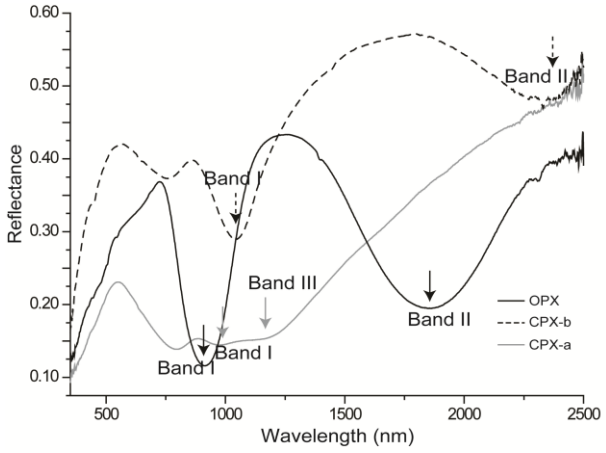

Fig. 5.6 Reflectance spectra of three pyroxene with different composition; OPX is an orthopyroxene while CPX are two clinopyroxene with different iron content.

5.1.4 Phyllosilicate reflectance spectroscopy

Phyllosilicates are composed of octahedral sheets bound to tetrahedral sheets. While kaolinite have a 1:1 ratio of tetrahedral to octahedral sheets, all the other phyllosilicates are characterized by a 2:1 ratio. The octahedral site contains a larger M1 site, with two OH ions positioned on adjacent sides of the octahdera, and two smaller M2 sites, with two OH on the opposite sides of the octahedral.

Here we focus on: (1) the smectite group, montmorillonite, nontronite and Fe-smectite, dioctahderal and with the M2 site dominated by trivalent cations Al^{3+} or Fe^{3+} , and (2) chamosite, belonging to the chlorite group, a trioctahedral mineral where M site is occupied by Fe^{2+}.

Electronic absorptions characterize the 500-1200 nm spectral region and, in particular, bands centered between 800 and 1200 nm are due to Fe^{2+} transitions.

Overtones and combination of modes characterize the longest wavelength (1400-2500 nm). In particular: smectite, nontronite and montmorillonite have the strongest water overtones near 1410 nm and water combination bands near 1920 nm. As shown in Ehlmann et al. (2008; and references therein) the absorption at 1400 nm (due to the OH stretching) depends on the octahedral cations present in the hydrated mineral crystal structure. The stretching occurs at 1430 nm, at 1410 nm and at 1380-1390 nm if the cation is Fe, Al or Mg, respectively. H-O-H combination stretching and bending vibrations occur near 1920 nm and 1970 nm, respectively (Bishop et al., 2008). Weak combination bands have been detected at ca. 2000 nm for adsorbed water in hydrated minerals.

Strong OH combination bands are also present in the 2200-2500 nm spectral region, and, as the 1400 nm absorption, their position is a function of the octahedral cation composition. In general, the OH combination bands occur at 2170-2210nm , 2290-2310 nm and 2320-2340 nm if Al, Fe^{3+} and Mg are in the octahedral sites, respectively, Al,Fe-OH combination bands occurs at ca. 2240 nm, while if the cation is the Fe^{2+} the band is centered at 2350-2370 nm. Additional bands between 2400nm and 2500 nm has been interpreted by Bishop et al. (2002) as due to further OH stretching and bending.

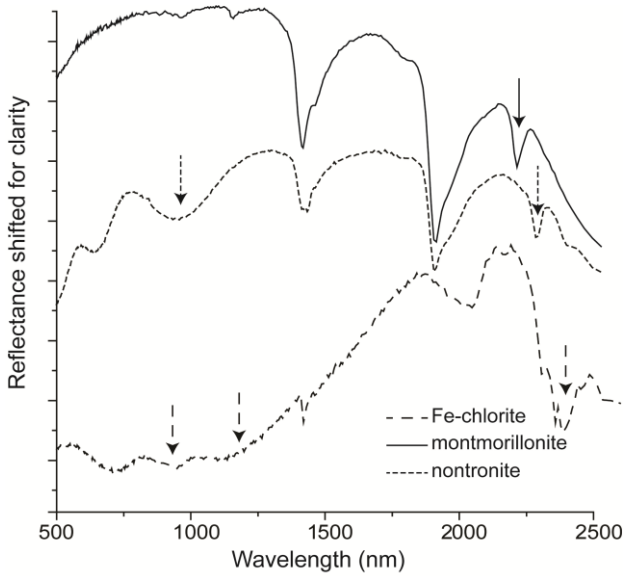

Fig. 5.7 Figure shows the reflectance spectra of three different hydrated minerals (spectra from USGS library)

Fig. 5.7 shows the reflectance spectra of chamosite, nontronite and montmorillonite. In particular: (1) nontronite (narrow-dotted line in Fig. 5.8) is characterized by an absorption band at ca. 900 nm and by vibrational bands at 1400, 1900 and 2300 nm, (2) montmorillonite (solid line in Fig.

5.8) shows vibrational bands at 1400, 1900 and 2200 nm, and (3) chamosite (large-dotted line in Fig. 5.8) have strong absorptions from 1000 to 1200 nm and vibrational bands at 1400, 1900 and 2350 nm.

5.2 Reflectance spectroscopy of mineral mixtures

Reflectance spectroscopy in the laboratory is different from the remote sensed spectroscopy: in the laboratory the analyzed sample has an area generally less than 1 cm^2 while, from orbit, the analyzed area is a pixel with a ground dimension that depends on the spectrometer's field of view and the orbit distance. A pixel can comprise distinct subareas each having single mineral composition. In this case, remotely obtained reflectance spectra are the sum of the spectral contributions of each material contained in the distinct areas. However, a pixel can also, and often, consists of more homogeneously distributed mixtures of different minerals, said to constitute an intimate mixture. In this case the spectral properties of the various minerals combine in an unpredictable way. For this reason, it is fundamental to analyze in the laboratory the spectral characteristics of intimate mixtures of rock-forming minerals, where each mineral component is randomly distributed within the field of view of the instrument.

Spectra of mafic mineral mixtures have been widely studied and reported in the literature.

Nash and Conel (1974) analyzed binary and ternary mixtures of plagioclase, pyroxene and ilmenite and concluded that (1) ilmenite strongly reduce the overall albedo and absorption band depth, (2) the 1000 nm pyroxene band depth is proportional to the pyroxene concentration, while its position does not change when mixed with plagioclase or ilmenite, and (3) the plagioclase band is weak and undistinguishable if plagioclase content is less than 75%.

Cloutis et al. (1986) analyzed mixtures composed of orthopyroxene and olivine to define the correlations between spectral parameters and mineralogical properties. In particular, the authors demonstrated that the area ratio for the 1000 and 2000 nm bands is sensitive of the mineral abundance, while the band position of the 1000 nm band can be utilized to determine both the mineral abundance and the molar iron content of olivine and orthopyroxene (see Fig. 5.8).

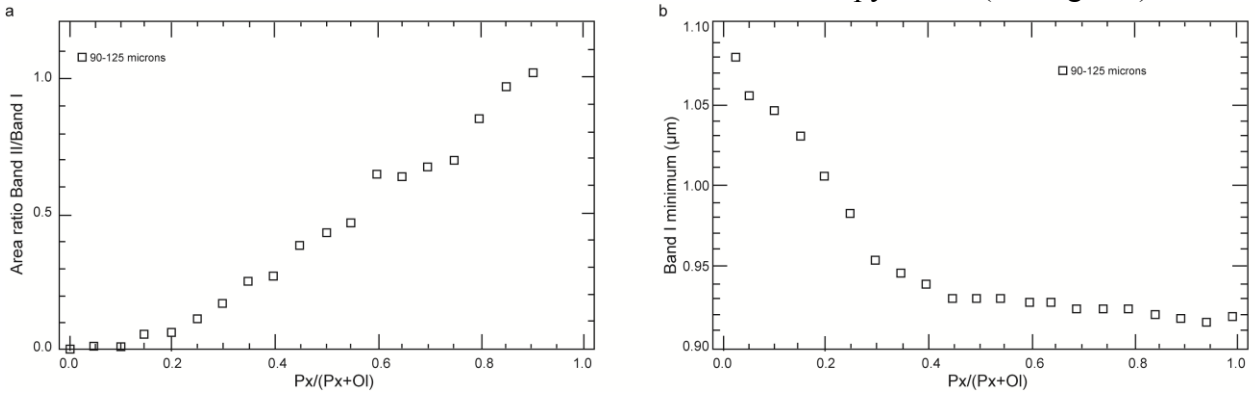

Fig. 5.8 The figure shows the behavior of the band area ratio and of the band minimum vs. the pyroxene content (from Cloutis et al., 1986). a) Band ratio increases as pyroxene content increases; b) band I shifts towards shorter wavelengths with increasing the pyroxene content.

Crown and Pieters (1987) investigated the spectral behavior of plagioclase-pyroxene mixtures, and observed that plagioclase can be detected as a flattening of the pyroxene reflectance maximum around 1300 nm, while to recognize a distinguishable absorption band at least 85% plagioclase is needed.

Sunshine and Pieters (1993) analyzed spectra of orthopyroxene and clinopyroxene as a function of modal abundance using the MGM. The results indicate that systematic changes in relative band strength are logarithmic function of modal abundances (see Fig. 5.9), while the band centers

and band widths of the two components are unchanged (on the contrary, the composite band position move to longer wavelengths with increasing clinopyroxene abundance). The authors also demonstrated that band center, band width and relative band strength are independent of particle sizes.

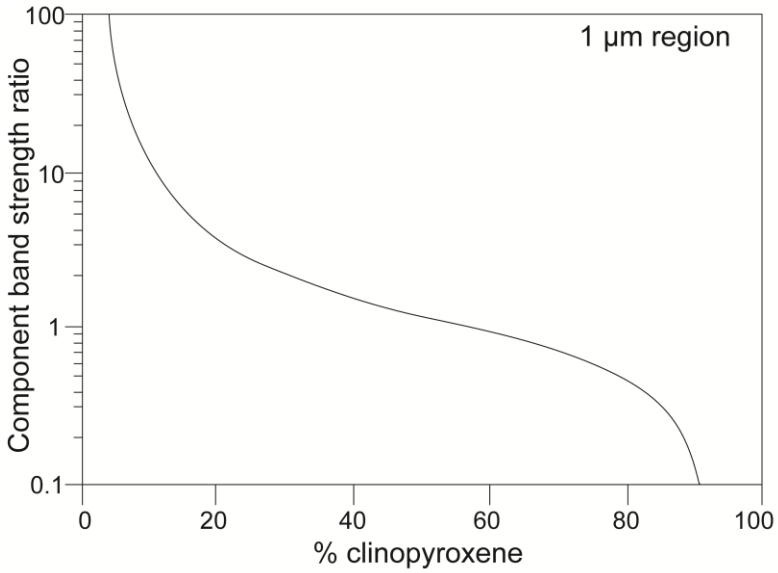

Fig. 5.9 The figure shows how the band strength changes as a logarithmic function of the modal abundance (from Sunshine and Pieters, 1993).

After the recent discoveries on the Moon, plagioclase has been studied in more detail. Cheek and Pieters (2014) analyzed plagioclase-rich mixtures with varying content and composition of olivine, pyroxene and very high-Mg spinels and demonstrated that plagioclase can significantly contribute to reflectance spectra if strongly absorbing minerals are present in low abundances, particularly in mixtures with pyroxene. In their paper, a plagioclase and six non-plagioclase end-members (one forsteritic olivine, one intermediate olivine, a orthopyroxene, a diopside and two Mg-spinels) have been selected at the 45-75 µm particle size. Non-plagioclase minerals have been mixed with plagioclase in different proportion: in plagioclase dominated mixtures, non-plagioclase minerals vary from 2%, 5%, 7% to 10% , while in non-plagioclase dominated mixtures, non-plagioclase minerals vary from 15%, 20% to 50%. The authors conclude that: 1) 2% orthopyroxene is distinguishable from plagioclase, while diopside minimum content is 5%; 2) olivine is distinguishable from 5%; 3) mixtures with olivine<5% and diopside<5% may be indistinguishable; 3) in mixtures with spinels, the detection of plagioclase depends on the iron content in spinel: iron-rich spinel significantly subdue plagioclase absorption; and 4) plagioclase is recognized in mixtures with spinels more than 15%, while plagioclase results in only a spectrum flattening in mixtures with orthopyroxene>10% and in a broadening of the 1000 nm band in mixtures with olivine>10%.

6. New contributions to plagioclase reflectance spectroscopy for planetary exploration

Plagioclase is an important rock forming mineral that has been often considered a featureless, transparent phase in studies of VNIR reflectance from planetary surfaces. The presence of plagioclase has been often associated to high albedo, featureless spectra, and explained as shocked plagioclase. Moreover, although it was considered one of the principal mineralogical component of the featureless reflectance spectra of different Mercury and Moon terrains, few studies are reported exploring the influence of Fe^{2+} absorption band in plagioclase on the more evident mafic absorption bands (Nash and Conel, 1974; Crown and Pieters, 1987; Cheek and Pieters, 2014).

Recently, as explained is Section 3.1.2, the improvements in the missions with spectrometers characterized by a very high spectral resolution permitted the detection of an unique absorption band centered in the 1200-1300 nm spectral region, due to the Fe^{2+} transition in crystalline plagioclase.

The recent identification of a well-defined absorption band at 1250 nm on the lunar surface, interpreted as indicative of the presence of crystalline plagioclase, makes it necessary to explore in detail the spectral behavior of plagioclase.

In particular, it is fundamental to analyzed the behavior of plagioclases with increasing iron content when mixed with mafic, iron richer and more absorbing minerals, to understand (1) how changes the plagioclase absorption band with increasing the iron content, (2) if plagioclase can be recognized when mixed with mafic minerals, (3) what is the detection limit under which plagioclase cannot be detected, (4) what happen when different minerals (e.g., plagioclase and olivine) absorb in the same spectral range, (5) what is the detection limit of mafic mineral, when plagioclase content is very high, and (6) what effects produce different particle sizes on the plagioclase absorption band.

Here, we propose a detailed study of plagioclase, where plagioclase with variable iron content (from 0.1 to 0.5 wt.% FeO) has been mixed with different mafic minerals. The plagioclase content in mixtures ranges between 20-99%, and the mixtures have been prepared at four different particle size, <10 μm, 36-63μm, 63-125μm and 125-250 μm. In this thesis the points discussed above are approached and the results are object of 6 published and submitted papers, the extended abstract of which are reported in the following chapters:

1) in chapter 7 selection and preparation of the mixtures as well as the methodology are described (from Serventi, G., Carli C., Sgavetti, M., Ciarniello, M., Capaccioni, F., Pedrazzi, G.: 2013. *Spectral variability of plagioclase-mafic mixtures 1): effects of chemistry and modal abundance in reflectance spectra of rocks and mineral mixtures*. Icarus, 226, 282-298; Serventi, G., Carli C., Sgavetti, M. :2015. *Spectral variability of plagioclase-mafic mixtures 3):quantitative analysis applying the MGM algorithm.* Icarus, 254, 34-55);
2) mixtures with plagioclase ranging between 20-90%, 63-125 μm, 125-250 μm, and <10 μm, have been analyzed in chapter 8 and 9 (from Serventi, G., Carli C., Sgavetti, M., Ciarniello, M., Capaccioni, F., Pedrazzi, G.: 2013. *Spectral variability of plagioclase-mafic mixtures 1): effects of chemistry and modal abundance in reflectance spectra of rocks and mineral mixtures*. Icarus, 226, 282-298; Serventi, G., Carli C., Sgavetti, M. :2015. *Spectral variability of plagioclase-mafic mixtures 3):quantitative analysis applying the MGM algorithm.* Icarus, 254, 34-55; Serventi, G., Carli, C., Sgavetti, M. *The role of very fine particle size in the reflectance spectroscopy of plagioclase-bearing mixtures: new understanding for the interpretation of the finest sizes of the lunar regolith.* To be submitted on Icarus); and

3) chapter 10 describes mixtures with PL content ranging between 90-99% (from Serventi, G., Carli C., Sgavetti, M. *Deconvolution of mixtures with high plagioclase content for the remote interpretation of lunar plagioclase-rich regions.* Accepted on Icarus).

At the same time, it is necessary to understand how terrestrial analogues can be used for the mineralogical interpretation of planetary surfaces. In chapter 11 has been described the followed methodology, while in chapter 12 and 13 results from Proclus crater (from Serventi, G., Carli, C., Sgavetti, M. *Proclus crater: a fresh view into the composition of lunar Highlands.* To be submitted on Earth and Planetary Science Letters) and from Nili Fossae (from Serventi, G., Carli, C., Sgavetti, M. Geminale, A., Grassi, D., Altieri, F., Orosei, R. *Removal of atmospheric features in near infrared spectra by means of principal component analysis and target transformation on Mars: II. Application. Spectral classification and MGM analysis of Nili Fossae after Surface Atmosphere Separation (SAS).*To be submitted on Icarus), respectively, have been reported.

7. Plagioclase-bearing mixtures as terrestrial analogues

7.1 Criteria for the choice of the minerals

We spectrally analyzed mixtures composed with different content of PL and mafic minerals; PL with increasing iron content have been chosen, following the suggestion from Taylor et al. (2009).Taylor et al., 2009 suggested that lunar magma ocean cumulates, including PL cumulates, are composed of at least 90% An_{90-95}PL. These anorthosites were called FAN (Warren et al., 1985), contain about 3.5 wt.% total FeO content, less than highland FeO content (3-8 wt.% FeO), and the iron content in PL is supposed to be less than 0.1 wt.%. The authors also modeled PL crystallization starting from a melt, for which a FeO Kd PL/melt of 0.03 was considered. They obtained the crystallization of a PL with 0.42 wt.% FeO, in disagreement with the typical value of 0.1 wt.% observed in highland PL. Observing the FeO behavior in terrestrial anorthosites affected by sub-solidus re-equilibration during metamorphism, the authors suggested a similar type of reaction in lunar rocks, made possible by greater heat and slower cooling conditions on the Moon with respect to the Earth; as a consequence, FeO wt.% in anorthitic PL may differ from the original composition.

According to these observations, further supported by iron rich PLs found in other lunar areas, PL compositions with more than 0.1wt.% FeO were considered in this PhD thesis.

To reproduce a plausible PL-mafic mineral assemblage, we consider that on the Moon, areas rich in PL are associated to the presence of mafic minerals, e.g. OPX, CPX and OL. Moreover lunar samples have a mineralogical variability which includes also the norite and gabbronorite with amount of OL (see Lucey et al., 2006, and references therein).

On the other hand, the analysis of MESSENGER spectra (Izenberg et al., 2008; McClintock et al., 2008) indicated the possible presence of PL, high-calcium iron-poor PX, low-iron OPXs, like enstatite, and low-iron OLs such as forsterite, a mineral assemblage that was assumed as a possible explanation for the featureless spectra on Mercury.

On the basis of these considerations, for our mixtures we selected mafic minerals with low iron content.

7.2 Sample preparation

Separate end-member minerals were obtained from samples of two layered intrusions (Bjerkreim Sokndal and Stillwater Complex) and from a peridotitic sample (Arizona). The chemistry of the rock forming minerals was determined by electron microprobe analyses with a CAMECA SX50 (EMP) at the microprobe laboratory of C.N.R.-IGG (Consiglio Nazionale delle Ricerche, Istituto di Geoscienze e Georisorse), Padova, to define the most useful compositions. For further details about the starting rock, e.g., geological setting, composition and microprobe analyses, please refer to Pompilio, 2005, and to Carli, 2009.

The selected rock samples were first crushed to a coarse particle-size class <2.00 mm, in order to preserve the original rock composition in powdered samples. The powders were then quartered and each fraction was ground to smaller particle-size classes. In particular, we have considered two particle-sizes, <250 μm and <125 μm. Each powder particle-size class was then quartered again and half material was then sieved into two size ranges: 125-250 μm and 63-125 μm. These particle sizes have been chosen in order to avoid problems arising when dealing with both very fine particles (e.g. coating processes) and coarse ones (e.g. band saturation effects).

From these particulate samples, three PLs with different iron content and five different mafic compositions with increasing OL amounts were separated, using a Frantz Isodynamic Magnetic Separator at the Department of Physics and Earth Sciences, University of Parma. In Table 7.1, the applied amperage, removed minerals and new samples obtained during magnetic separation are shown.

Samples	Applied Amperage (A)	Minerals removed	New samples
Ultramafic rock 1	0.3	Opaques	OPX+Ol (E2)
	1.4	PL	
Ultramafic rock 2	0.3	Opaques	CPX+OPX+OL (E3)
	1.4	PL	
Ultramafic rock 3	0.3	Opaques	
Anorthosite	1.4	CPX+OPX+Zoisite	PL (PL3)
Gabbronorite	1.4		CPX+OPX (E1)
			PL (PL2)
Melanorite	1.4	OPX+Opaques+Biotite	PL (PL1)
Norite	0.3	PL	OPX (E5)

Tab. 7.1 Table shows the starting compositions, the applied amperage and the final samples obtained with the Frantz Isodynamic Separator.

Part of the new end-members have been reduced to finer particle size, 36-63 µm. The selected PL phases include: an iron-poor PL (PL1: An_{45}, with 0.1 wt.% FeO), a medium-iron (PL2) and an iron-rich (PL3) PL (both An_{80}, with 0.36 and 0.5 wt.% FeO, respectively). PL1 (An_{45}) is a more sodic PL than PL2 and PL3 (An_{80}). Adams and Goulland (1978) analyzed PL with different An content but also with a variable iron content. The authors shown that the PL with the position at the highest wavelength is PL with An_{65} (see section 5.1.1); however, it is also clear that the An_{65} is also the sample with the highest iron content. From their paper, a correlation between position and iron content seems to be reasonable, whereas it is not clear if the band position shifting is related to the An content, as suggested. For this reason, in this thesis, even if we are dealing with a PL (PL1) characterized by a different An content, we plot our results versus the iron content, neglecting the Na/Ca ratio, because the PL Crystal Field absorption bands are due to iron transitions in mineral crystal lattice (Burns, 1993).
The Fe, Mg (mafic) compositions consist of five distinct mineral assemblages1) E1, 44% CPX and 56% OPX mixture; 2) E2, 70% OPX and 30% OL; 3) 28.2% OPX, 3.4% CPX and 68.4% OL;4) E4, 100% OL; and 5) E5, 100% OPX. Tab. 7.2 shows the end-member's chemistry as well as the FeO wt.% content in each mineral.

End-members	Minerals % and Chemistry	FeO wt.% in minerals
E1	CPX(43.9%) En_{45}-Wo_{46}	5.72
	OPX(56.1%) En_{77}	13.45
E2	OPX(70%) En_{86}	7.44
	OL(30%) Fo_{87}	11.70
E3	OPX(28.2%) En_{82}	9.03
	CPX(3.4%) En_{45}-Wo_{46}	3.80
	OL(68.4) Fo_{84}	14.65
E4	OL(100%) Fo_{90}	9.73
E5	OPX(100%) En_{82}	10.67
PL1	An_{45}	0.1
PL2	An_{80}	0.36
PL3	An_{80}	0.5

Tab. 7.2 Table shows the end-member's chemistry and the relative FeO wt.% content in each mineral.

Using each end-member, a total of 130 mixtures have been prepared at two different particle sizes, 63-125 µm and 125-250 µm, with PL ranging between 20 and 90 wt.%. The 63-125 µm mixtures have been micronized to produce the <10µm mixtures using a micronizer at the Department of Geosciences, Padova University.

For each of the resulting mixtures, we calculated the new total FeO vol.% content for the PL and Fe, Mg mineral chemistries and the vol. FeO% due to PL phase with respect to the mixture (Serventi et al., 2013; 2015). The volumetric FeO% has been calculated as the FeO wt.% content in PL multiplied by modal PL (%) in each mixture. With the term volumetric iron because it defines the iron abundance for the mineral phase in the volume of our mixture, similarly to Pompilio et al. (2007), Carli and Sgavetti (2011).
The same end-members were used to produce a total of 63 mixtures with PL ranging between 90-99%, and consequently the mafic content from 10 to 1 wt.%. For these mixtures, we do not calculate the vol. FeO%: the spectral parameter variation has been evaluated vs. the PL content.

7.3 Analytical methods

7.3.1 Spectroscopic measurements

Bidirectional reflectance spectra of each mixture were acquired at room temperature and normal atmospheric pressure with a Field-Pro Spectrometer mounted on a goniometer (Istituto di Astrofisica e Planetologie Spaziali, Inaf-IAPS, Roma). The spectra were acquired with a spectral resolution of ~3 nm in the VIS and of ~10-12nm in the NIR, with $i=30°$ and $e=0°$. The source used was a QTH (Quartz Tungsten Halogen) lamp and the spot illuminated has an area of ca. 0.5cm^2. The calibration of the spectrometer was performed with Spectralon® optical standard (registered trademark of Labsphere, Inc.).
Regarding the very fine particle sizes, several spectra have been acquired from each powder, and then only the mean spectrum has been considered. In order to avoid problems due to "slab behavior" or to the powder roughness, powders have been slightly pressed in the sample holder.

7.3.2 Qualitative analyses

The influence of PL on reflectance spectra of Fe, Mg minerals is firstly described in terms of spectral shape, continuum, band depth and band width variations and band position shifting. The spectral parameter variations were determined in continuum removed spectra, using the software ORIGIN® and considering the continuum line, function of wavelength, as the straight-line segments that join the reflectance maxima in the spectrum (Clark and Roush, 1984; please refer to Fig. 2.8b). Continuum line depends on the reflectance maximum positions in the spectrum, so it will vary between different spectra. For each absorption band of the continuum-removed spectrum we evaluated the position of the band absolute minimum as the wavelength corresponding to the reflectance minimum, the depth as the distance between the minimum and the continuum line and the band width, or FWHM, as the difference between the λ values at half depth.
The spectral parameters describing the absorption bands were labeled as follows: 1) "Band PX" indicates the ~900 nm PX absorption in E1, in E2 and in E5- bearing mixtures, 2) "Band PL" indicates the ~1200 nm PL absorption in the E1 and E5-bearing mixtures, 3) "Band COMP" represents the OL-PL composite absorption in the 1200 nm interval in the E2, E3 and E4-bearing mixtures, where the two absorptions cannot be clearly distinguished. PX 1800 nm band has not been considered here, because we focused on the spectral region affected by PL absorption band.
Two additional parameters, the maximum (H1) in the about 500-700 nm region and the band shoulder (H2) in the about 1500-1700 nm spectral region, were taken into account. H1 and H2 variations were evaluated in terms of position and Δ-reflectance (the difference between the continuum reflectance and H reflectance) variations. These parameters can be useful to qualitatively describe the variation of the abundance of PL.

7.3.3 Quantitative analyses: the MGM algorithm

As explained in section 2.4, the MGM is a statistic-base method based on the assumption that different mineral absorptions can be described with a modified Gaussian distribution superimposed on to a continuum. MGM is widely applied on mineral phases and mixture analysis, in particular for the electronic absorptions (e.g., Sunshine et al., 1990; Sunshine and Pieters, 1993, 1998; Klima et al., 2007, 2011; Clénet et al., 2011). Different papers used also Gaussian models to determine the vibrational overtones present in hydrated silicates, carbonates and sulfates measured in laboratories (see
Sgavetti et al., 2015; and references therein).
The MGM algorithm models the continuum as a function of the wavenumber, with two parameters(Sunshine et al., 1990, please refer to Fig. 2.8a), the intercept c0 (variable between negative values and 0 with increasing reflectance values) and the offset c1 (variable from negative values/red slope to positive values/blue slope), while each Gaussian is described by three parameters, the band depth (in logarithm of the reflectance), the band center and the band width (both in nanometers).

7.3.3.1 Continuum

The continuum is still today not fully understood, and different approaches are used in the literature. Moreover, in the literature there is not a specific procedure to follow when applying the Gaussian modeling to a reflectance spectrum. So the continuum choice has been the result of the following considerations (serventi et al., 2015).
Fig. 7.1a shows the reflectance spectra for the E5+PL3 mixtures at the 63-125 μm size; these mixtures have been selected as an example because are composed with a mono-mineralic mafic end-member (100% OPX) and an iron-rich PL and because the OPX and PL absorption bands are well separated. Fig. 7.1a shows that increasing the PL modal abundance the spectra have higher albedo and their shape changes from a red slope (spectrum in the VIS have lower reflectance values than spectrum in the NIR) to an almost blue slope (spectrum in the VIS have higher reflectance values than spectrum in the NIR). Therefore, we expect that, increasing the PL content, both the offset c0 and the slope c1 increase towards positive values.

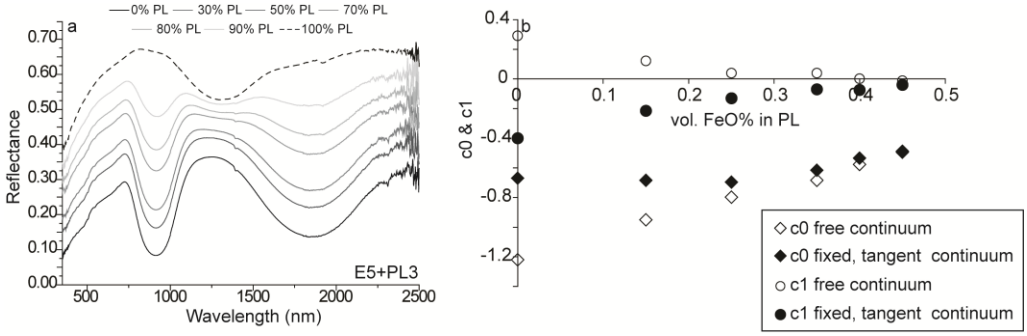

Fig. 7.1The figure shows the reflectance spectra for the E5+PL3 mixtures (from Serventi et al., 2015). a) increasing the PL modal abundance the spectra have higher albedo and their shape changes from a red slope to an almost blue slope ; b) the c0 and c1 behavior with different continua after MGM deconvolution: leaving both c0 and c1 free to vary, c0 become more positive while c1 moves towards negative values (empty symobls); while considering a fixed continuum tangent to the spectrum reflectance maxima, c0 still become more positive and c1 also moves towards positive values (filled symbols).

In Fig. 7.1b is shown the c0 and c1 behavior with different, linear continua choosen for the MGM deconvolution and with increasing the PL modal abundance, and, as a consequence, the vol. FeO % in PL:

1) Considering a free continuum (so leaving both c0 and c1 free to vary), c0 become more positive while c1 moves towards negative values (empty symbols in Fig.7.1b); while
2) Considering a continuum with fixed c0 and c1 for all the mixtures, and tangent to the spectrum reflectance maxima, c0 still become more positive but c1, differently from point (1), moves towards positive values (filled symbols in Fig.7.1b), as expected.

From the comparison of the different behavoirs of c1 with the spectrum shape of the mixtures, we considered a fixed and tangent continuum as more reliable.
Furthermore, considering the PL modal abundance, we needed a continuum that model the real strength of the absorption bands (see also Clenet et al., 2011) thus avoiding an horizontal continuum but choosing a tangent continuum.

7.3.3.2 Gaussians

We first deconvolved the end-members, mafic and PL, as mineralogically unknown end-members, assigning Gaussians only where either an absorption band or a band asymmetry are visually perceptible. The rational of this was that the objective of planetary surface spectroscopy is the interpretation of the unknown mineralogical composition of that surface.
Then, we deconvolved the mixtures, considering that our goal is to analyze PL behavior when mixed with mafic minerals, and that:

1) If measured under the same conditions, the band center and width of mafic minerals depend only on the chemistry (e.g. the iron content, Burns, 1993);
2) the band depth is related with the abundance of the mineral phase in a mixture (in particular for mafic phases, see Sunshine and Pieters, 1993; 1998);
3) no data in the literature discussed in a systematic way the PL behavior varying iron content;
4) in mixtures composed with OL and PL we cannot assume that the composite band center and width will remain fixed varying the OL and PL modal abundance.

So, we decided that the band center and the band width assigned to the mafic absorption bands must be fixed for the Gaussians because these parameters are only relate to the mineral chemistry, whereas the mafic band depth, that varies with the modal abundance, as well as Gaussians assigned either to PL or to COMP (PL+OL) absorption bands, were left free. This also helped to avoid a high number of free parameters. Consequently, only the spectral parameters variations of the ~1250 nm (PL and COMP) band and the mafic mineral band depth will be discussed.
In this thesis, the ~900 nm and the ~1800 nm PX absorption bands are defined as Band I and Band II, respectively; the OL absorptions are defined Band 1,2 and 3; the complex absorption of PL and OL in the 1200 nm region is called COMP Band; and the 1250nm absorption band is called PL band. A number has been assigned to each Gaussian, as shown in Tab. 7.3.

Gaussian	Position (nm)	Interpretation
G1	900-950	Fe^{2+} in OPX M2 site
G2	1000-1100	Fe^{2+} in CPX M2 site
G3	1850	Fe^{2+} in OPX M2 site
G4	2300	Fe^{2+} in CPX M2 site
G5	840	Adjustment Gaussian
G6	850-950	Fe^{2+} in OL M1 site
G7	1000-1100	Fe^{2+} in OL M2 site
G8	1200-1250	Fe^{2+} in OL M1 site
G9	650	IVCT
G10	1250-1300	Fe^{2+} in PL
G11	1600-1800	PL asymmetry

Tab. 7.3 In the table are reported a list of Gaussians used in the end-member deconvolution, the wavelength position and the mineralogical interpretation.

8. Spectral reflectance of plagioclase bearing mixtures: 63-125 µm and 125-250 µm mixtures

8.1 Spectral characteristics of the end-members: qualitative analyses

8.1.1 Fe, Mg end-members

8.1.1.1 E1

The reflectance spectrum of E1 for the 63-125 µm particle size (solid lines in Fig. 8.1a,b) shows two main absorption bands at 955 nm and 1905 nm assigned to Fe^{2+} in distorted octahedral M2 site in OPX and type B CPX (Cloutis and Gaffey, 1991; Burns, 1993). In this spectrum it is not possible to discriminate between the OPX and CPX absorption bands, combined in a composite band centered at 955 nm and located between OPX (~900 nm) and CPX (~1000 nm) absorption positions. Minor absorption bands are also present at 650 nm, assigned to a Fe^{3+}-Fe^{2+} IVCT transition. Other absorptions occur at 1400 nm, 1900 nm and 2310 nm due to mineral alterations (e.g., by H_2O and Mg-OH^- vibrational modes). In the spectra of the coarsest particle size powders (dashed lines), the PX absorption bands are still present but the band minima are shifted at longer wavelength (976 nm and 1909 nm respectively), the absorption band depths are less prominent and the albedo is lower with respect to the fine particle size.

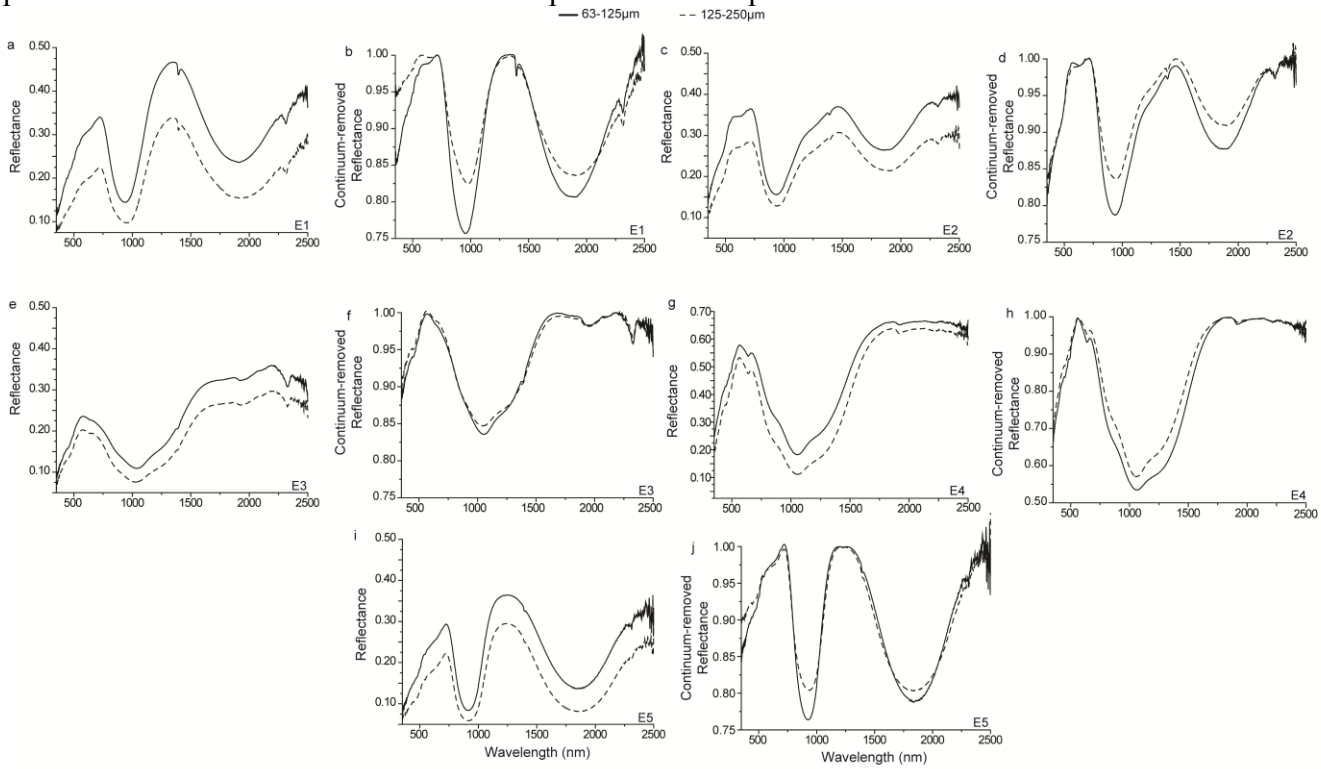

Fig. 8.1The figure shows the reflectance spectra for each mafic end-member at different particle sizes. 63-125 µm: solid lines; 125-250 µm: dashed lines. Considering the 63-125 µm size: a,b) E1 shows two principal absorptions at ~955nm and ~1905nm due to Fe^{2+} in M2 site of OPX and CPX; c,d) E2 shows two principal absorptions at ~938nm and ~1891nm due to Fe^{2+} in M2 site of OPX and a flattening in the 1200nm region associated with Fe^{2+} in M1 site of OL; e,f) E3 is characterized by a composite band centered at 1056nm attributable to Fe^{2+} in M1 and M2 site of OL; g,h) E4 displays a broad band centered at 1064 nm, due to Fe^{2+} transition in OL M1 and M2 sites; and i,l) E5 shows two absorption bands at 929 and 1850nm, due to the Fe^{2+} transition in OPX M2 site. Coarsening the particle size, all the end-members show lower albedo and less intense absorption band, while E3, despite a lower albedo, does not show any difference about band depth.

8.1.1.2 E2

In Fig.8.1c,d, the E2 reflectance spectrum for the 63-125µm particle sizes shows two principal absorption bands at 938 nm and 1891nm, due to Fe^{2+} in distorted octahedral M2 site in OPX (Burns, 1993), whereas the spectral flattening in the 1200 nm region is interpreted as the Fe^{2+}transition in OL M2 site (Burns, 1993). The first two absorption bands of OL, due to Fe^{2+} in OL M1 and M2 sites (Burns, 1993) cannot be clearly resolved, although the visually perceptible 938 nm band asymmetry toward the NIR region suggests the combination of the OPX and OL absorption bands. An additional IVCT absorption band occurs at 630 nm, probably due to a Fe^{3+}-Fe^{2+} IVCT transition, and vibrational bands are present at 1400 nm and 2310 nm, due to mineral alterations (e.g., H_2O and Mg-OH^-). In the spectrum of the coarse particle size (dashed lines), the minima of both bands are at slightly longer wavelengths (945 nm and 1906 nm) and the band depth is less intense than in fine particle powder spectra. In addition, the albedo is lower than in the fine-grained sample spectra.

8.1.1.3 E3

The reflectance spectrum of E3 for the 63-125µm particle sizes (Fig. 8.1e,f) shows a broad composite absorption band centered at 1056 nm, attributable to Fe^{2+} in M1 and M2 sites of OL (Burns, 1993). Other negligible absorption bands at 630 nm, probably due to a Fe^{3+}-Fe^{2+} IVCT transition, and weak vibrational bands at 1400 nm, 1900 nm and 2310 nm are also observed. In the coarse particle size (dashed lines) the OL absorption bands are less intense and occur at shorter wavelength than in fine-grained spectrum (solid lines). The composite band minimum in this spectrum is at 1042 nm.

8.1.1.4 E4

As in the E3 end-member, the reflectance spectrum of E4 for the 63-125µm particle sizes (Fig. 8.1g,h) is characterized by a broad composite absorption band centered at 1064 nm, attributable to Fe^{2+} in M1 and M2 sites of OL (Burns, 1993). An absorption band at 637 nm, probably due to a Fe^{3+}-Fe^{2+} IVCT transition, and a weak vibrational band at 1900 nm are detected. In the coarse particle size (dashed lines) the OL absorption band is less intense and occurs at 1056 nm.

8.1.1.5 E5

The reflectance spectrum of E5 for the 63-125 µm particle size (solid lines in Fig. 8.1i,j) is characterized by two main absorptions at 929 nm and 1850 nm assigned to Fe^{2+}transition in distorted octahedral M2 site in OPX (Burns, 1993). Minor absorption bands are also present at 650 nm, assigned to a Fe^{3+}-Fe^{2+}IVCT transition, at 1400 nm and 2310 nm due to mineral alterations (e.g., by H_2O and Mg-OH^- vibrational modes). In the coarsest size spectrum (dashed lines), the albedo is lower and the OPX absorptions are shallower and shifted towards longer wavelength (934 nm and 1850 nm respectively) with respect to the fine particle size.

8.1.1.6 Comparison between mafic end-members

Comparing different particle sizes, a coarse size produces: (1) a shifting of the PX absorption bands toward longer wavelengths and of the OL absorption towards shorter wavelengths (refer to the fourth column in Tab. 8.1); (2) less intense absorption bands, with a band depth variation maximum for E1 and minimum for E3 end-members (refer to the third column in Tab. 8.1); and (3) a systematically lower albedo.

The narrow shift of the absorption minima can be explained in different ways: 1) the FieldSpec spectral resolution varying between 2-12 nm and the difference in the two particle sizes thus falling in the instrumental error; 2) a different particle distribution in the particle sizes of mixture

end-members; and 3) a different particle size affecting the continuum in unpredictable ways with consequences not completely correctable even on the spectral parameters.
Considering OL-PX bearing end-members, in the E3 end-member (Fig. 8.1e,f), the OPX absorption band due to 30% OPX is not resolvable (even if E3 has been analyzed in detail, thus assuming the mineralogical composition reliable), while in the spectra of the E2 end-member (Fig. 8.1c,d), 30% OL is clearly expressed in the 1200 nm flattening. Indeed, the corresponding volumetric FeO contents in the two phases are similar in the E2 end-member (3.03% in OL and 5.29% in OPX), but are very different in the E3 end-member (10.02% in OL and 2.54% in OPX), resulting in the clear OL predominance in the E3 spectrum.

End-member	Particle size (μm)	Band depth (refl)	Band position (nm)	Band width (Δnm)
E1	63-125	0.244	955	298
	125-250	0.174	976	304
E2	63-125	0.212	938	314
	125-250	0.162	945	308
E3	63-125	0.163	1056	599
	125-250	0.155	1042	630
E4	63-125	0.462	1064	677
	125-250	0.428	1056	588
E5	63-125	0.236	929	245
	125-250	0.195	934	250
PL1	63-125	0.06	1264	418
	125-250	0.077	1275	441
PL2	63-125	0.149	1278	491
	125-250	0.199	1279	487
PL3	63-125	0.146	1298	495
	125-250	0.179	1301	518

Tab. 8.1 End-member spectral parameters extracted from ORIGIN analysis.

8.1.2 PL end-members

In Fig.8.2a,b, the PL spectra show a main absorption band in the 1250 nm region, due to Fe^{2+} replacing Ca^{2+} in seven coordination site (Bell and Mao, 1973; Burns, 1993). The spectra also show weak vibrational bands at 1400 nm, 1900 nm, 2200 nm and 2310 nm due to alterations (e.g., H_2O, Al-OH^- and Mg-OH^-) in the natural PL used here. The 1250 nm absorption band observed in relatively iron-rich PL becomes asymmetric toward the 1800-2000 nm spectral region, and it is associated with a possible but undefined band in the ca. 1800 nm region. However, we do not observe an absorption band at 2000 nm, detected by other authors in synthetic PL (Burns, 1993; Cheek et al., 2011) and tentatively assigned to Fe^{2+} in multiple coordination environment (Appleman et al., 1971; Hafner et al., 1971; Dyar et al., 2002). Fig.8.2c displays the variation of the PL continuum from red to blue slope with increasing FeO wt.% in PL for both fine (solid lines) and coarse (dashed lines) particle size.
In Fig.8.2d-f, the spectral parameters are plotted vs. the wt.% FeO content in PL. In the spectra of 63-125 μm particle size PL (full symbols), PL band depth (Fig. 8.2d) increases from PL1 to PL2 end-members, whereas it remains almost unchanged for PL2 and PL3 end-members. Similarly,

the band minima are clearly shifted towards longer wavelengths with increasing iron content in PL (from 1264 nm and 1279 nm to 1298 nm, Fig. 8.2e). Fig.8.2f also shows that band widens with FeO wt.% content in PL, apparently associated with increasing asymmetry toward the IR region, visible in the spectra.
Similar behaviors are also observed for the coarse particle size (empty symbols), with the band becoming deeper (Fig. 8.2d), shifted towards longer wavelengths (1275 nm, 1278 nm, and 1301 nm; Fig. 8.2e), and wider than fine particle size (Fig. 8.2f).
Both increasing iron content and particle size produce deeper bands, a minimum shift toward the IR region and an overall decrease of the reflectance.

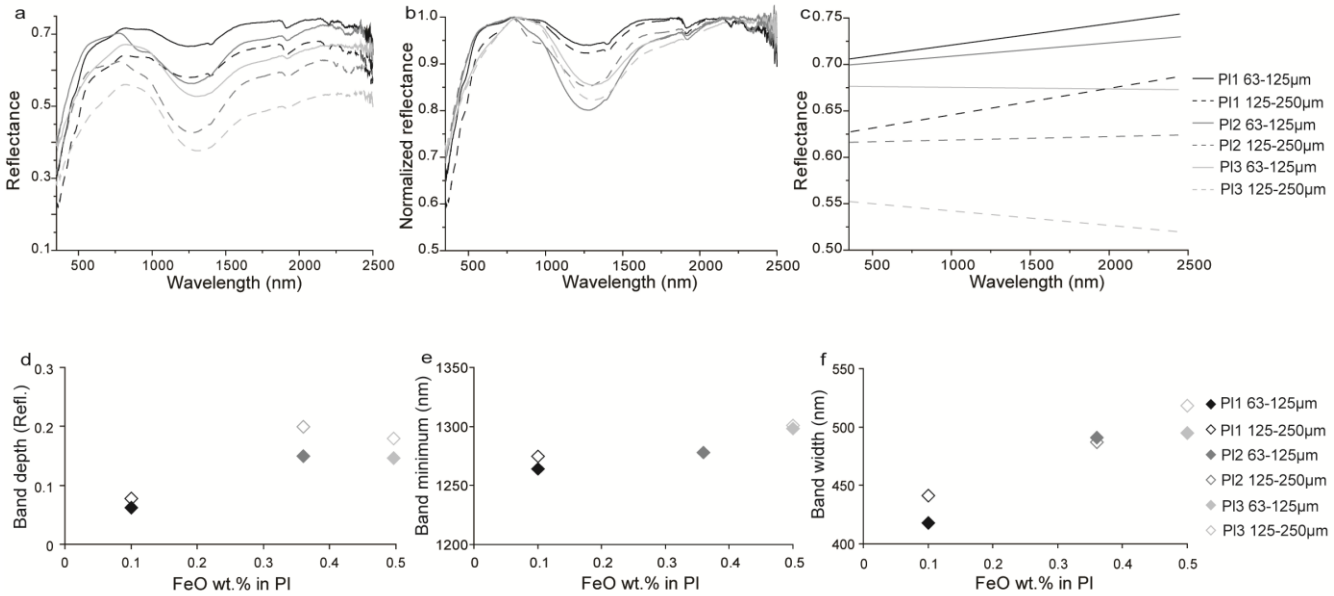

Fig. 8.2 a) Reflectance spectra of PL with different chemistry and different particle size (from Serventi et al., 2013). PL shows a principal absorption band in the 1250 nm region that becomes asymmetric toward the IR with increasing FeO wt.% in PL; b) Continuum-removed spectra; c) PL continua vary from a red to a blue slope adding FeO wt.% in plagioclase; d) PL band depth increases from PL1 to PL2 but it slightly decrease from PL2 to PL3; coarse PL (empty diamonds) are deeper than fine ones (full diamonds); e) PL minimum shifts to IR region from PL1 to PL3; f) PL band widens from PL1 to PL3; coarsening the particle size (empty diamonds), except PL2, band is wider than fine particle size (full diamonds).

8.2 Spectral characteristics of the mixtures: qualitative analyses

Fig. 8.3 and 8.4 show the reflectance spectra of the mixtures at the two different particle sizes.
For each of the mixture compositions, three interdependent variables are expected to exert a non-linear control on the overall spectral shape and absorption band parameters: 1) the decreasing content of the Fe, Mg component related to increasing PL modal abundance; 2) the increasing FeO wt. % concentration in PL, that consequently no more can be considered a transparent mineral phase, and 3) the particle size effects, as this parameter controls the optical path of the light. The first two variables combine to determine the total FeO in the mixtures (i.e., overall decreasing with increasing PL percentage), while the last variable introduces the effects of the optical path and the mineral contiguity, critical in coarse Fe, Mg end-members.

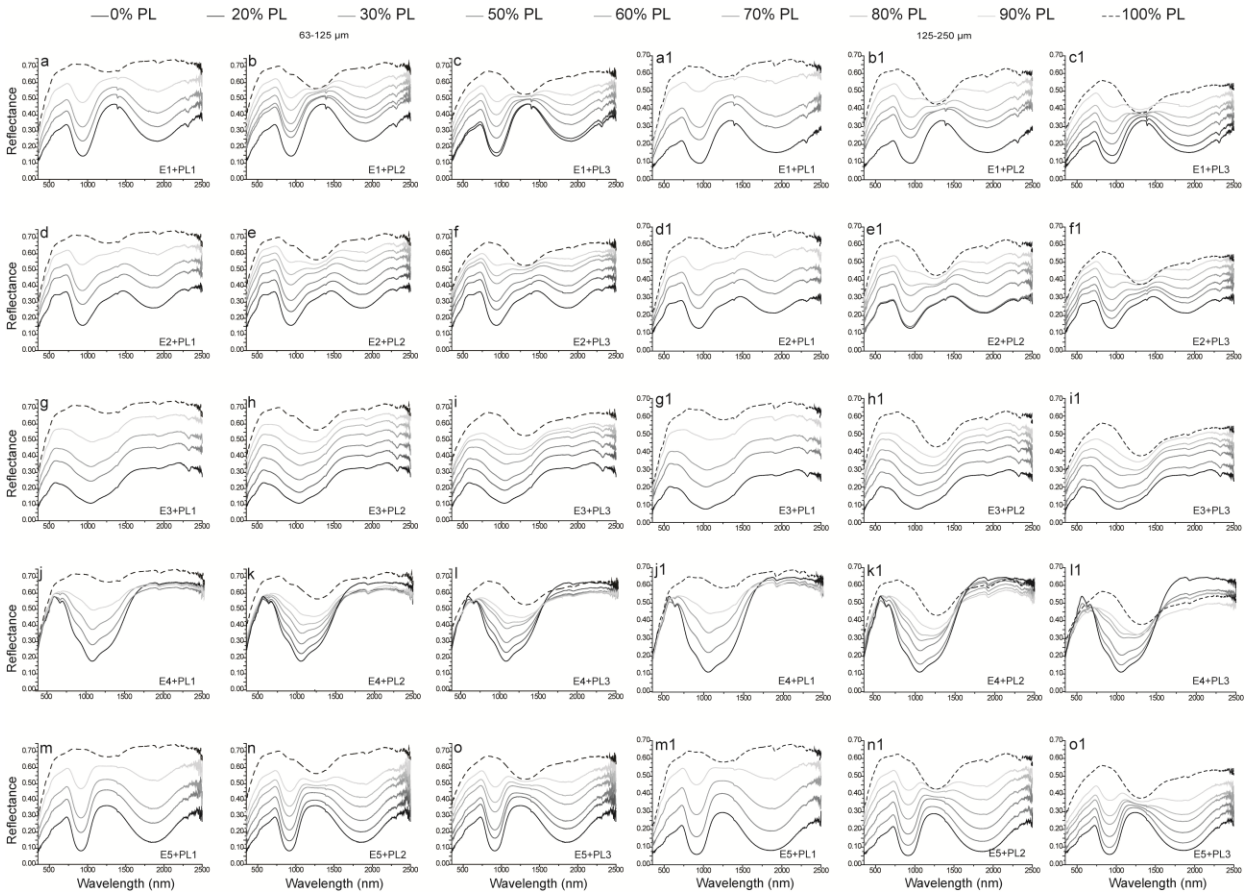

Fig. 8.3 Reflectance spectra at the 63-125 µm particle size. a)E1+PL1 (from bottom to top PL1:0-50-70-90-100); b) E1+PL2 (from bottom to top PL2:0-50-60-70-80-90-100); c)E1+PL3 (from bottom to top PL3:0-20-50-70-80-90-100); d)E2+PL1 (from bottom to top PL1:0-50-70-90-100); e)E2+PL2 (from bottom to top PL2 :0-30-50-70-90-100); f)E2+PL3 (from bottom to top PL3 :0-30-50-70-90-100); g)E3+PL1 (from bottom to top PL1 :0-50-70-90-100); h)E3+PL2 (from bottom to top PL2 :0-30-50-70-90-100); i)E3+PL3 (from bottom to top PL3 :0-30-50-70-90-100); j)E4+PL1 (from bottom to top PL1 :0-50-70-90-100); k)E4+PL2 (from bottom to top PL2 :0-30-50-70-90-100); l)E4+PL3 (from bottom to top PL3 :0-30-50-70-90-100); m)E5+PL1 (from bottom to top PL1 :0-50-70-90-100); n)E5+PL2 (from bottom to top PL2 :0-30-50-70-90-100); o)E5+PL3 (from bottom to top PL3 :0-30-50-70-90-100). Plagioclase modal abundance increases from the bottom (black spectrum) to the top (dashed line spectrum). Mixtures with PL1 are less than mixtures with PL2 and PL3 because PL1 is characterized by a weak 1250 nm absorption that is resolvable only for high PL content. a1-o1: 125-250 µm

8.2.1 E1+PL1 mixtures

Fig. 8.3a-c shows the E1+PL mixtures: PL1 produces a flattening in the 1250 nm region only from 90%, while the flattening is visible from 30% PL2 and PL3. If PL2 and PL3 are up to 80% a well-defined band can be resolved, and the band is deeper in PL3-mixtures than in PL2.mixtures.
Fig.8.3a1-c1 report the effects of coarse particle size on the mixture spectra. PL produces a well resolved absorption band for lower PL concentration than for fine mixtures. It is also evident that for more than 90% PL2 and PL3 content, the PL absorption band is more intense than the PX absorption band.
Thus, we can summarize that, in general, adding PL to the Fe, Mg end-member produces higher albedo, a continuum's flattening in the 1300-1500 nm spectral region and a reduced spectral contrast and that PL produces first a flattening in the 1250 nm region and only for high PL content an absorption band can be resolved. However, a variety of behaviors are observed when PL with different FeO wt.% contents are included in the mixtures, as documented by the spectral parameter variations plotted in fig. 8.4. Since PL minimum is not clearly detectable, the PL

absorption band depth has been calculated keeping fixed its minimum position at 1264 nm, 1279 nm and 1298 nm for PL1, PL2 and PL3, respectively, in the fine particle size, and at 1275 nm, 1278 nm and 1301 nm for the coarse particle size.

In particular, Fig.8.4 shows that, increasing the vol. FeO% due to the PL fraction:

1) the PX band depth decreases and PL band depth increases (Fig. 8.4a) becoming very similar for about 0.324% vol. FeO in PL2-bearing mixtures (90% PL2) and for 0.45% vol. FeO in PL3-bearing mixtures (90 % PL3);
2) the PX absorption minimum shifts to shorter wavelengths until ca. 70-80%, but to longer wavelengths for volumetric FeO >0.25 in PL2 and for volumetric FeO>0.3% in PL3 (Fig. 8.4b);
3) the PX band width becomes narrower (Fig. 8.4c) until 70-80% (0.252-0.288vol. FeO% and 0.35-0.4 vol. FeO%) of PL amount. For higher PL content it is not possible to calculate the width.

Fig. 8.4 also show the particle size effects (empty symbols): a coarse particle size produces less intense PX absorption bands but deeper PL absorption (Fig. 8.4a), band minimum displacements toward longer wavelength (Fig. 8.4b) and broader band with respect to the fine particle size (Fig. 8.4c).

Increasing PL modal abundance, H1 and H2 positions move to longer wavelength and H2 Δ-reflectance increases (Fig. 8.4d-f).

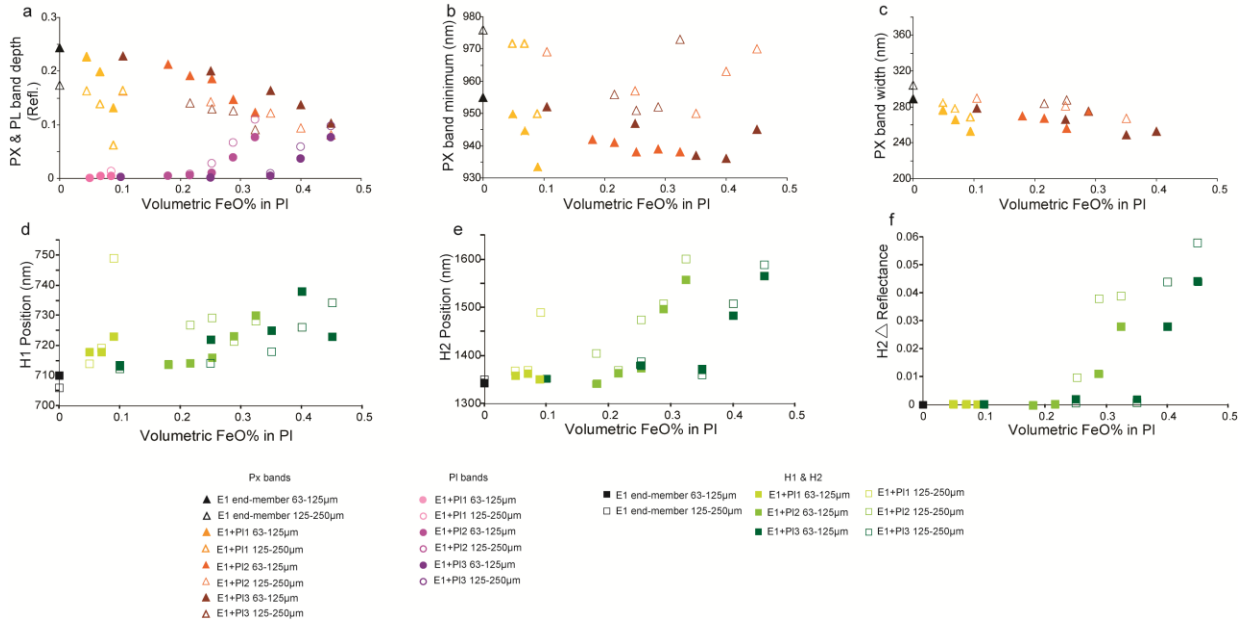

Fig. 8.4 Spectral parameters variation vs. the volumetric FeO% due to PL phase in each mixture (from Serventi et al., 2013). Increasing volumetric FeO% due to PL, a) PX band depth (triangles) decreases while PL depth (circles) increases. Coarsening the particle size produces less intense PX bands but deeper PL bands; b)PX band minimum shifts to Ultraviolet (UV) region but for high PL content shifts to IR region. At coarse particle size, the minimum is shifted to longer wavelength ; c) PX band width becomes narrower and a coarse particle size produces broader bands; d) H1 (1500-1700 nm region) position moves to longer wavelength; e) H2 position moves to longer wavelength and a coarse particle size produces a shifting towards the IR region; f) H2 Δ-reflectance increases.

8.2.2 E2+PL mixtures

In this Fe, Mg end-member, the small OL content is responsible for the spectral flattening in the 1250 nm region due to the OL band 3 (Figs. 8.3d-f, d1-f1).

Also in this case, adding PL produces progressively higher albedo and reduced spectral contrast. Figs.8.3d-f show that: PL1 does not produce a clear absorption band, masked by OL even for 90% PL content, PL2 content produces an inflection in the 1200 nm region that can be resolved as absorption band for PL2>50% while the PL absorption band is better defined starting from 30% PL3.

In Figs. 8.3d1-f1, the coarse particle size emphasizes the presence of PL in the 1200 nm interval: the PL absorption band can be detected for 90% PL1, 30% PL2 and 30% PL3.

In general, adding FeO wt.% content in PL and coarsening the particle size produce a lower albedo.

Fig.8.5a-c reports, for all the mixtures, the diagrams of the variations of the Fe, Mg component and PL spectral parameters with increasing the volumetric FeO content in PL.

Specifically:

1) the OPX absorption band depth decreases and, except in the PL1-bearing mixtures (pink filled circles), the composite absorption band depth increases with increasing vol. FeO% (Fig. 8.5a). Furthermore, for volumetric FeO>0.4%, the composite band absorption is deeper than the OPX absorption band depth (Fig. 8.5a);
2) the OPX band minimum is almost unchanged, with a shift comprised within 10 nm, except for a few outliers (black stars in fig. 8.5b) representing mixtures with high content of PL at a coarse particle size (Fig. 8.5b);
3) the band width can be identified only for PL< 70 % and it does not show a clear trend (Fig. 8.5).

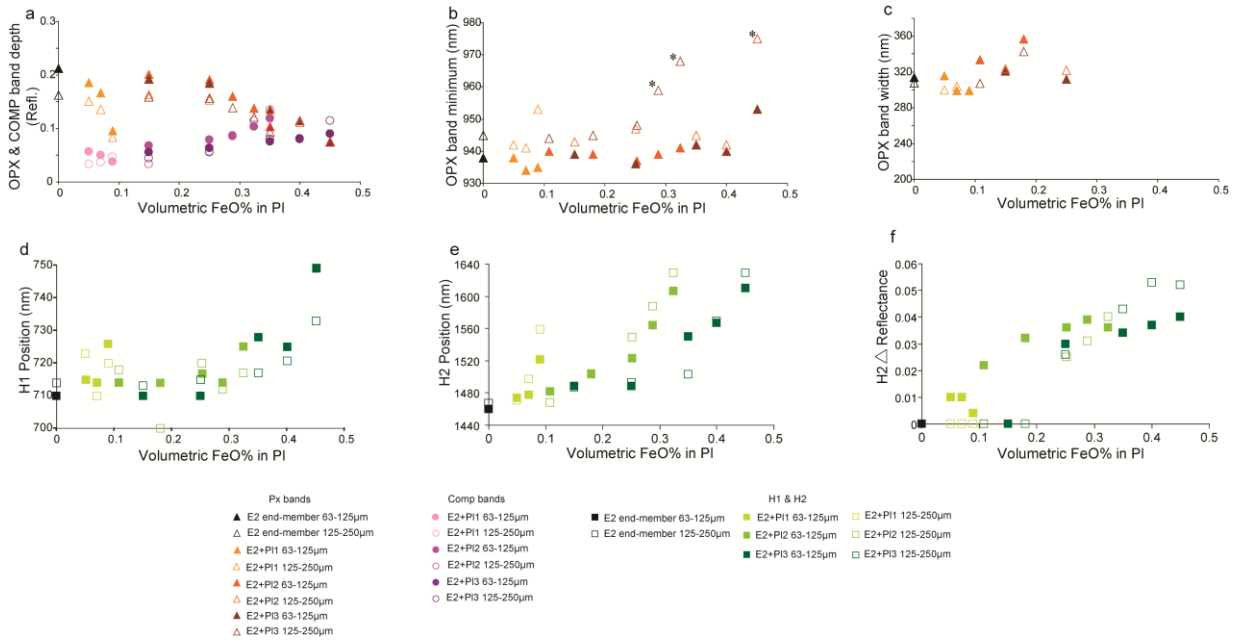

Fig. 8.5 Spectral parameters variation vs. the volumetric FeO% due to PL phase in each mixtures (from Serventi et al., 2013). Increasing volumetric FeO% due to PL, a) OPX band depth decreases while the composite band depth increases, except from PL1-bearing mixtures. Coarsening the particle size, PX depth is reduced while COMP depth is reduced for FeO %<0.3 but increased for higher content ; b) OPX band position does not show great variations, except from outliers identified with black stars. The position shift toward the IR region coarsening the particle size of higher FeO samples; c) OPX width does not show a clear trend at both particle sizes; d) H1 (1500-1700 nm region) position moves to longer wavelength; e) H2 position moves to longer wavelength and a coarse particle size produces a shifting the IR region; f) H2 Δ-reflectance increases.

A coarse particle size produces less intense OPX absorption band and, for vol. FeO% in PL <0.3, less intense composite band, while for higher vol. FeO% content composite band deepens (fig. 8.5a), OPX minimum shifts toward longer wavelength (fig. 8.5b) and OPX becomes wider (fig. 8.5c).
The presence of PL is also revealed by the H1and H2 positions shifting to longer wavelengths (Fig. 8.5d,e), and the Δ-reflectance increasing of the H2(Fig. 8.5f).

8.2.3 E3+PL mixtures

The starting OL content in this end-member is higher than in the previous end-member.
In these mixtures (Fig. 8.3g-i, g1-i1) the PL absorption is clearly superimposed on the three OL bands, so that it cannot be discriminated from the OL band 3. Consequently, we consider the OL band 3 and PL absorption as a unique composite band. The variation of PL concentration can however be detected from the absorption band position shifting toward longer wavelength.
In Fig. 8.3g-i the PL is not resolvable even for 90% PL1 content, while it can be resolved for more than 90% of PL2 and 80% of PL3. In contrast, in the coarsest particle size (Fig. 8.3g1-i1) the PL produces a deep absorption in the 1200 nm region and it can be resolved for > 90% PL1, > 80% PL2 and > 80% PL3. Moreover, in mixture with 90% PL3, PL causes a shift to longer wavelength of the composite band and totally masks the contribute of OL.
Fig. 8.6 shows that, with increasing the vol. FeO % due to the PL fraction:

1) the COMP band depth varies only slightly (Fig. 8.6a);
2) the COMP band minima form two distinct clusters: in the lower cluster, the OL spectral feature controls the composite absorption band, whereas, in the upper cluster, the PL absorption band is clearly predominant (Fig. 8.6b). In both cases, the band minimum shifts toward the IR region;
3) the COMP band becomes narrower (Fig. 8.6c).

Coarse particle size produce a COMP band depth attenuation for PL1 and low PL2 and PL3 content, increasing for vol. FeO% >0.25 (fig. 8.7a), a shifting of the position toward the IR region (fig. 8.6b) and narrower band width (fig. 8.6c).
The presence of PL is also revealed by a shifting of the H1 position for more than 0.35% vol. FeO, (Fig. 8.6d) and by the H2 Δ-reflectance increasing (Fig. 8.6f). H2 position variation does not show a clear trend (Fig. 8.6e).

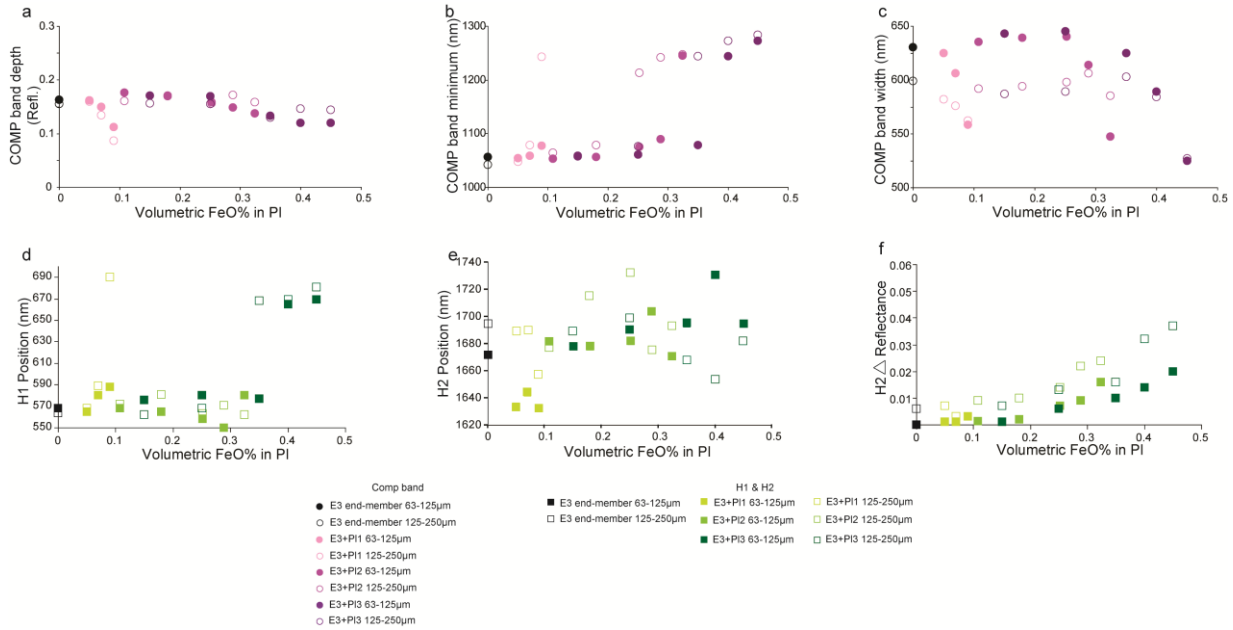

Fig. 8.6 Spectral parameters variation vs. the volumetric FeO% due to PL phase in each mixture (from Serventi et al., 2013). Increasing volumetric FeO% due to PL, a) COMP band depth slightly decreases. Coarsening the particle size, for FeO% <0.25 band depth is reduced while for upper content it increases; b) COMP band position form two cluster at different wavelength: in the lower cluster OL is dominant while in the upper cluster PL is dominant. A coarse particle size shifts the position toward longer wavelength; c) COMP band becomes narrow and a coarse particle size produces narrower bands; d) H1 (1500-1700 nm region) position moves to longer wavelength; e) H2 position does not show a clear trend; f) H2 Δ-reflectance increases.

8.2.4 E4+PL mixtures

These mixtures are composed with PL and 100% OL-bearing end-member. In this case, 1800 nm absorption bands are not expected, due to the OPX absence. Nevertheless, a reflectance decrease can be detected in the 1600-1800 spectral region (fig. 8.3j-l, j1-l1). In Fig. 8.3j-l the PL is not resolvable even for 90% PL1 content, while it can be resolved only for more than 90% of PL2, PL3. In the coarsest particle size (Fig. 8.3j1-l1) the PL band can be resolved for > 80% PL2 and >70% PL3. Moreover in mixture with 90% PL3, PL totally masks the contribute of OL.

Fig. 8.7 shows that, with increasing the FeO vol.% due to the PL fraction:

1) the COMP band becomes shallower (Fig. 8.7a);
2) the COMP band minima form two distinct clusters, as for the previous mixtures (Fig. 8.7b): in the lower cluster, the OL spectral feature controls the composite absorption band, whereas, in the upper cluster, the PL absorption band is clearly predominant (Fig. 8.8b);
3) the COMP band becomes narrower (Fig. 8.8c).

Coarse particle size produces a deeper COMP band (fig. 8.7a), a shifting of the position toward the IR region (fig. 8.7b) and wider band (fig. 8.7c).

As for the E3+PL mixtures, PL is also expressed by the H2 shifting towards longer wavelengths and Δ-reflectance increasing (Fig. 8.7e,f).

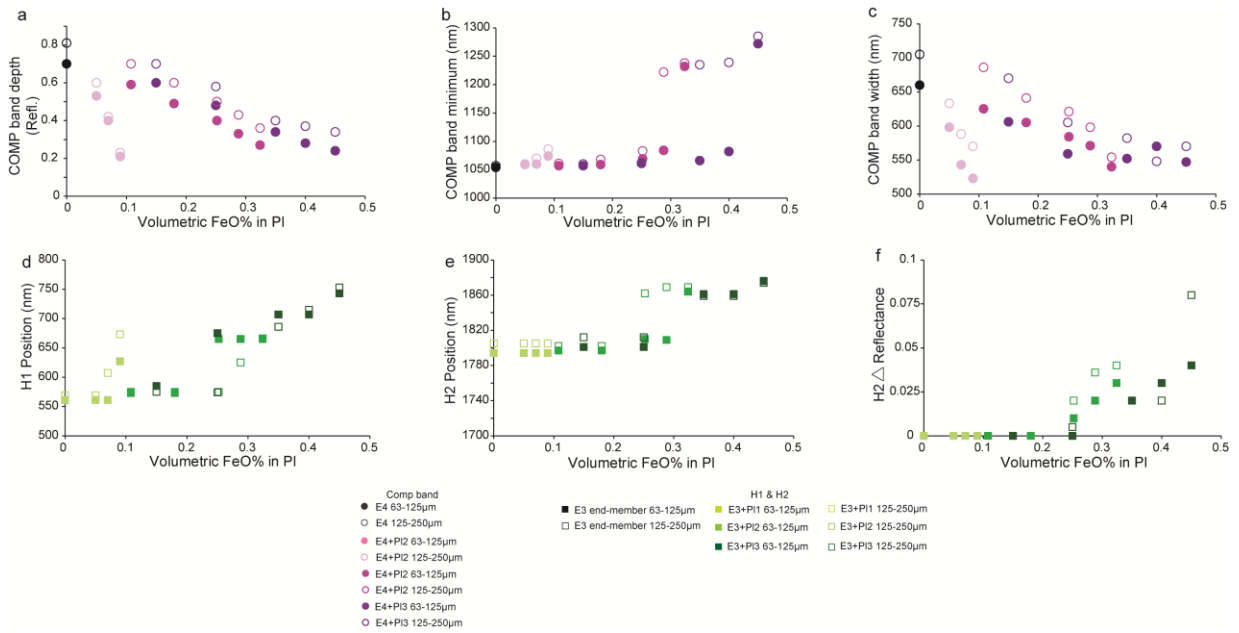

Fig. 8.7 Spectral parameters variation vs. the volumetric FeO% due to PL phase in each mixture. Increasing volumetric FeO% due to PL, a) COMP band depth decreases for the two particle sizes; b) COMP band position form two cluster at different wavelength: in the lower cluster OL is dominant while in the upper cluster PL is dominant. A coarse particle size shifts the position toward slightly longer wavelength; c) COMP band becomes narrow and a coarse particle size produces wider bands; d) H1 (1500-1700 nm region) position moves to longer wavelength; e) H2 position moves to longer wavelength; f) H2 Δ-reflectance increases.

8.2.5 E5+PL mixtures

Fig. 8.3m-o show that PL1 produces a flattening only from 90%, PL2 produces a flattening in the 1250 nm region from 50% PL whereas only for more than 80% PL a well-defined absorption band is produced, and the absorption band due to 80% PL3 is more intense than in previous mixtures.

Fig.8.3m1-o1 report the effects of coarse particle size on the mixture spectra. For these mixtures PL produces a well resolved absorption band for lower PL concentration than for fine-grained mixtures. It is also evident that for more than 90% PL3 content, the PL absorption band is more intense than the PX absorption band.

Differently from E1-bearing mixtures, the PL band is asymmetric towards the longest wavelengths.

Fig.8.8 shows that, increasing the FeO wt.% due to the PL fraction:

1) the OPX band depth decreases and PL band depth increases (Fig. 8.8a) becoming very similar for about 0.324% vol. FeO in PL2-bearing mixtures (90% PL2) and for 0.45% vol. FeO in PL3-bearing mixtures (90 % PL3);
2) the OPX absorption minimum shifts toward longer wavelengths for vol. FeO>0.4% in PL3-mixtures (Fig. 8.8b) and for vol. FeO > 0.36% in PL2-mixtures;
3) the OPX band becomes narrower (Fig. 8.8c) until 70-80% of PL amount. For higher PL content the band becomes wider.

A coarse particle size produces less intense OPX absorption bands but more intense PL absorption bands (Fig. 8.8a), a PX shifting towards slightly longer wavelengths and broader band width, even if for very high PL-content it is not possible to calculate the band width, with respect to the fine particle size (Fig. 8.8c).

Increasing PL modal abundance, H1 moves to longer wavelength, while H2 shifts towards shorter wavelengths and H2 Δ-reflectance increases (Fig. 8.8d-f). The opposite behavior of H2 position with respect to E1-bearing mixtures can be related to the absence of CPX.

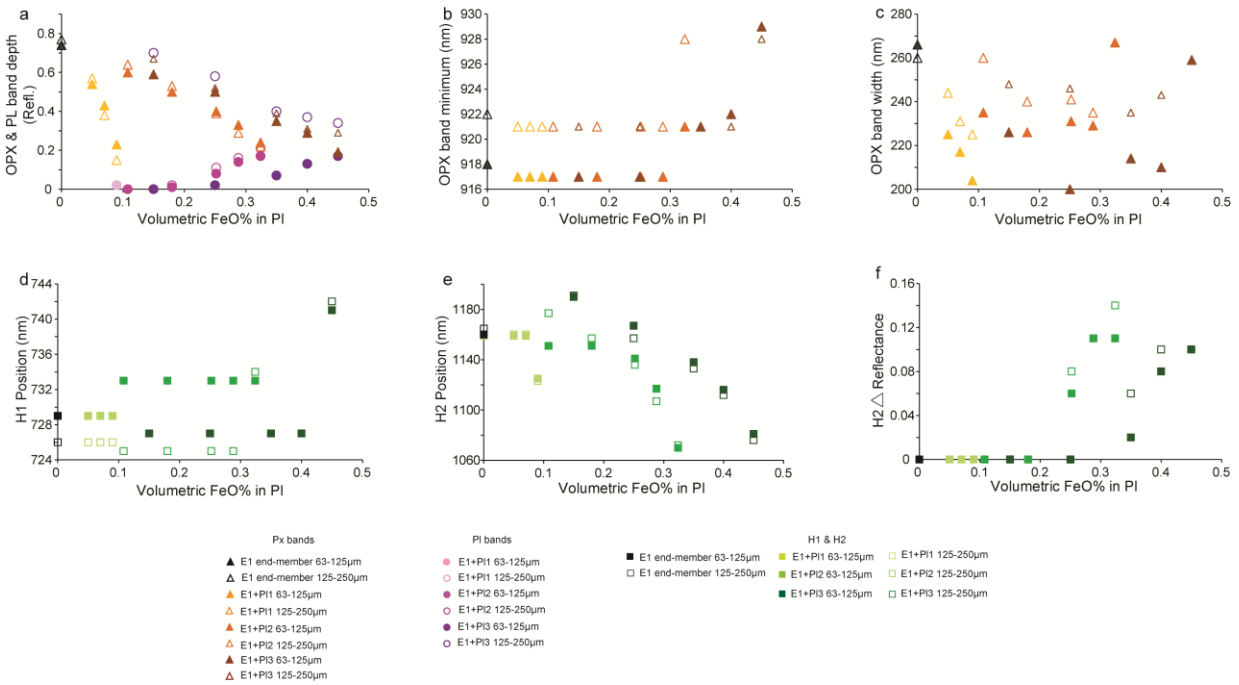

Fig. 8.8 Spectral parameters variation vs. the volumetric FeO% due to PL phase in each mixture. Increasing volumetric FeO% due to PL, a) OPX band depth (triangles) decreases while PL depth (circles) increases. Coarsening the particle size produces less intense OPX bands but deeper PL bands; b) OPX band minimum shifts toward the IR region. At coarse particle size, the minimum is shifted to longer wavelength; c) OPX band width becomes narrower until 70-80% PL and then the band becomes wider. A coarse particle size produces broader bands; d) H1 (1500-1700 nm region) position moves to longer wavelength; e) H2 position moves to shorter wavelength; f) H2 Δ-reflectance increases.

8.3 End-member deconvolution

8.3.1 Mafic end-members

Fig. 8.9 shows the end-members (left end column), their MGM deconvolution at 63-125µm and 125-250µm particle sizes (central and right end columns, respectively) and the residuals.

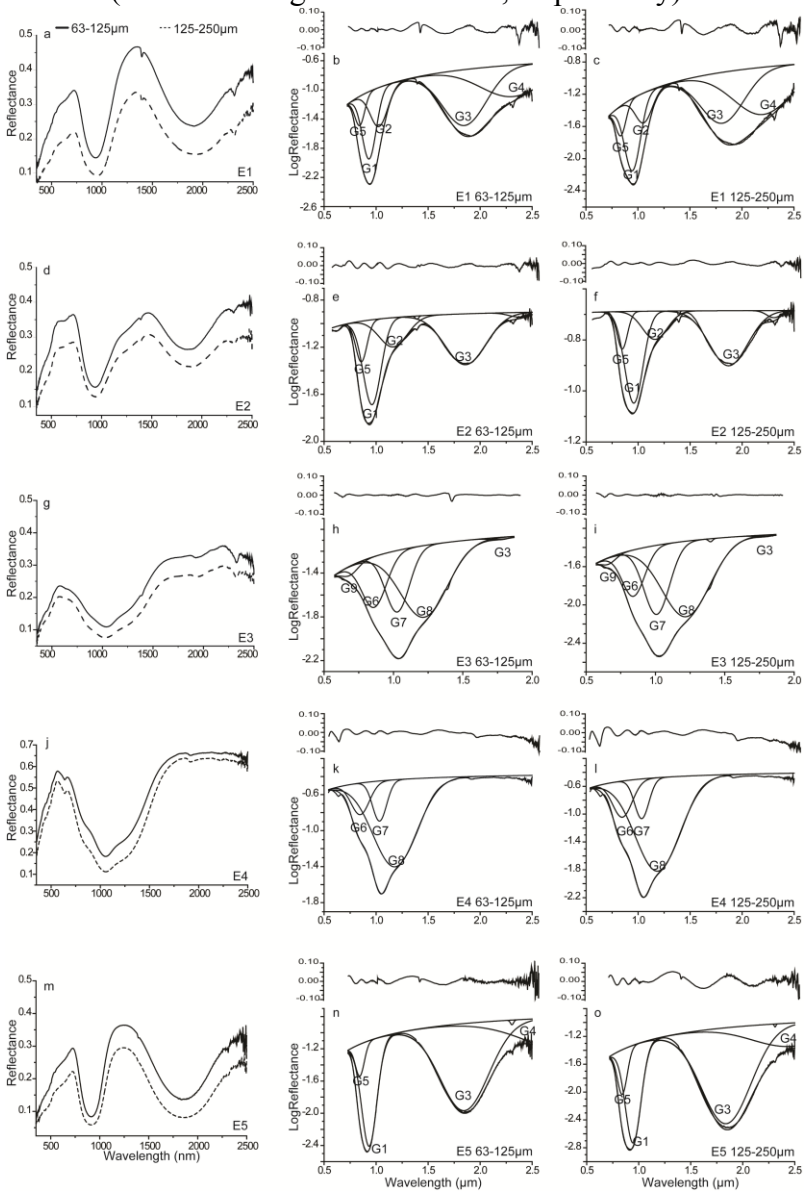

Fig. 8.9 The figure shows the mafic end-members and their MGM deconvolution at two different particle size (from Serventi et al., 2015), 63-125 µm (solid spectrum; central column) and 125-250 µm (dashed spectrum; right column). a-c) E1 end-member is decomposed with 5 Gaussians, 3 in the 800-1000 nm range, G1 for Fe^{2+} in OPX, G2 for Fe^{2+} in CPX and G5 for adjustment, and 2 in the NIR range, G3 for Fe^{2+} in OPX and G4 for Fe^{2+} in CPX; d-f) E2 end-member is decomposed with 4 main Gaussians, G1, G2 and G5 in the 800-1200 nm range for the Fe^{2+} transitions in the olivine M1 and M2 sites and G3 at ~1850 nm for the Fe^{2+} in OPX; g-i) E3 end-member is deconvolved with 3 Gaussians assigned to Fe^{2+} transitions in the olivine M1 (G6 and G8) and M2 (G7) sites; j-l) E4 end-member is decomposed with 3 Gaussians, G6, G7 and G8, as in the previous end-members, even if the Gaussian relative strength in this case is very different; m-o) E5 end-member is deconvolved with 4 Gaussians, 2 in the 800-1000 nm range, G1 for Fe^{2+} in OPX and G5 for adjustment, and 2 in the NIR range, G3 for Fe^{2+} in OPX and G4 for adjustment.

In Tab. 8.2 are reported the spectral parameters for each mafic end-member.

		E1						
	Center	Width	Depth	RMS	Center	Width	Depth	RMS
G5	843	110	-0.4007		837	113	-0.3706	
G1	934	159	-0.9294		949	180	-0.8958	
G2	1028	199	-0.5359		1058	191	-0.3715	
G3	1851	496	-0.7669		1813	489	-0.6319	
G4	2311	730	-0.4315		2202	678	-0.5865	
				0.018				0.020
		E2						
	Center	Width	Depth	RMS	Center	Width	Depth	RMS
G5	858	127	-0.342		848	117	-0.1465	
G1	961	202	-0.7214		959	206	-0.3596	
G2	1165	320	-0.2488		1162	281	-0.1108	
G3	1859	463	-0.4321		1870	433	-0.2157	
				0.010				0.009
				E3				
	Center	Width	Depth	RMS	Center	Width	Depth	RMS
G6	861	210	-0.4645		842	193	-0.4839	
G7	1028	204	-0.5626		1009	218	-0.7225	
G8	1221	400	-0.6557		1221	408	-0.7893	
				0.005				0.003
		E4						
	Center	Width	Depth	RMS	Center	Width	Depth	RMS
G6	848	220	-0.3506		849	237	-0.5192	
G7	1033	170	-0.4452		1035	173	-0.5702	
G8	1181	534	-0.9666		1188	542	-1.343	
				0.019				0.029
		E5						
	Center	Width	Depth	RMS	Center	Width	Depth	RMS
G5	844	101	-0.3952		842	111	-0.6415	
G1	934	173	-1.311		947	176	-1.404	
G3	1849	548	-1.081		1842	559	-1.379	
				0.018				0.025

Tab. 8.2 In table are reported the spectral parameters obteined by MGM deconvolution of mafic end-members, at the 63-125 µm (on the left) and 125-250 µm (on the rigth). Center and width are expressed in nanometers, while depth as the logarithm of the reflectance. RMS represent the Root Mean Square error: the lower the RMS the better the fit.

For the PX-bearing end-members, a Gaussian centered at ca. 840 nm, G5, has been added. In the literature, Sunshine and Pieters (1993) inserted a Gaussian at ca. 800 nm for OPX spectra acquired on 75-125 µm size, which was not considered for the same material at fine sizes, demonstrating how only increasing the size the MGM fit requires an additional Gaussian in that spectral region. So, here, G5 has been interpreted as a Gaussian that adjusts the absorption band shape and is not assigned to a particular crystal field transition; for this reason, G5 is not considered in the following discussions.

Furthermore, in E3 end-member we needed to add the Guassian G9 at ca. 650 nm in order to obtain a better fit. This band is representative of a IVCT absorption (Burns, 1993), but will not be taken in to account in the further discussion.
In particular, for the 63-125 μm particle size (central column in the figure):

1) E1 band I is deconvolved with 2 Gaussians (Fig. 8.9a,b): G1 at 934 nm for Fe^{2+} transition in the OPX M2 site, and G2 at 1028 nm for the Fe^{2+} transition in the CPX M1 site; band II has been fitted with 2 Guassians, G3 at 1851 nm for Fe^{2+} transition in the OPX M2 site, and G4 at 2311 nm for the Fe^{2+} transition in the CPX M2 site;
2) E2 is deconvolved with 2 Gaussians for the absorption band at ~950 nm (Fig. 8.9d,e): G1 at 961 nm for the composite absorption due to Fe^{2+} transition in OPX M2 site and in OL M1 and M2 sites, and G2 at 1165 nm for the Fe^{2+} transition in the OL M1 site; 1 Guassian, G3 at 1859 nm, describes the ~1850 nm band, for the Fe^{2+} transition in the OPX M2 site;
3) E3 is deconvolved with 3 Gaussians (Fig. 8.9g,h) for the Fe^{2+} transition in OPX M2 site (G6 at 861 nm) and in M1 (G6 and G8 at 861 nm and 1221 nm, respectively) and M2 (G7 at 1028 nm) sites in OL;
4) E4 is deconvolved with 3 Gaussians for the Fe^{2+} transition in M2 (G7 at 1033 nm) and M1 (G6 and G9 at 848 nm and 1181 nm, respectively) sites in OL (Fig. 8.9j.k); and
5) E5 is deconvolved with 1 Gaussian for the absorption band I (Fig. 8.9m,n), G1, at 934 nm for Fe^{2+} transition in the OPX M2 site; and 1 Guassian, G3, at 1849 nm, for the Band II, describing the Fe^{2+} transition in the OPX M2 site.

E3 and E4 end-members are both composed mainly of OL, 70% and 100% respectively, but the Gaussians assigned to E4 show a different behavior with respect to the ones in E3. In E4 end-member, G8 is almost twice deeper than G6 and G7, while in E3 the depth differences are reduced. The different OL composition and iron content in E3 and E4 and the presence of circa 30% OPX in E3, can explain this different spectral behavior.
On the top of each MGM plot we report the fit's residual. The residual shows the difference between measured and fitted spectra. It is clear from the literature (e.g. Sunshine et al., 1990; Sunshine and Pieters, 1993) that the residual error present in our plot can be considered due not to missing Gaussians, but regarded as typical MGM residual error associated maybe to band saturation or to the mathematical statistics of this approach, or related to our choice of fixing spectral parameters, such as band center and band width. Furthermore, the intensity of the residual, ±0.1, indicates values comparable with Klima et al. (2011).

8.3.2 Plagioclase deconvolution

Fig. 8.9a-i and Tab. 8.3 show the deconvolution of the PL at the two different particle sizes. Each PL has been decomposed assigning a principal Gaussian (G10) for the absorption band at ~ 1250 nm. Furthermore, it is necessary to add a Gaussian (G11) in the 1600-1800 nm region, here called the 1800 nm Gaussian, in order to model the asymmetry due to flattening of the long-wavelength shoulder of the 1250 nm band towards the IR. However, an 1800 nm absorption band, even if described in literature (Pieters, 1996; Hiroi et al., 2012), has not been interpreted and is still unassigned to a specific transition in the PL crystal structure. Gaussians describing the vibrational modes at approximately 1400, 1900 and 2300 nm, due to the OH- alterations of natural PL, are not considered in further discussions. The residuals show a very weak pattern for both the particle size, suggesting that the spectra are well fit, as indicated by also the R^2 values in Tab. 8.3.
From Tab. 8.3 it is evident that, for the 63-125 μm particle size (filled symbols in figure), increasing the FeO content in PL:

a) G10 deepens from PL 1 to PL2, while it slightly decreases from PL2 to PL3; G11 deepens;
b) G10 center is very similar for PL1 and PL2 while in PL3 it moves towards longer wavelengths; G11 moves towards the IR region from PL1 to PL2 while it shifts towards shorter wavelengths from PL2 to PL3;
c) G10 width does not show significant variations while G11 band widens; and
d) co becomes more negative while c1 becomes positive.

Coarsening the particle size, G10 deepens and moves slightly towards the IR region while the width does not show a defined trend. On the other hand, G11 deepens, moves towards shorter wavelengths and broadens. C0 values are more negative while c1 are more positive (except from PL1) with respect to the fine particle size.

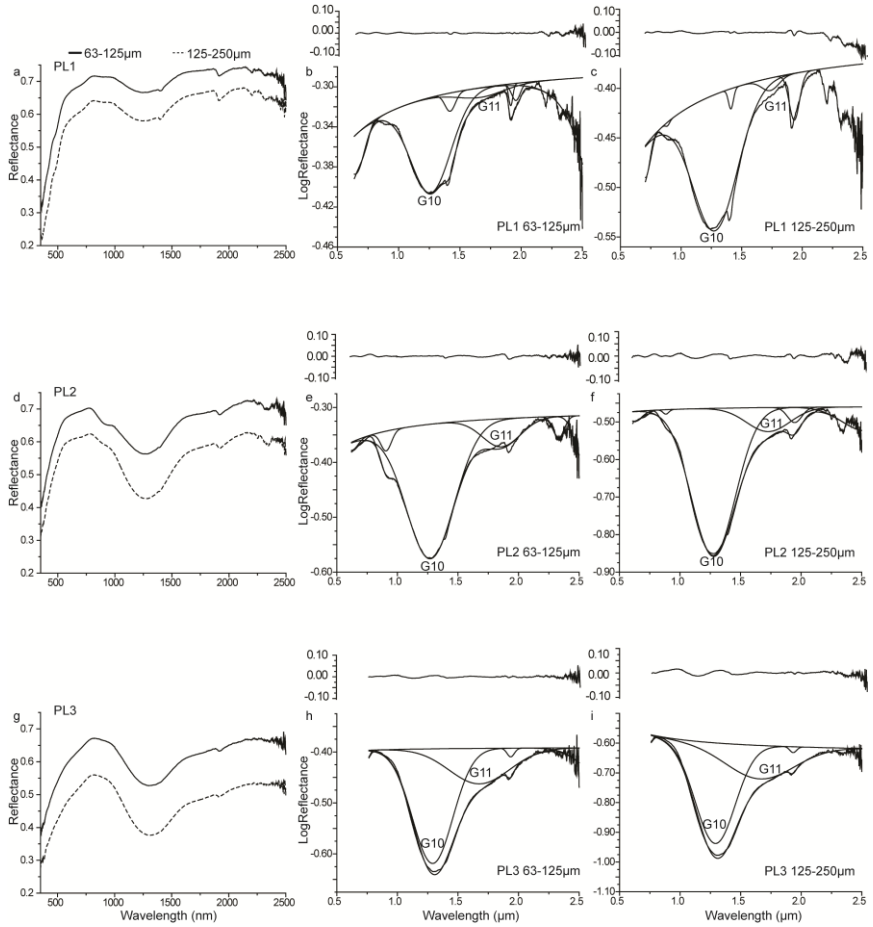

Fig. 8.9 The figure shows the PL end-members used in this paper and their MGM deconvolution at two different particle size (from Serventi et al., 2015), 63-125 μm (solid spectrum; central column) and 125-250 μm (dashed spectrum; right column). a-c) PL1 is decomposed with G10 centered at ca. 1200-1250 nm for the Fe^{2+} in PL, and G11 in the 1600-1800 nm spectral region; d-f) PL2 is decomposed with G10 centered at ca. 1200-1250 nm for the Fe^{2+} in PL, G11 at ca. 1800 nm and other Gaussian for the vibrational bands due to OH alteration; g-i) PL3 is decomposed with G10 centered at ca. 1200-1250 nm for the Fe^{2+} in PL, G11 at ca. 1800 nm. Gaussians describing the vibrational bands due to OH alteration are not described in the text and in the discussions.

		PL1						
	Center	Width	Depth	RMS	Center	Width	Depth	RMS
G10	1276	440	-0.0936		1282	478	-0.1382	
G11	1750	168	-0.0055		1739	189	-0.01288	
				0.0017				0.005
		PL2						
	Center	Width	Depth	RMS	Center	Width	Depth	RMS
G10	1271	505	-0.2439		1282	481	-0.3919	
G11	1837	443	-0.04704		1822	441	-0.06778	
				0.005				0.009
		PL3						
	Center	Width	Depth	RMS	Center	Width	Depth	RMS
G10	1298	438	-0.2356		1295	431	-0.3598	
G11	1734	591	-0.06649		1711	636	-0.1066	
				0.005				0.007

Tab. 8.3 In table are reported the spectral parameters obteined by MGM deconvolution of PL, at the 63-125 μm and 125-250 μm. Center and width are expressed in nanometers, while depth as the logarithm of the reflectance. RMS represent the Root Mean Square error: the lower the RMS the better the fit.

8.4 Mixtures deconvolution

8.4.1 E1+PL mixtures

In these mixtures, in which the mafic end-member consists of OPX+CPX, the 1250 nm Gaussian is fully representative of the PL.

Fig. 8.11 shows the spectral parameter variations of the 1250 nm PL band and the OPX, CPX mafic bands in mixtures (Fig. 8.11f,g). In particular, with increasing vol. FeO % content in the three PL species, for the 63-125μm particle size (filled symbols in Fig. 8.11):

1) PL band deepens(Fig. 8.11a) with linear trend and R^2 values >0.89, even if the band depth is very reduced in PL1-bearing mixtures;
2) PL band center moves towards longer wavelengths (Fig. 8.11b). PL band centers of all mixtures have an unique, linear trend for all PL compositions with high correlation coefficients, R^2 =0.939, (Fig. 8.11b solid line); the outliers represent the 90% PL1 mixture and PL1;
3) PL band width increases with trend and R^2 values similar to the band depth (Fig. 8.11c). The figure also shows that PL1-mixtures band width is less broad than PL2 and PL3, that, in contrast, display very similar values;
4) the continuum intercept c0 becomes negative but for vol. FeO% in PL > 0.25 it moves towards positive values (Fig. 8.11d), while c1 always moves towards positive values (Fig. 8.11e);
5) mafic mineral band depths decrease with linear trends, for both the OPX band I and II and the CPX band (Fig. 8.11f,g and with R^2 between 0.97 and 0.99.;
6) mafic band depths result correlated to the PL chemistry: Fig. 8.16a shows that, considering mixtures with the same mafic abundance, bands representative of the same process are deeper in PL1-mixtures (light colors) than in PL3-mixtures (dark colors).

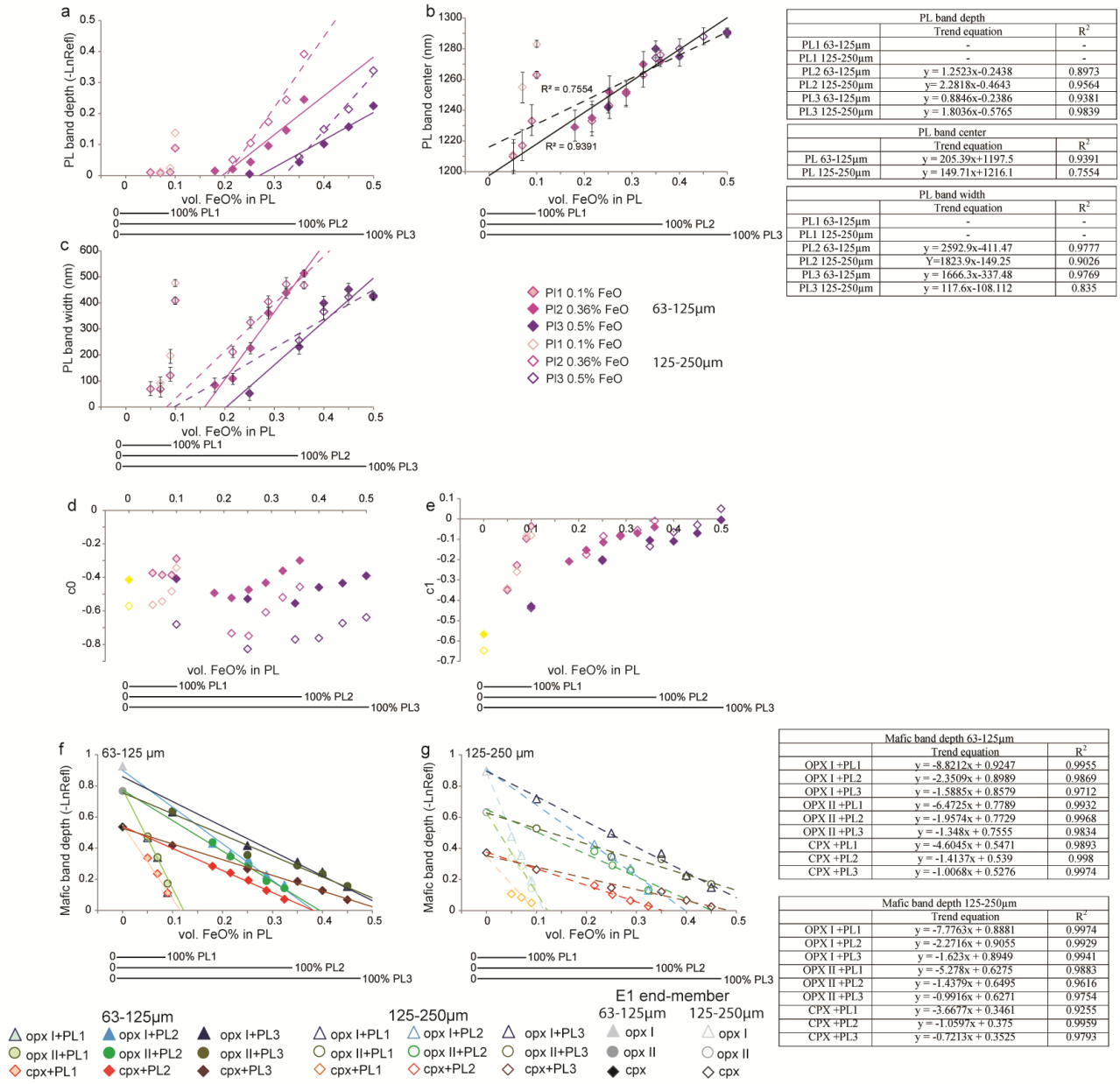

PL band depth		
	Trend equation	R^2
PL1 63-125µm	-	-
PL1 125-250µm	-	-
PL2 63-125µm	y = 1.2523x-0.2438	0.8973
PL2 125-250µm	y= 2.2818x-0.4643	0.9564
PL3 63-125µm	y = 0.8846x-0.2386	0.9381
PL3 125-250µm	y = 1.8036x-0.5765	0.9839

PL band center		
	Trend equation	R^2
PL 63-125µm	y = 205.39x+1197.5	0.9391
PL 125-250µm	y = 149.71x+1216.1	0.7554

PL band width		
	Trend equation	R^2
PL1 63-125µm	-	-
PL1 125-250µm	-	-
PL2 63-125µm	y = 2592.9x-411.47	0.9777
PL2 125-250µm	Y=1823.9x-149.25	0.9026
PL3 63-125µm	y = 1666.3x-337.48	0.9769
PL3 125-250µm	y = 117.6x-108.112	0.835

Mafic band depth 63-125µm		
	Trend equation	R^2
OPX I +PL1	y = -8.8212x + 0.9247	0.9955
OPX I +PL2	y = -2.3509x + 0.8989	0.9869
OPX I +PL3	y = -1.5885x + 0.8579	0.9712
OPX II +PL1	y = -6.4725x + 0.7789	0.9932
OPX II +PL2	y = -1.9574x + 0.7729	0.9968
OPX II +PL3	y = -1.348x + 0.7555	0.9834
CPX +PL1	y = -4.6045x + 0.5471	0.9893
CPX +PL2	y = -1.4137x + 0.539	0.998
CPX +PL3	y = -1.0068x + 0.5276	0.9974

Mafic band depth 125-250µm		
	Trend equation	R^2
OPX I +PL1	y = -7.7763x + 0.8881	0.9974
OPX I +PL2	y = -2.2716x + 0.9055	0.9929
OPX I +PL3	y = -1.623x + 0.8949	0.9941
OPX II +PL1	y = -5.278x + 0.6275	0.9883
OPX II +PL2	y = -1.4379x + 0.6495	0.9616
OPX II +PL3	y = -0.9916x + 0.6271	0.9754
CPX +PL1	y = -3.6677x + 0.3461	0.9255
CPX +PL2	y = -1.0597x + 0.375	0.9959
CPX +PL3	y = -0.7213x + 0.3525	0.9793

Fig. 8.11 The figure shows the spectral parameter variations in mixtures composed with E1 and PL (from Serventi et al., 2015). Filled symbols: 63-125 µm; empty symbols: 125-250 µm. In particular, with increasing the volumetric FeO% in PL: a) the PL band depth deepens and mixtures with different PL have different band depth. A coarse particle size (empty symbols) deepens the absorption bands; b) the PL band center moves towards longer wavelength with correlation curves with high R^2 , with the exception of the outliers indicated in the square and representing 90% PL1-mixtures and PL1 end-members; c) the PL band width broadens; d,e) co moves towards positive values only for FeO vol. % in PL>0.25, while c1 become less negative; f,g) mafic mineral (OPX, CPX) absorption bands decrease with linear, high correlated, trends. OPX band I is deeper than OPX band II, while CPX band is the weakest band. Vertical error bars not shown in the figure: PL band depth ± 0.005 LnRefl; mafic band depth ± 0.001 LnRefl.

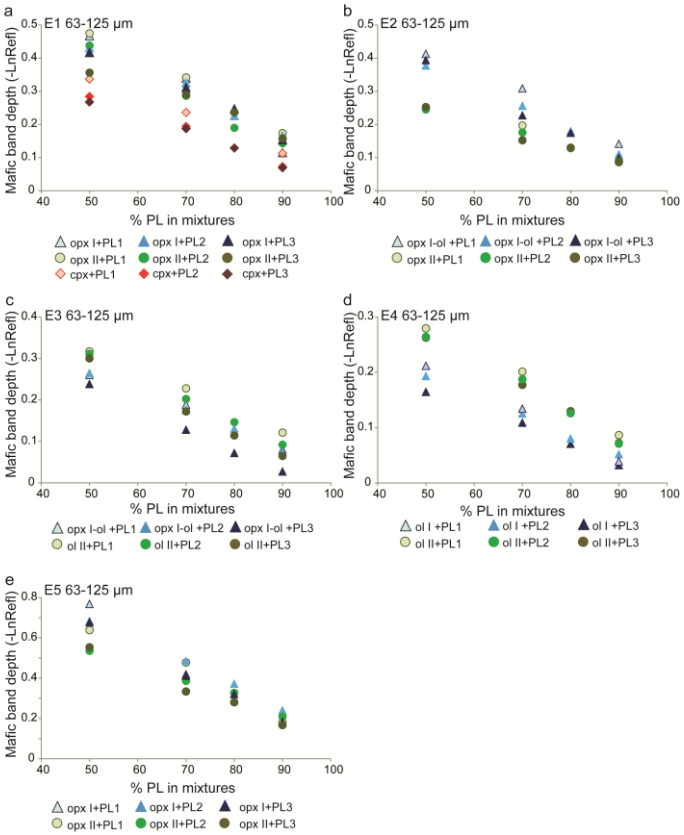

Fig. 8.16 The figure shows the mafic band depth for mixtures composed with the same modal abundance but with different PL chemistry, for the 63-125 µm particle size. a) E1+PL mixtures; b) E2+PL mixtures; c) E3+PL mixtures; d) E4+PL mixtures; and 5) E5+PL mixtures . For each mixture, mafic bands relative to the same process are deeper in PL1-mixtures than in PL3 mixtures (from Serventi et al., 2015).

The general trends of band center (empty symbols in Fig. 8.11b) are similar for the coarse and fine mixtures, but the band in coarse mixtures (empty symbols in Fig. 8.11a) are deeper. The band widths are larger in coarse PL1 and PL2 mixtures, and narrower in coarse PL3 mixtures (Fig. 8.11c). c0 is always more negative while c1 shows scattered variations, with respect to the 63-125 µm size. The correlation curves are very similar to those found for the fine particle size mixtures, even if the R^2 values are slightly lower.

The effects of PL chemistry on the PL band spectral parameters are also displayed in the figures. Increasing Fe^{2+} in PL, the band deepens (Fig. 8.11a), the center band shifts towards the IR spectral region (Fig. 8.11b) and the band width widens (Fig. 8.11c).

8.4.2 E2+PL mixtures

In these mixtures, PL and OL absorb in the same spectral range, thus a COMP absorption band in the 1250 nm region is here considered. In the same way, OPX band I and OL band 1 and 2 are considered as a complex absorption band, here indicated as OPX+OL band I.

Fig. 8.12 shows that, increasing the vol. FeO% due to PL:

1) for 63-125μm mixtures, COMP band depth decreases in PL1 mixtures with a linear trend and R^2 =0.979, but it slightly decreases and then increases in PL2 and PL3 mixtures with a resulting parabolic trend and with R^2 between 0.904 and 0.989 (filled symbols in Fig. 8.12a). Band depth increases in coarse mixtures (empty symbols in Fig. 8.12a) with second-degree polynomial curves and with worse R^2 ranging between 0.696 and 0.925. This behavior points out the different PL importance in different particle sizes: in coarse mixtures, the effects of transparent PL are emphasized, and, consequently, COMP band deepens (see also Fig. 8.12a).
2) COMP band center moves towards longer wavelengths with a linear trend and very high R^2 values for all PL compositions, with the exception of the 90% PL1-bearing mixture and the PL1, at both particle sizes (Fig.8.12b);
3) COMP band width is slightly widening, mostly for the coarse mixtures (Fig. 8.12c);
4) c0 and c1 become less negative (Figs. 8.12d,e);
5) OPX+OL band I and OPX band II depth decrease as expected, with a linear trend both in the fine and in the coarse mixtures, both with high R^2 from 0.89 to 0.99. (Fig.8.12f,g);
6) mafic band depths result correlated to the PL chemistry: Fig. 8.16b shows that, considering mixtures with the same mafic abundance, bands are deeper in PL1-mixtures (light colors) than in PL3-mixtures (dark colors).

In general, increasing Fe^{2+} content in PL the COMP band in PL2 and PL3 mixtures is deeper than in PL1 bearing-mixtures, even if in PL2 mixtures it is slightly deeper than in PL3 ones; the COMP band center shifts to longer wavelengths and the band width is wider.

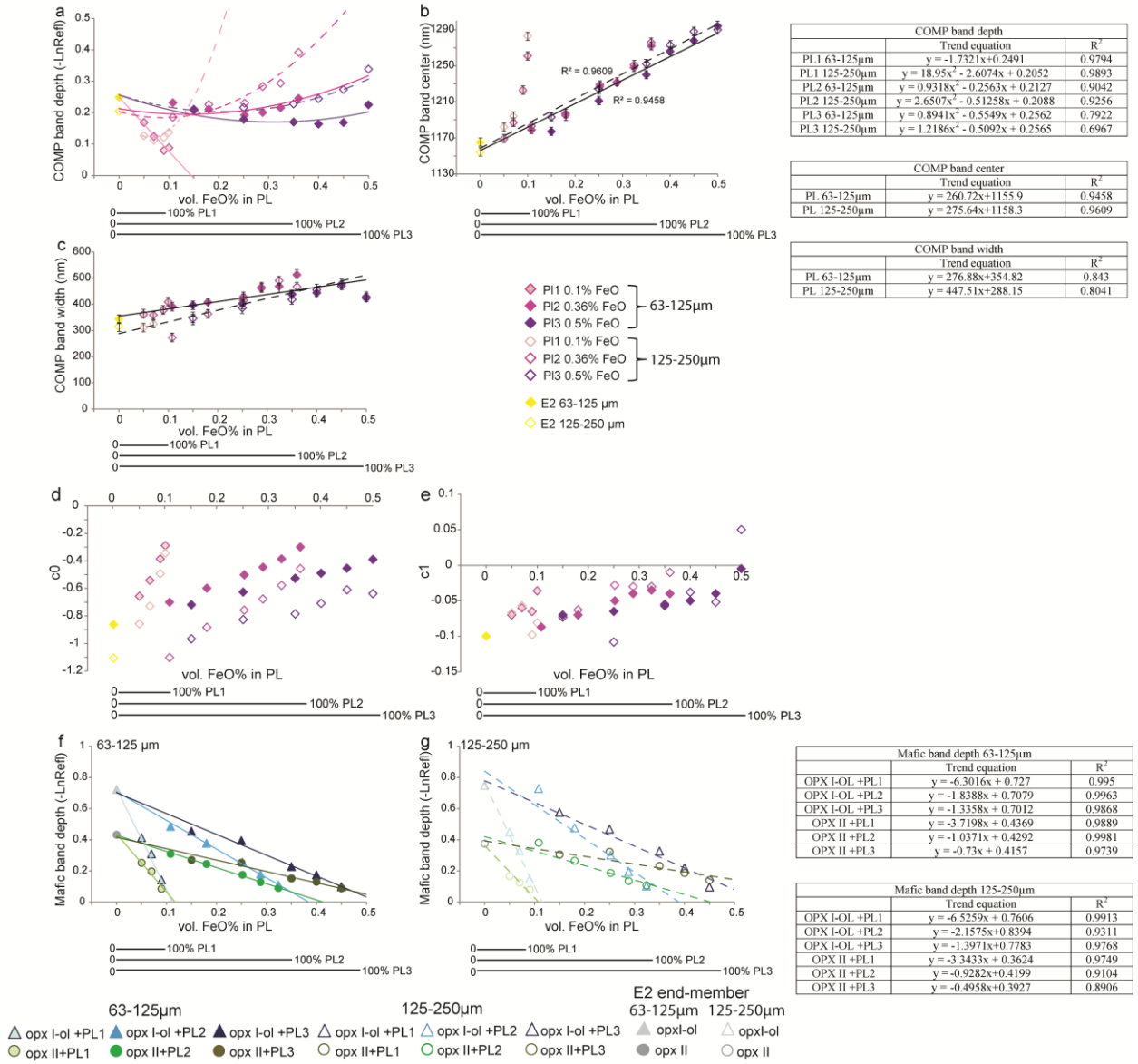

COMP band depth		
	Trend equation	R^2
PL1 63-125µm	y = -1.7321x+0.2491	0.9794
PL1 125-250µm	y = 18.95x² - 2.6074x + 0.2052	0.9893
PL2 63-125µm	y = 0.9318x² - 0.2563x + 0.2127	0.9042
PL2 125-250µm	y = 2.6507x² - 0.51258x + 0.2088	0.9256
PL3 63-125µm	y = 0.8941x² - 0.5549x + 0.2562	0.7922
PL3 125-250µm	y = 1.2186x² - 0.5092x + 0.2565	0.6967

COMP band center		
	Trend equation	R^2
PL 63-125µm	y = 260.72x+1155.9	0.9458
PL 125-250µm	y = 275.64x+1158.3	0.9609

COMP band width		
	Trend equation	R^2
PL 63-125µm	y = 276.88x+354.82	0.843
PL 125-250µm	y = 447.51x+288.15	0.8041

Mafic band depth 63-125µm		
	Trend equation	R^2
OPX I-OL +PL1	y = -6.3016x + 0.727	0.995
OPX I-OL +PL2	y = -1.8388x + 0.7079	0.9963
OPX I-OL +PL3	y = -1.3358x + 0.7012	0.9868
OPX II +PL1	y = -3.7198x + 0.4369	0.9889
OPX II +PL2	y = -1.0371x + 0.4292	0.9981
OPX II +PL3	y = -0.73x + 0.4157	0.9739

Mafic band depth 125-250µm		
	Trend equation	R^2
OPX I-OL +PL1	y = -6.5259x + 0.7606	0.9913
OPX I-OL +PL2	y = -2.1575x+0.8394	0.9311
OPX I-OL +PL3	y = -1.3971x+0.7783	0.9768
OPX II +PL1	y = -3.3433x + 0.3624	0.9749
OPX II +PL2	y = -0.9282x+0.4199	0.9104
OPX II +PL3	y = -0.4958x+0.3927	0.8906

Fig. 8.12 The figure shows the spectral parameter variations in mixtures composed with E2 and PL (from Serventi et al., 2015). Filled symbols: 63-125 µm; empty symbols: 125-250 µm. Here we refer to a COMP band for the OL band 3 and PL absorption band. In particular, with increasing the volumetric FeO% in PL: a) COMP band depth decreases in PL1 fine mixtures, while it decreases and then increases in PL2 and PL3 fine mixtures. Coarsening the particle size (empty symbols) COMP band deepens and it is deeper with respect to the fine particle size; b) COMP band center moves towards longer wavelengths with correlation curves with high R^2, with the exception of the outliers indicated in the square and representing 90% PL1-mixtures and PL1 end-members; c) COMP band width broadens; d,e) co and c1, become less negative; f,g) mafic mineral (OPX, OL) absorption bands decrease with linear, high correlated, trends for both the particle sizes.
Vertical error bars not shown in the figure: COMP band depth ± 0.002 LnRefl; mafic band depth ± 0.001 LnRefl.

8.4.3 E3+PL mixtures

These mixtures are OL richer than the E2-bearing mixtures, and the presence of the COMP band at about 1250 nm is particularly well expressed.

In Fig. 8.13, increasing the vol. FeO% content due to PL, for the 63-125μm mixtures (filled symbols in figure) we observe:

1. COMP band depth decreases with distinct linear correlation curves and R^2 up to 0.937 for the three PL (Fig.8.13a). Differently from previous mixtures, E3-bearing mixtures the band depth constantly and linearly decreases, indicating that OL is spectroscopically dominant;
2. COMP band center moves towards longer wavelengths with an unique upward parabolic trend, with the exception of 90% PL1-mixture and PL1 (Fig.8.13b);
3. COMP band width does not show significant variations, even if a general, though slight, widening can be recognized (Fig. 8.13c) and, as in the previous mixtures, there is a unique trend of variation at each particle size;
4. c0 and c1 become less negative (Fig. 8.13d,e);
5. mafic band depths decrease with a linear trend and high R^2, with a steeper trend in PL1 mixtures than in PL2 and PL3-mixtures (Fig. 8.13f,g);
6. mafic band depths result correlated to the PL chemistry: Fig. 8.16c shows that, considering mixtures with the same mafic abundance, bands are deeper in PL1-mixtures (light colors) than in PL3-mixtures (dark colors).

Coarsening the particle size, the COMP band depth is always deeper (Fig. 8.13a), the center band is at slightly longer wavelengths (Fig. 8.13b) and the bands are wider (Fig. 8.13c) with respect to the 63-125 μm mixtures.

In general, increasing the Fe^{2+} content in PL the negative linear correlation curve between FeO and the COMP band depth has smaller angular coefficient, that is the angle formed between the correlation curve and the x-axis (Fig. 8.13a), the band center moves to longer wavelengths (Fig. 8.13b) and the band broadens (Fig. 8.16c).

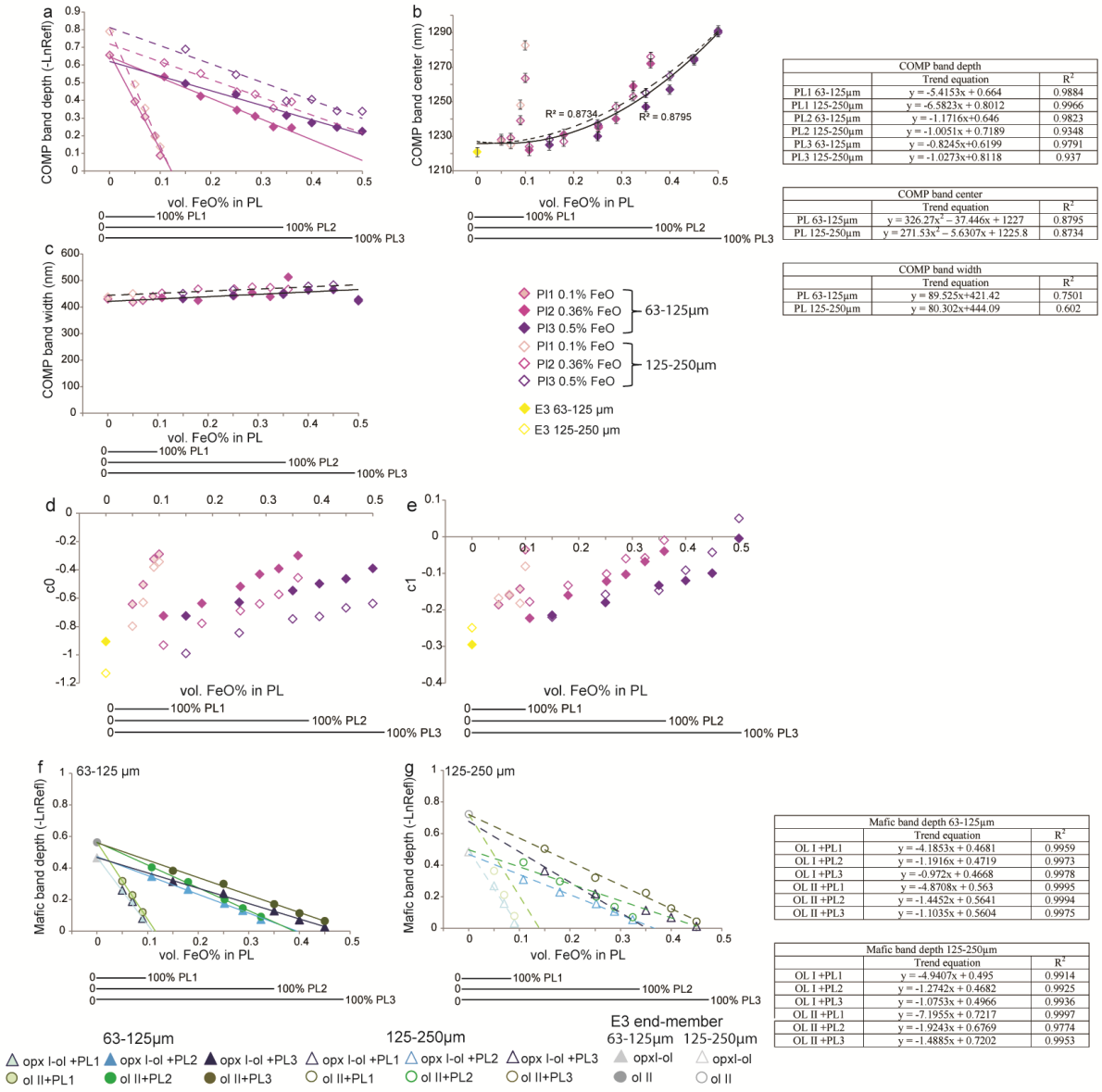

COMP band depth		
	Trend equation	R^2
PL1 63-125µm	y = -5.4153x + 0.664	0.9884
PL1 125-250µm	y = -6.5823x + 0.8012	0.9966
PL2 63-125µm	y = -1.1716x+0.646	0.9823
PL2 125-250µm	y = -1.0051x + 0.7189	0.9348
PL3 63-125µm	y = -0.8245x+0.6199	0.9791
PL3 125-250µm	y = -1.0273x+0.8118	0.937

COMP band center		
	Trend equation	R^2
PL 63-125µm	$y = 326.27x^2 - 37.446x + 1227$	0.8795
PL 125-250µm	$y = 271.53x^2 - 5.6307x + 1225.8$	0.8734

COMP band width		
	Trend equation	R^2
PL 63-125µm	y = 89.525x+421.42	0.7501
PL 125-250µm	y = 80.302x+444.09	0.602

Mafic band depth 63-125µm		
	Trend equation	R^2
OL I +PL1	y = -4.1853x + 0.4681	0.9959
OL I +PL2	y = -1.1916x + 0.4719	0.9973
OL I +PL3	y = -0.972x + 0.4668	0.9978
OL II +PL1	y = -4.8708x + 0.563	0.9995
OL II +PL2	y = -1.4452x + 0.5641	0.9994
OL II +PL3	y = -1.1035x + 0.5604	0.9975

Mafic band depth 125-250µm		
	Trend equation	R^2
OL I +PL1	y = -4.9407x + 0.495	0.9914
OL I +PL2	y = -1.2742x + 0.4682	0.9925
OL I +PL3	y = -1.0753x + 0.4966	0.9936
OL II +PL1	y = -7.1955x + 0.7217	0.9997
OL II +PL2	y = -1.9243x + 0.6769	0.9774
OL II +PL3	y = -1.4885x + 0.7202	0.9953

Fig. 8.13 The figure shows the spectral parameter variations in mixtures composed with E3 and PL (from Serventi et al., 2015). Filled symbols: 63-125 µm; empty symbols: 125-250 µm. Again, we refer to a COMP band for the OL band 3 and PL absorption band. In particular, with increasing the volumetric FeO% in PL: a) COMP band depth decreases in all the mixtures at both particle sizes. A coarse particle size (empty symbols) deepens the COMP band depth; b) COMP band center moves towards longer wavelengths with correlation curves with high R^2, with the exception of the outliers indicated in the square and representing 90% PL1-mixtures and PL1 end-members; c) COMP band width does not show significant variations; d,e) co and c1, become less negative; f,g) mafic mineral (OL) absorption bands decrease with linear, high correlated, trends.
Vertical error bars not shown in the figure: COMP band depth ± 0.0007 LnRefl; COMP band width ±2 nm; mafic band depth ± 0.001 LnRefl.

8.4.4 E4+PL mixtures

These mixtures are composed with PL and 100% OL-bearing end-member. In this case, 1800 nm absorption bands are not expected, due to the OPX absence. Nevertheless, a Gaussian is needed in this spectral region, particularly for PL2 and PL3 bearing mixtures, to account for a possible asymmetry of the 1250 nm absorption band.

Generally, increasing the FeO vol. content due to PL for the 63-125 μm mixtures (filled symbols in Fig. 8.14):

1) COMP band depth decreases with linear variation trends and high R^2 (pink filled symbols in Fig. 8.14a) while the 1800 nm band depth slightly increases with low correlation coefficients (orange filled symbols in Fig. 8.17a);
2) COMP band center moves towards longer wavelengths with parabolic trend (Fig. 8.14b), while the shallow 1800 nm center band shifts to shorter wavelengths, with a linear trend, with the exception of PL1-mixtures;
3) COMP band does not show variations and, therefore, a variation trend can't be defined, while the 1800 nm band widens (Fig. 8.14c). In this case, three different trends can be recognized for the different PL compositions;
4) c0 becomes more negative (Fig. 8.14d), differently from E1, E2 and E3-bearing mixtures, while c1 becomes slightly less negative (Fig. 8.14e);
5) OL band 1 and 2 become less intense with linear and highly correlated trends (Fig. 8.14f,g);
6) mafic band depths result correlated to the PL chemistry: Fig. 8.16d shows that, considering mixtures with the same mafic abundance, bands are deeper in PL1-mixtures (light colors) than in PL3-mixtures (dark colors).

Coarse particle size (empty symbols in Fig. 8.14a-c) produces a deeper and wider COMP absorption bands but a less deep, narrower and shifted towards longer wavelengths 1800 nm band.

Overall, increasing the Fe^{2+} content in PL, the COMP band depth decreases with a less inclined trend, while the 1800 nm band becomes more intense (Fig. 8.14a); the COMP band center moves towards longer wavelengths while the 1800 nm band shifts to shorter wavelengths (Fig. 8.14b); and both the bands are wider (Fig. 8.14c).

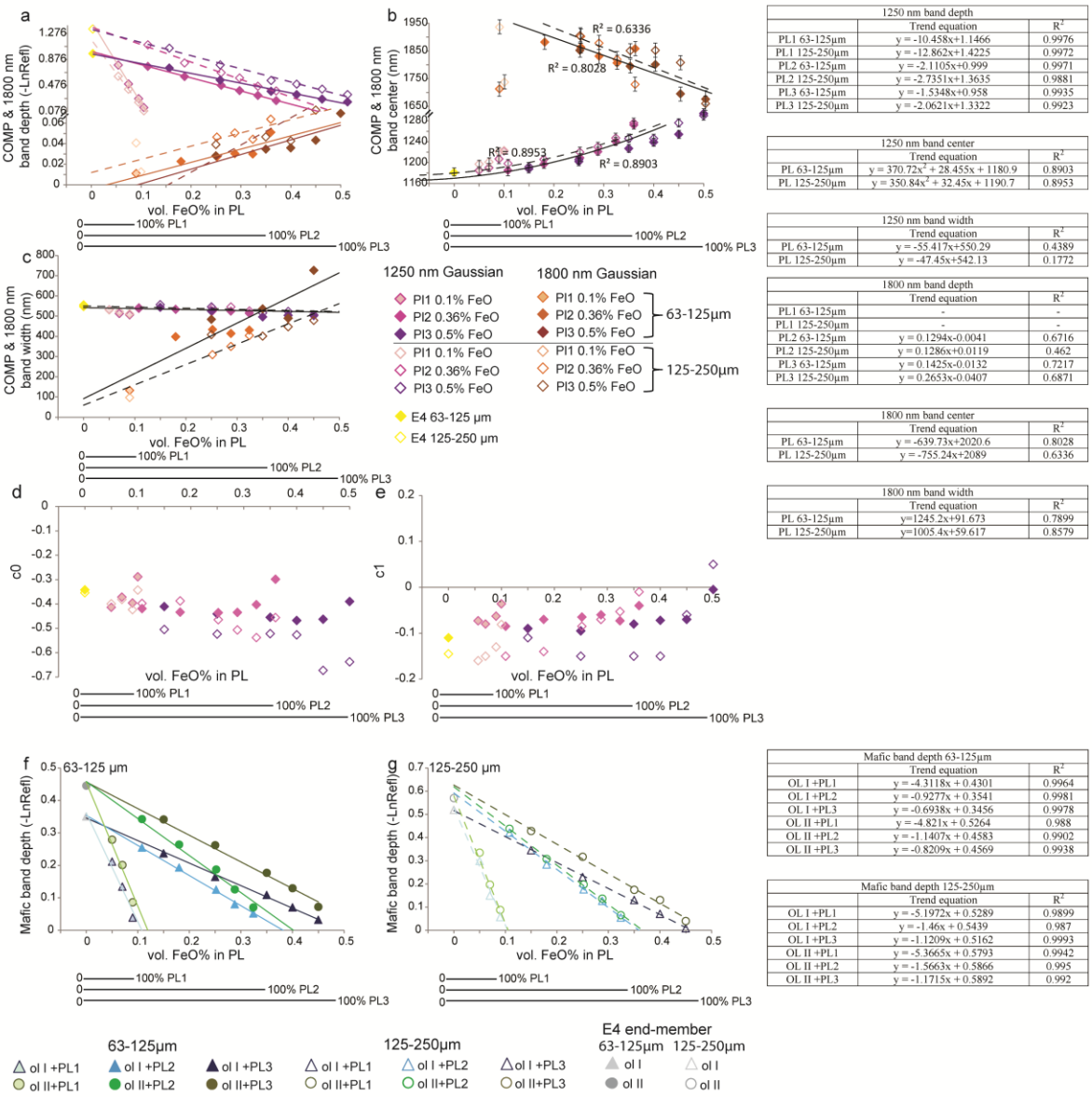

1250 nm band depth		
	Trend equation	R^2
PL1 63-125µm	y = -10.458x+1.1466	0.9976
PL1 125-250µm	y = -12.862x+1.4225	0.9972
PL2 63-125µm	y = -2.1105x+0.999	0.9971
PL2 125-250µm	y = -2.7351x+1.3635	0.9881
PL3 63-125µm	y = -1.5348x+0.958	0.9935
PL3 125-250µm	y = -2.0621x+1.3322	0.9923

1250 nm band center		
	Trend equation	R^2
PL 63-125µm	$y = 370.72x^2 + 28.455x + 1180.9$	0.8903
PL 125-250µm	$y = 350.84x^2 + 32.45x + 1190.7$	0.8953

1250 nm band width		
	Trend equation	R^2
PL 63-125µm	y = -55.417x+550.29	0.4389
PL 125-250µm	y = -47.45x+542.13	0.1772

1800 nm band depth		
	Trend equation	R^2
PL1 63-125µm	-	-
PL1 125-250µm	-	-
PL2 63-125µm	y = 0.1294x-0.0041	0.6716
PL2 125-250µm	y = 0.1286x+0.0119	0.462
PL3 63-125µm	y = 0.1425x-0.0132	0.7217
PL3 125-250µm	y = 0.2653x-0.0407	0.6871

1800 nm band center		
	Trend equation	R^2
PL 63-125µm	y = -639.73x+2020.6	0.8028
PL 125-250µm	y = -755.24x+2089	0.6336

1800 nm band width		
	Trend equation	R^2
PL 63-125µm	y=1245.2x+91.673	0.7899
PL 125-250µm	y=1005.4x+59.617	0.8579

Mafic band depth 63-125µm		
	Trend equation	R^2
OL I +PL1	y = -4.3118x + 0.4301	0.9964
OL I +PL2	y = -0.9277x + 0.3541	0.9981
OL I +PL3	y = -0.6938x + 0.3456	0.9978
OL II +PL1	y = -4.821x + 0.5264	0.988
OL II +PL2	y = -1.1407x + 0.4583	0.9902
OL II +PL3	y = -0.8209x + 0.4569	0.9938

Mafic band depth 125-250µm		
	Trend equation	R^2
OL I +PL1	y = -5.1972x + 0.5289	0.9899
OL I +PL2	y = -1.46x + 0.5439	0.987
OL I +PL3	y = -1.1209x + 0.5162	0.9993
OL II +PL1	y = -5.3665x + 0.5793	0.9942
OL II +PL2	y = -1.5663x + 0.5866	0.995
OL II +PL3	y = -1.1715x + 0.5892	0.992

Fig. 8.14 The figure shows the spectral parameter variations in mixtures composed with E4 and PL (from Serventi et al., 2015). Filled symbols: 63-125 µm; empty symbols: 125-250 µm. As in the previous mixtures, we refer to a COMP band for the OL band 3 and PL absorption band. A new Gaussian is here added, to take in to account the absorption/asymmetry in the 1800 nm spectral region. In particular, with increasing the volumetric FeO% in PL: a) COMP band depth decreases in all the mixtures at both particle sizes, while the 1800 nm band deepens. A coarse particle size (empty symbols) deepens both the band depth; b) COMP band center moves towards the IR region with correlation curves with high R^2, with the exception of the outliers indicated in the square and representing 90% PL1-mixtures and PL1 end-members. On the other hand, the 1800 nm band center moves towards shorter wavelengths but with a lesser correlated fit with respect to the COMP band center variation; c) COMP band width does not show variations while the 1800 nm band width become significantly wider; d,e) c0 becomes more negative while c1 become less negative; f,g) mafic mineral (OL) absorption bands decrease with linear, high correlated, trends for both particle sizes. Vertical error bars not shown in the figure: COMP band depth ± 0.0015 LnRefl; COMP band width ±5 nm; mafic band depth ± 0.001 LnRefl.

8.4.5 E5+PL mixtures

E5 end-member is totally composed with OPX, so that the mafic and PL absorption bands are well separated.

Fig. 8.15 shows that, increasing the vol. FeO% due to PL for the 63-125 μm mixtures (filled symbols in the figure):

1) PL band depth deepens with linear trend and R^2>0.84 (Fig. 8.15a);
2) PL band moves towards longer wavelengths with R^2=0.735 (Fig. 8.15b), with the exception of 90% PL1;
3) PL band width broadens (Fig. 8.15c), very similarly to the band width in E1 mixtures;
4) c0 and c1 become less negative (Figs. 8.15d,e);
5) OPX band I and II become less intense with linear trends(Fig. 8.15f,g);
6) mafic band depths result correlated to the PL chemistry: Fig. 8.16e shows that, considering mixtures with the same mafic abundance, bands are deeper in PL1-mixtures (light colors) than in PL3-mixtures (dark colors).

Coarsening the particle size (empty symbols in Fig. 8.15), PL band deepens, the center band shifts to longer wavelengths and the bands are only slightly wider than the 63-125 μm size.

In general, increasing Fe^{2+} content in PL, PL absorption band in PL2 and PL3-bearing mixtures are deeper and wider than in PL1 mixtures (Fig. 8.15a,c) and center band shifts towards the IR spectral range (Fig. 8.15b).

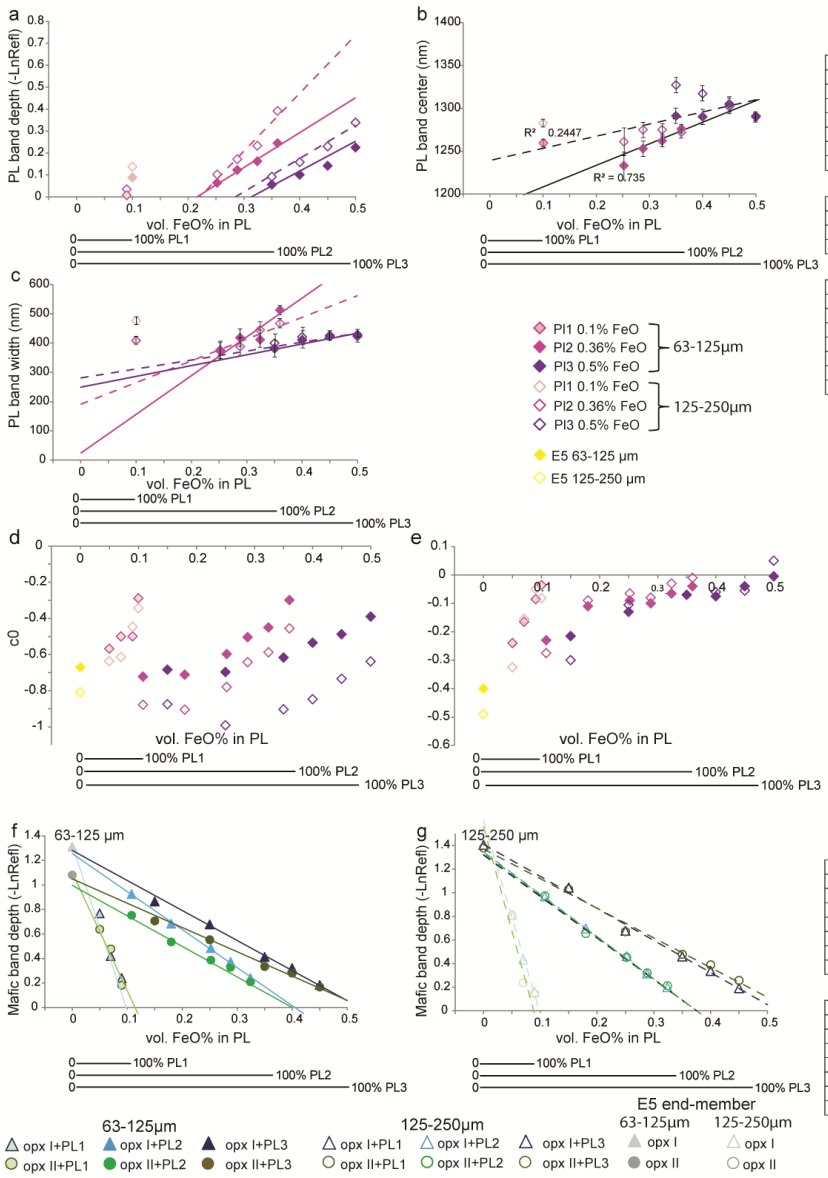

PL band depth		
	Trend equation	R^2
PL1 63-125µm	-	-
PL1 125-250µm	-	-
PL2 63-125µm	y = 1.6209x-0.3475	0.9805
PL2 125-250µm	y = 2.5868x-0.5667	0.9455
PL3 63-125µm	y = 1.7757x-0.5955	0.8489
PL3 125-250µm	y = 1.6205x-0.4841	0.9852

PL band center		
	Trend equation	R^2
PL 63-125µm	y = 250.05x+1183.6	0.735
PL 125-250µm	y = 141.26x+1238.4	0.2447

PL band width		
	Trend equation	R^2
PL1 63-125µm	-	-
PL1 125-250µm	-	-
PL2 63-125µm	y = 1063.5x+109.93	0.8072
PL2 125-250µm	y = 884.37x+153.28	0.9324
PL3 63-125µm	y = 305.79x+280.84	0.8908
PL3 125-250µm	y = 228.59x+318.29	0.6442

Mafic band depth 63-125µm		
	Trend equation	R^2
OPX I +PL1	y = -12.158x + 1.3229	0.9912
OPX I +PL2	y = -3.1023x + 1.2559	0.9982
OPX I +PL3	y = -2.4496x + 1.2817	0.9956
OPX II +PL1	y = -9.6447x + 1.1012	0.9856
OPX II +PL2	y = -2.4069x + 0.997	0.9904
OPX II +PL3	y = -1.9818x + 1.0489	0.9926

Mafic band depth 125-250µm		
	Trend equation	R^2
OPX I +PL1	y = -16.325x + 1.6178	0.9965
OPX I +PL2	y = -3.5482x + 1.3456	0.9991
OPX I +PL3	y = -2.7144x + 1.4094	0.9953
OPX II +PL1	y = -16.618x + 1.5215	0.7217
OPX II +PL2	y = -3.4595x + 1.3204	0.9925
OPX II +PL3	y = -2.5112x + 1.3703	0.9917

Fig. 8.15 The figure shows the spectral parameter variations in mixtures composed with E5 and PL (from Serventi et al., 2015). Filled symbols: 63-125 µm; empty symbols: 125-250 µm. In particular, with increasing the volumetric FeO% in PL: a) the PL band depth deepens and mixtures with different PL have different band depth. A coarse particle size (empty symbols) deepens the absorption bands compared to the fine size; b) the PL band center moves towards the IR region but with correlation curves with low R^2, with the exception of the PL1-bearing mixtures; c) the PL band width broadens; d,e) co and, above all, c1, become less negative; f,g) mafic mineral (OPX) absorption bands decrease with linear, high correlated, trends for both particle sizes. Vertical error bars not shown in the figure: PL band depth ± 0.004 LnRefl; mafic band depth ± 0.001 LnRefl.

8.4.6 Comparison between the mixtures

The spectral parameters behavior are shown in Fig. 18a-c, relative to mixtures in which the mafic end-member composition is characterized by increasing OL content from E2 to E4.

In general, Fig. 8.17a shows the clear change in the spectral behavior of the PL-bearing mixtures occurring at 0.1 vol. FeO% in PL, separating the control of low Fe^{2+} content PL from that of intermediate and high Fe^{2+} content. Within each of the three domains, due to the PL chemistry, the variation of vol. FeO % in PL produces the distinct correlation curves for PL1, PL2 and PL3-bearing mixtures described in previous sections, but some parameters of these curves are dictated by the mafic component chemistry. In fact, in Fig. 8.17a increasing vol. FeO% content due to PL:

1. For the low iron content PL1 (0.1 wt.% FeO) mixtures, the band depth decreases although with increasing rates for increasing OL content in the mafic component;
2. The PL2 and PL3 produce negative band depth trends for the E3 and E4 mafic composition and an almost invariable band depth for the E2 mixtures. In synthesis, the rate of the variation curve apparently depends on the mafic component chemistry more than on PL chemistry.

Fig. 8.17b displays the different behavior of the COMP band center according to the volumetric FeO% content in PL. In particular:

1) Between 0 and 0.15 vol. FeO% content there are the effects of increasing PL1 content in the mixtures, with the COMP band center moving to longer wavelengths from E2-mixtures, to E4-mixtures to E3-mixtures. The band center in E2-mixtures is at shorter wavelengths than in E4-mixtures due to the higher amount of OPX, while in E3-mixtures the band center is at longer wavelengths than in E4-mixtures even if E3 is composed of OPX. This can be due to the E3 olivine iron-richer chemistry than in E4, thus resulting in absorption bands at longer wavelength, presumably consistent with lower OL content;
2) For 0.15 < vol. FeO% > 0.35, the E3 (E3+PL2/PL3) and E4 (E4+PL2/PL3) bearing mixtures form two groups, with positive trends, with the E3-mixture band centers at longer wavelength;
3) The E2+PL3 mixtures have a variation trend with a high angular coefficient that intersects that of E3 + PL3 at about 0.35 vol. FeO%. This indicates that in E2, that contains a lower amount of OL with respect to E3 and E4, the effect of PL is spectroscopically more important.
4) As a consequence, the E2+PL3 mixtures converge with the E4+PL2 at about 1210 nm for 0.25 vol. FeO% in PL, while for 0.35 vol. FeO% in PL there is the spectral convergence of the E2+PL3 mixtures with the E3+PL3 at about 1250 nm.

Fig. 8.17c shows that even the COMP band width behavior is different in the different mixtures: COMP band is wider in E4-mixture and narrower in E2-mixtures with respect to E3-mixtures.

Moreover, the spectral parameters of the three mixtures with the same PL but different mafic end-member converge to a value that represents the spectral parameters of the PL end-member absorption bands (squares in Fig. 8.17).

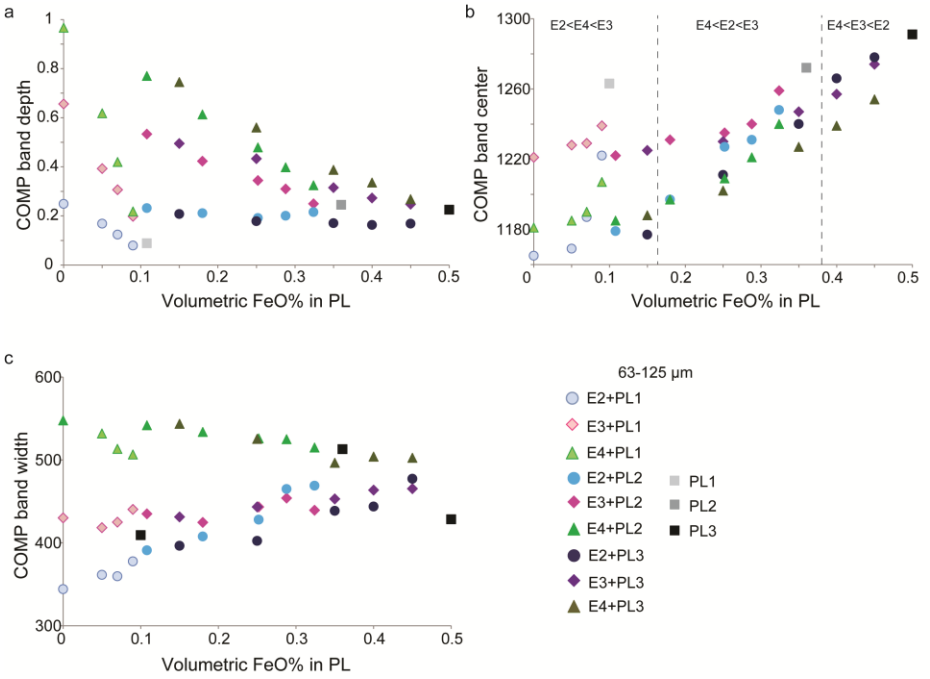

Fig. 8.17 The figure shows how the 1250 nm COMP band spectral parameters, for the 63-125 µm particle size, depend on the OL content in the mafic end-member(from Serventi et al., 2015). In particular: a) in PL1-bearing mixtures band depth decreases, with increasing rates for increasing the OL content in mafic end-member; in PL2 and PL3-bearing mixtures band depth produces negative trends for E3 and E4 and invariable trend for E2 (circles); b) for vol. FeO% <0.15, the COMP band center moves towards longer wavelengths from E2, to E3, to E4-mixtures; for 0.15< vol. FeO%<0.35, the COMP band center shows positive trends and E3-mixtures are at longer wavelengths than E2 and E4-bearing mixtures; for vol. FeO%>0.35 E2-mixtures are centered at the longest wavelengths; c) COMP band is wider in E4-mixtures and narrower in E2 mixtures with respect to E3-mixtures.All the mixture spectral parameters converge to the PL end-member parameters (squares).

Fig. 8.18 shows examples of possible ambiguity for the spectral parameters of OL-bearing mixtures, particularly the COMP band depth. Fig. 8.18 a displays the COMP band depth variation for E2 and E3-bearing mixtures; the horizontal lines show how mixtures that differ both in modal composition (different mineral modal abundance) and in particle size have very similar band depth values. In order to discriminate the different mixtures it is necessary to consider both the COMP and the mafic mineral band depths (Fig.8.18b,d).

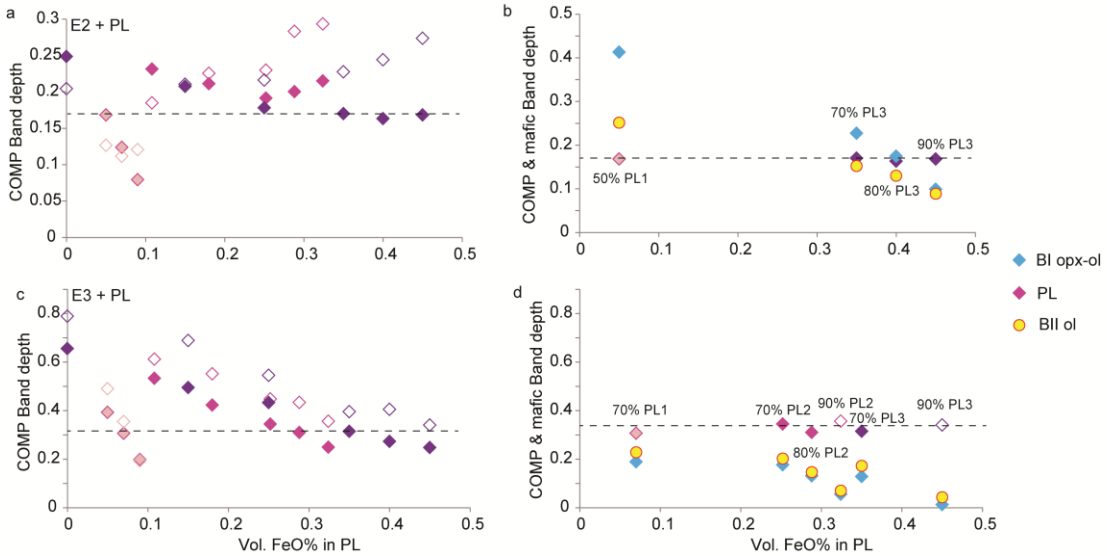

Fig. 8.18a,c) examples of ambiguity in the interpretation of spectral parameters in OL-bearing mixtures (from Serventi et al., 2015). Horizontal, dashed lines evidences mixtures with different composition and different particle size, but with analogue COMP band depth values; b,d) in the figures are plotted both COMP band and mafic band depth values. It is fundamental to consider all the absorptions to have a correct mineralogical interpretation of the spectral parameters.

Fig. 8.19 shows mixtures of the same PL as above with OL-free mafic end-members consisting of 44% CPX, 56% OPX (E1) and 100% OPX (E5). In particular, except for some outliers (e.g., 90% PL2 and PL3), E5-bearing mixtures show PL absorption bands deeper (Fig. 8.19a), wider (Fig. 8.19c) and at longer wavelengths (Fig. 8.19b) with respect to E1-bearing mixtures, probably related to the CPX absence. Fig. 8.19b shows how PL3+E5 mixture center bands display a behavior that differs from E1+PL3, moving towards shorter wavelengths.

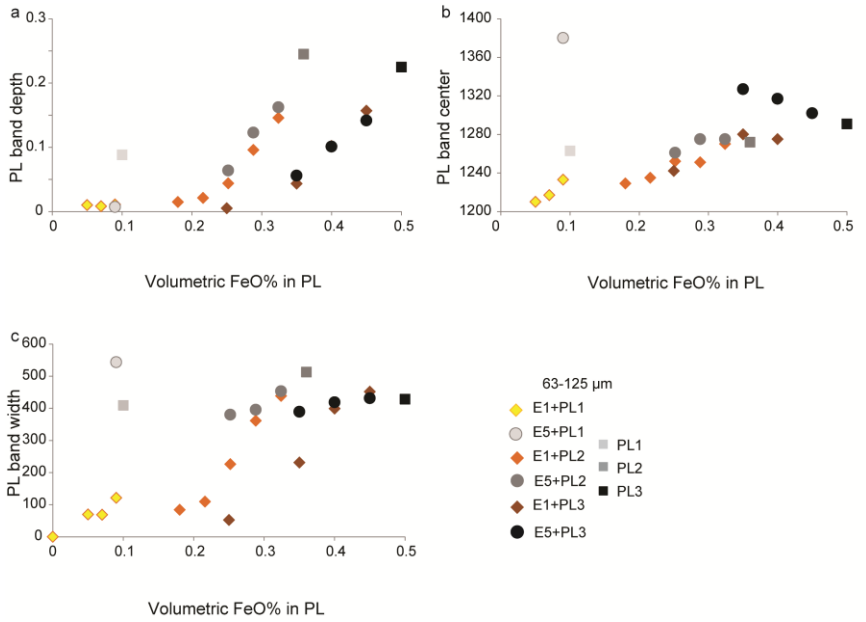

Fig. 8.19 The figure shows the different behavior of PL absorption band when mixed with OL-free, PX-bearing end-members at the 63-125 µm size (from Serventi et al., 2015). In these mixtures, differently from those shown in fig.15, the spectral parameters are more controlled by the PL chemistry than by the mafic end-member composition. In particular, E5-mixtures (diamonds) show deeper (fig. 17a), centered at longer wavelengths (fig. 17b) and wider (fig. 17c) PL band with respect to E1-mixtures (circles).

9. Spectral reflectance of plagioclase bearing mixtures: <10 μm mixtures

9.1 Particle size effects on reflectance spectra

Generally, changing the particle size affects albedo, reflectance and spectral contrast; in particular, decreasing the particle size the spectrum albedo increases while the spectral contrast, that is the strength of the absorption, is reduced due to the decrease in the mean optical path length of reflected light (Adams, 1968; Pieters, 1983). On the other hand, the band center and the band width are almost unaffected with changing the particle size (Nash and Conel, 1974), or with shifts that fall in the error of the instruments (Serventi et al., 2013).

Crown and Pieters (1987) analyzed the reflectance spectra of mixtures composed with different modal abundance of labradorite (PL) and enstatite (OPX) at different particle size. The authors showed that in the spectra of both end-members and mixtures the reflectance increases while the spectral contrast decreases. Also, they pointed out how the amount of PL detectable in mixtures with mafic minerals is particle size dependable: more PL is required in finer mixtures.

Furthermore, Craig et al. (2007) showed that increasing particle size the overall reflectance of OL, OPX and basalts decreases, while the band depth increases to reach a maximum between 45 and 250 μm to then decreases. Coarsening the particle size can produce saturation effects that complicate the determination of the absorption band center.

Serventi et al. (2013, 2015; accepted) shown how different particle size (125-250μm; 63-125μm; 36-63 μm) on PX, OL and PL spectra does not affect the band center (shifts of few nanometers fall in the instrumental error) but only the band depth, that decreases decreasing the particle size.

9.2 End-members reflectance spectroscopy and deconvolution

Fig. 9.1 shows that, generally, a fine particle size (Fig. 9.1a,b, g,h) produces spectra with higher reflectance and reduced spectral contrast compared to the coarse sizes (Fig. 9.1c-f, i-l).In particular,(1) PL (dotted lines in Fig.9.1,9.2) are characterized by a bluer slope in the NIR and almost featureless spectra; (2) E1 band I at ~900 nm becomes V-shaped (Fig. 9.1a,b) and the band asymmetry due to the presence of both OPX and CPX is emphasized; and (3) E3 shows a different behavior in the 1800-2500 nm spectral range (Fig. 9.1g,h). E3 has been separated from chromite-bearing rocks belonging to the Stillwater Complex, and, probably, some residual chromite that does not affect the spectra at coarse particle size becomes important for very fine particle sizes.

End-members at different particle sizes have been deconvolved using the same number of Gaussian, with the exception of E1, where the adjustment Gaussian G5 centered at ca. 840 nm, has not been introduced (in accordance with Sunshine and Pieters, 1993; Serventi et al., 2015).

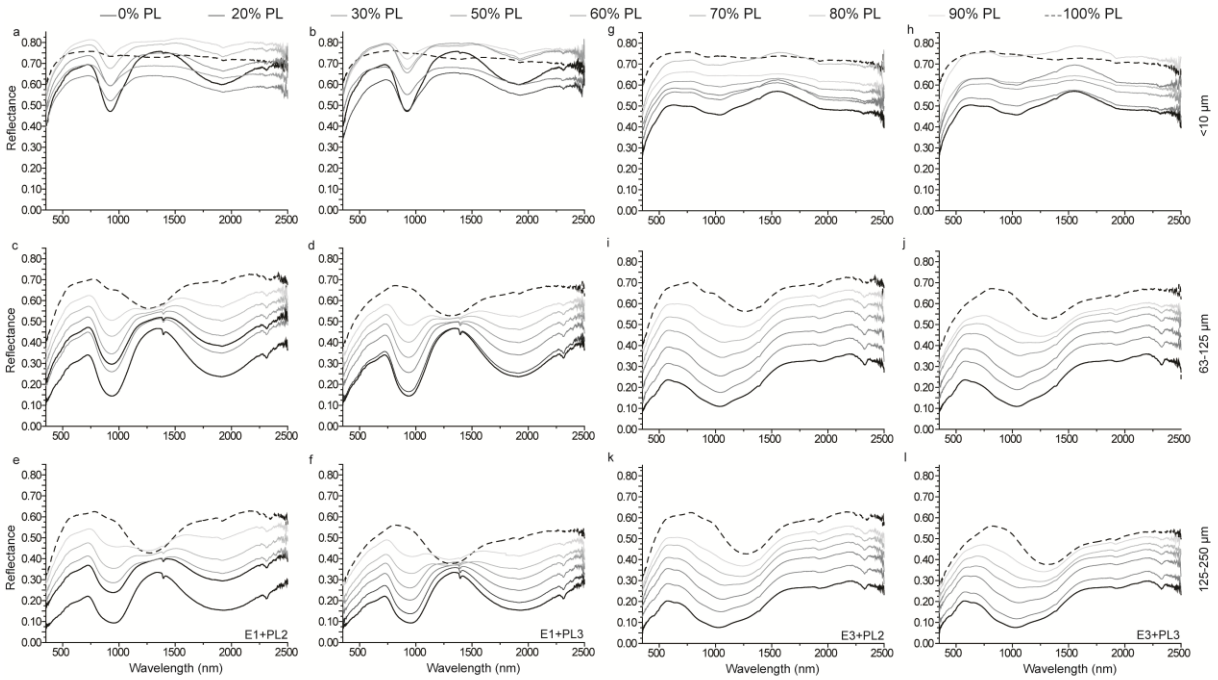

Fig. 9.1a-f) Reflectance spectra of E1+PL2 and E1+PL3 mixtures at three different particle sizes, <10 µm, 63-125 µm and 125-250 µm. a) E1+PL2 <10 µm (from bottom to top PL2: 0-50-60-70-80-90-100); b) E1+PL3 <10 µm (from bottom to top PL3: 0-20-50-70-80-90-100); c) E1+PL2 63-125 µm (from bottom to top PL2: 0-30-50-70-80-90-100); d) E1+PL3 63-125 µm (from bottom to top PL3: 0-30-50-70-80-90-100); e) E1+PL2 125-250µm (from bottom to top PL2: 0-30-50-70-80-90-100); f) E1+PL3 63-125 µm (from bottom to top PL3: 0-30-50-70-80-90-100). g-l) Reflectance spectra of E3+PL2 and E3+PL3 mixtures at three different particle sizes, <10 µm, 63-125 µm and 125-250 µm. a) E3+PL2 <10 µm (from bottom to top PL2: 0-30-50-70-80-90-100); b) E3+PL3 <10 µm (from bottom to top PL3: 0-30-50-70-80-90-100); c) E3+PL2 63-125 µm (from bottom to top PL2: 0-30-50-70-80-90-100); d) E3+PL3 63-125 µm (from bottom to top PL3: 0-30-50-70-80-90-100); e) E3+PL2 125-250µm (from bottom to top PL2: 0-30-50-70-80-90-100); f) E3+PL3 63-125 µm (from bottom to top PL3: 0-30-50-70-80-90-100).

Tab.9.1 shows, in detail, the E1 and E3 end-member spectral parameters after MGM deconvolution for the different particle sizes. In particular, reducing the particle size:

1) Both in E1 and in E3, c0 and c1 become less negative, reflecting that the albedo increases and the slope is bluer;
2) band depth of both E1 and E3 are reduced and the depth of the different absorption bands are very similar, thus revealing a reduced spectral contrast;
3) band center of both E1 and E3 do not show significant changes; and
1) band width of E1 does not show significant changes, while in E3band width, and above all the BIII width, becomes narrow.

Tab.9.1 also shows the PL end-member spectral parameters after MGM deconvolution for the different particle sizes. In particular, reducing the particle size:

1) c0 becomes less negative for both PL2 and PL3;
2) for both PL, c1 becomes more negative from 125-250 µm to 63-125 µm, but it is positive for the very fine size, revealing that very fine particle sizes act like “slab surfaces”;
3) band depth is very reduced with values close to 0;
4) PL2 band center shifts towards shorter wavelength, while PL3 center moves towards longer wavelength;
5) PL band width is narrower from 125-250 µm to 63-125 µm, but it is wider for the very fine size; and

6) The 1800 nm band is shallower, shifted towards longer wavelengths (1900-2000 nm) and narrower with respect to the 1800 band in coarse sizes.

End-member	Particle size (μm)	Band depth (Refl.)	Band position (nm)	Band width (Δnm)
E1	<10	0.240	920	200
	63-125	0.244	955	289
	125-250	0.174	976	304
E3	<10	0.078	1051	439
	63-125	0.163	1056	599
	125-250	0.155	1042	630
PL2	<10	0.018	1242	-
	63-125	0.149	1278	491
	125-250	0.199	1279	487
PL3	<10	0.018	1302	389
	63-125	0.146	1298	495
	125-250	0.179	1301	518

Tab. 9.1 Spectral parameter comparison between different particle sizes.

9.3 Mixture reflectance spectroscopy and deconvolution

Fig. 9.1 shows the reflectance spectra of mixtures at the three different particle sizes. In particular:

1) Reducing the particle size, the albedo increases and the spectral contrast is reduced;
2) While for the 63-125 and 125-250 μm sizes increasing the PL modal abundance the reflectance systematically increases, in the <10 μm size there are some outliers, such as the 50% PL2-E3 and 80% PL3-E3 mixtures, and the E1, PL2 and PL3 end-members. This behavior can be probably due to the extremely cohesiveness of the very fine particle sizes, that can resemble slab behavior;
3) PL in very fine E1-bearing mixtures produces weaker absorption bands with respect to the coarse sizes and is revealed by a flattening in the 1200 nm spectral region, while only for very high PL content (>90%) a weak absorption band can be recognizable. PL band is always shallower than PX bands;
4) In very fine E3-bearing mixtures there is not the composite band center shift in the PL region (see Serventi et al., 2013 and their Fig. 13), revealing a weaker PL absorption.

Regarding the very fine particle size, fig. 9.2, 9.3 shows that increasing the vol. FeO% in PL:

1) PL band deepens in E1 mixtures (fig. 9.2a),while it decreases in E3 mixtures (Fig. 9.3a);
2) PL band center shifts towards longer wavelength for both E1 and E3 mixtures (Fig. 9.2b, 9.3b). The shift between PL end-member and PL dominated mixtures (PL >80%) is major in E3-bearing mixtures;
3) PL band widens in E1 mixtures, while in E3-mixtures band width narrows till 0.2 vol. FeO% to then increases for higher vol. FeO% values (Fig. 9.2c, 9.3c).

Fig. 9.2, 9.3 also show a comparison for the spectral parameters after MGM deconvolution for the three different particle sizes: <10 μm (violet symbols), 63-125 μm (pink symbols) and 125-250 μm (fuchsia symbols). The principal differences regard the band depth; fig. 9.2a, 9.3a display

how PL and COMP band depths are very reduced compared to the coarse sizes and close to 0. Also the band width in the fine particle size is strongly reduced.

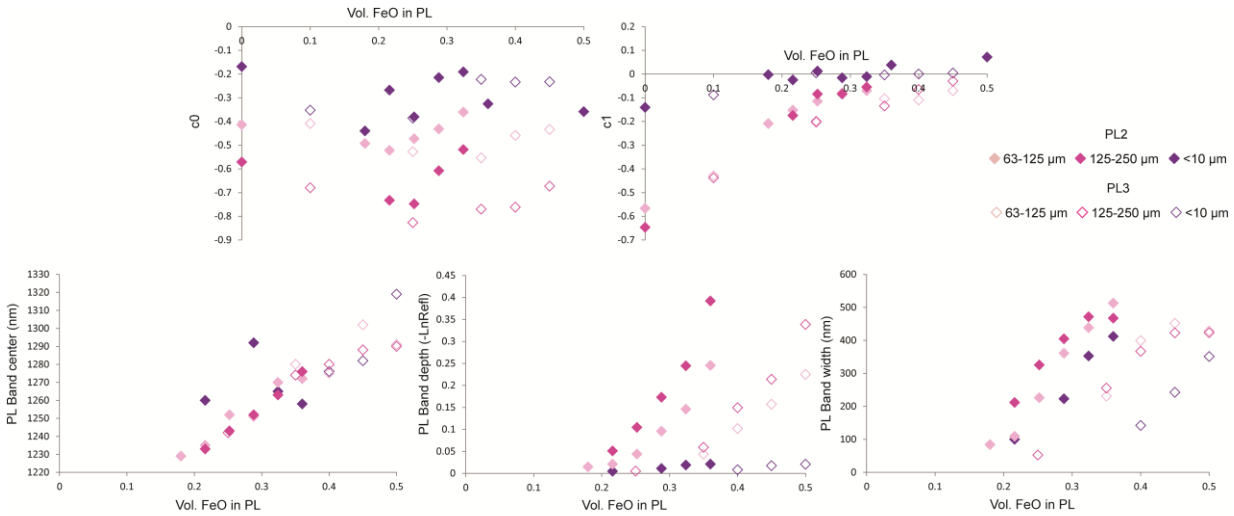

Fig. 9.2 Spectral parameter variations for the E1-bearing mixtures at three different particle sizes. Pink: 63-125 µm; fuchsia: 125-250 µm; dark violet: <10 µm; filled symbols: PL2-mixtures; empty symbols: PL3-mixtures.

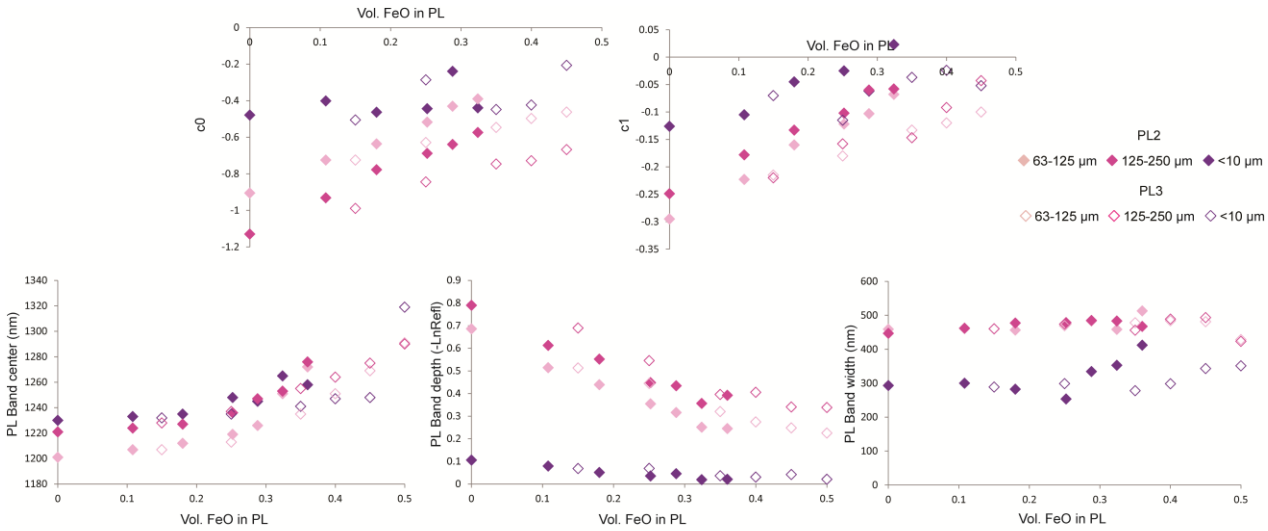

Fig. 9.3 Spectral parameter variations for the E3-bearing mixtures at three different particle sizes. Pink: 63-125 µm; fuchsia: 125-250 µm; dark violet: <10 µm; filled symbols: PL2-mixtures; empty symbols: PL3-mixtures.

10. Spectral reflectance of plagioclase-dominated mixtures: 36-63 µm mixtures

In this section we describe the results about mixtures composed with high PL content. The 36-63 µm size has been chosen as a more representative size for the lunar regolith (and probably for the hermean surface). In this chapter, our results have been plotted vs. the PL modal abundance in each mixture. Furthermore, we focus mainly on quantitatively results; qualitative analyses are reduced to a simple description of the spectroscopic variations.

10.1 Overall spectral shape variations

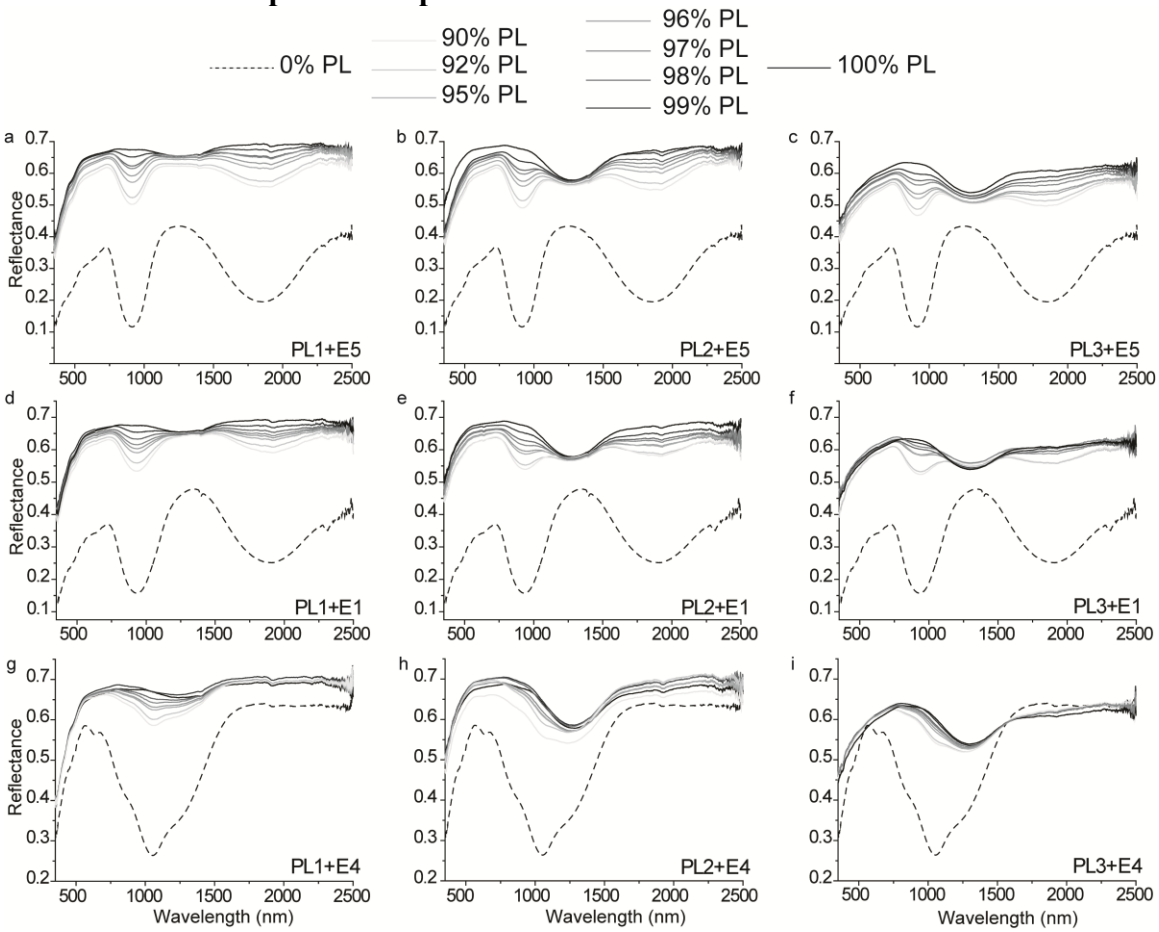

Fig. 10.1 Reflectance spectra at the 36-63 µm particle size (from Serventi et al., Accepted). a)E5+PL1; b)E5+PL2; c)E5+PL3; d)E1+PL1; e)E1+PL2; f)E1+PL3; g)E4+PL1; h)E4+PL2; i)E4+PL3. Plagioclase modal abundance increases from the bottom (dashed line spectrum) to the top (black spectrum).

Fig. 10.1 shows that, generally:

1) increasing the PL content in mixtures, spectra have reduced spectral contrast and high albedo;
2) in PX-bearing mixtures, the PX band I at ca. 900-1000 nm is detectable even in mixtures with only 1% PX (Fig. 10.1a-f), though in mixtures composed with PL3 and E1 the absorption band I is just a flattening (Fig. 10.1f);
3) in mixtures with PL1 and PX-bearing end-members, PX band I is always deeper than PL band and PX band II is deeper than PL till 98% PL (Fig. 10.1a,d);
4) in mixtures with iron-richer PL, PL2 dominates from 96% PL and PL3 from 95% PL (Fig. 10.1b,c and e,f). In E1-mixtures PL is deeper than PL in E5-mixtures;

5) in OL-mixtures, when mixed with PL1, OL is clearly recognizable till 98% PL (Fig. 10.1g), while, if mixed with PL2 and PL3 (Fig. 10.1h,i), it is masked from 97% and 96% PL, respectively; and
6) in mixtures with OL and PL2/PL3 (Fig. 10.1h,i), in the 1500-2000 nm spectral region a clear decreasing in the reflectance is visible, even if no absorption bands are expected in this PX-free spectra. This can be probably related to the iron-rich composition of PL, as shown in Hiroi et al. (2012) and in Serventi et al. (2015).

10.2 Quantitative spectral analyses: MGM deconvolution

10.2.1 End-members

Fig. 10.2 shows the deconvolution of mafic and PL end-members and Tab. 3 and 4 show the spectral parameter values.

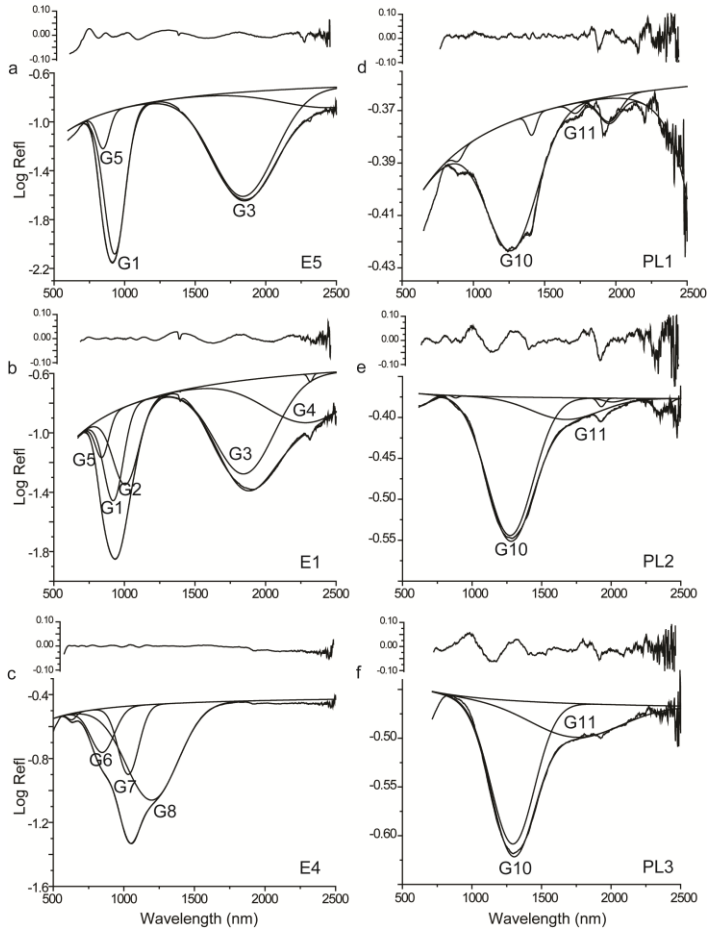

Fig. 10.2 MGM deconvolution and residuals of mafic end-members and plagioclases (from Serventi et al., Accepted).

a) E5 end-member is deconvolved with 3Gaussians, 2 in the 800-1000 nm range, G1 for Fe^{2+} in OPX and G5 for adjustment (for further explanation refer to the text), and in the NIR range G3 for Fe^{2+} in OPX; b) E1 end-member is decomposed with 5 Gaussians, 3 in the 800-1000 nm range, G1 for Fe^{2+} in OPX, G2 for Fe^{2+} in CPX and G5 for adjustment, and 2 in the NIR range, G3 for Fe^{2+} in OPX and G4 for Fe^{2+} in CPX; c) E4 end-member is decomposed with 3 Gaussians, G6, G7 and G8, due to Fe^{2+} transition in M1 and M2 sites of OL; d) PL1 is decomposed with G10 centered at ca. 1200-1250 nm for the Fe^{2+} in PL, and G11 in the 1600-1800 nm spectral region and other Gaussian for the vibrational bands due to OH alteration; e) PL2 is decomposed with G10 centered at ca. 1200-1250 nm for the Fe^{2+} in PL, G11 at ca. 1800 nm; f) PL3 is decomposed with G10 centered at ca. 1200-1250 nm for the Fe^{2+} in PL, G11 at ca. 1800 nm. Gaussians describing the vibrational bands due to OH alteration are not described in the text and in the discussions.

The residuals of the mafic end-members and PL1 are generally between ±0.05. However, considering PL2 (Fig. 3e) and PL3 (Fig. 3f), the residuals show a sinusoidal pattern in the 1000-1500 nm spectral region that could indicate the lacking of a Gaussian. We preferred to explain this behavior with a possible asymmetry or saturation effects of the PL band, also considering the reflectance decrease in the 1600-1800 nm spectral region, thus not adding further Gaussians.

For the PX-bearing end-members, a Gaussian centered at ca. 840 nm, G5, has been added. Even if the analyzed particle size is finer then those in Sunshine and Pieters (1993), and in chaper 8, the residual pattern in error after MGM deconvolution with only one Gaussian for the 900 nm band suggested us to add an additional Gaussian, called G5 and not assigned to a particular crystal field transition; for this reason, G5 is not considered in the following discussions.
In particular:

1) E5 is deconvolved with 2 Gaussians: G1 at 930 nm assigned to Fe^{2+} in M2 OPX site and G3 at 1843 nm due to Fe^{2+} transition in OPX M2 site (Fig. 10.2a);
2) E1 is deconvolved with 4 Gaussians: G1 occurring at 924 nm assigned to Fe^{2+} in OPX M2 site; G2 at 1010 nm assigned to Fe^{2+} in CPX M2 site; G3 at 1851 nm due to Fe^{2+} transition in OPX M2 site and G4 at 2317 nm due to Fe^{2+} transition in CPX M2 site (Fig. 10.2b);
3) E4 is deconvolved with 3 Gaussians, including G6 at 848 nm and G8 at 1199 nm due to Fe^{2+} transition in OL M1 site, and G7 at 1032 nm due to Fe^{2+} transition in OL M2 site (Fig. 10.2c);
4) PL1, PL2 and PL3 have been deconvolved with 2 main Gaussians, G10 centered in the 1250 nm spectral region (1271 nm, 1279 nm and 1293 nm, respectively) due to the Fe^{2+} transition in PL crystal structure, and G11 centered in the 1600-1800 nm region (1719 nm, 1675 nm and 1785 nm, respectively) to explain the reflectance decrease in the region as an asymmetry of the PL band (Fig. 10.2d-f). This band has already been recognized by Pieters et al. (1996), Hiroi et al. (2012) and Serventi et al. (2015) but has not been yet related to any particular crystal field transition;
5) the residuals in PL2 and PL3 deconvolution show a pattern in the 1000-1500 nm spectral region that could indicate the lacking of a Gaussian, but we did not add further Gaussians because no other phases are present. We preferred to explain this behavior with a possible asymmetry or saturation effects of the PL band, also considering the reflectance decrease in the 1600-1800 nm spectral region (see also Serventi et al., 2015).

Comparing with the end-member deconvolution at coarse particle size (chapter 8), absorption bands at 36-63 μm are shallower and shifted of only few nanometers with respect to absorption bands at 63-125 μm, shift that falls in the instrumental error of the instrument setup, thus revealing that a finer particle size (36-63 μm) influence the band depth but not the band center.

10.2.2 Mixtures

10.2.2.1 E5+PL

E5 is the OPX (En_{45}-Wo_{46}) endmember. Fig. 10.3 and 10.4 show that, adding PL % content:

1) c0 and c1 become less negative. c0 is less negative from PL3, to PL1, while c1 has an opposite behavior and is less negative from PL1 to PL3 (Fig. 10.3, b);
2) PL band always deepens (Fig. 10.3c), while mafic band depth decreases (Fig.10.4a). Furthermore, PL2 is slightly deeper than PL3, even if PL3 is iron richer than PL2 (Fig. 10.3c);
3) For PL1, PL2<98% and PL3< 96%, OPX band I (green symbols in Fig. 10.4a1-a3) is deeper than OPX Band II, while for PL2≥ 98% and PL3≥ 96% there is an overturn and

the OPX band II (grey symbols in Fig. 10.4a1-a3) become deeper (see squares in Fig. 10.4a1-a3). This behavior is unexpected, and can be related to the presence of PL;

4) PL center does not show significant variations (Fig. 10.3d) even if 98% and 99% PL3 are shifted towards longer wavelengths with respect to the other PL3-bearing mixtures; and
5) PL band width is almost unchanged in PL2 and PL3 mixtures, while it widens in PL1-mixtures increasing the PL abundance in mixtures (Fig. 10.3e).

Fig. 10.3c also shows that the PL depth is very different from 0.1 to 0.36 wt.% FeO PL, while it only slightly varies from 0.36 to 0.5 wt. FeO; PL1 band dominates only for more than 99% PL, while PL2 and PL3 bands are the deepest from 95% PL (Fig. 10.4a). Furthermore, the band width shows that the major difference is between PL1 and Pl2, while there is an overlap between PL2 and PL3 (Fig. 10.3e). c0, c1 and band center are the spectral parameters useful to distinguish PL2 from PL3.

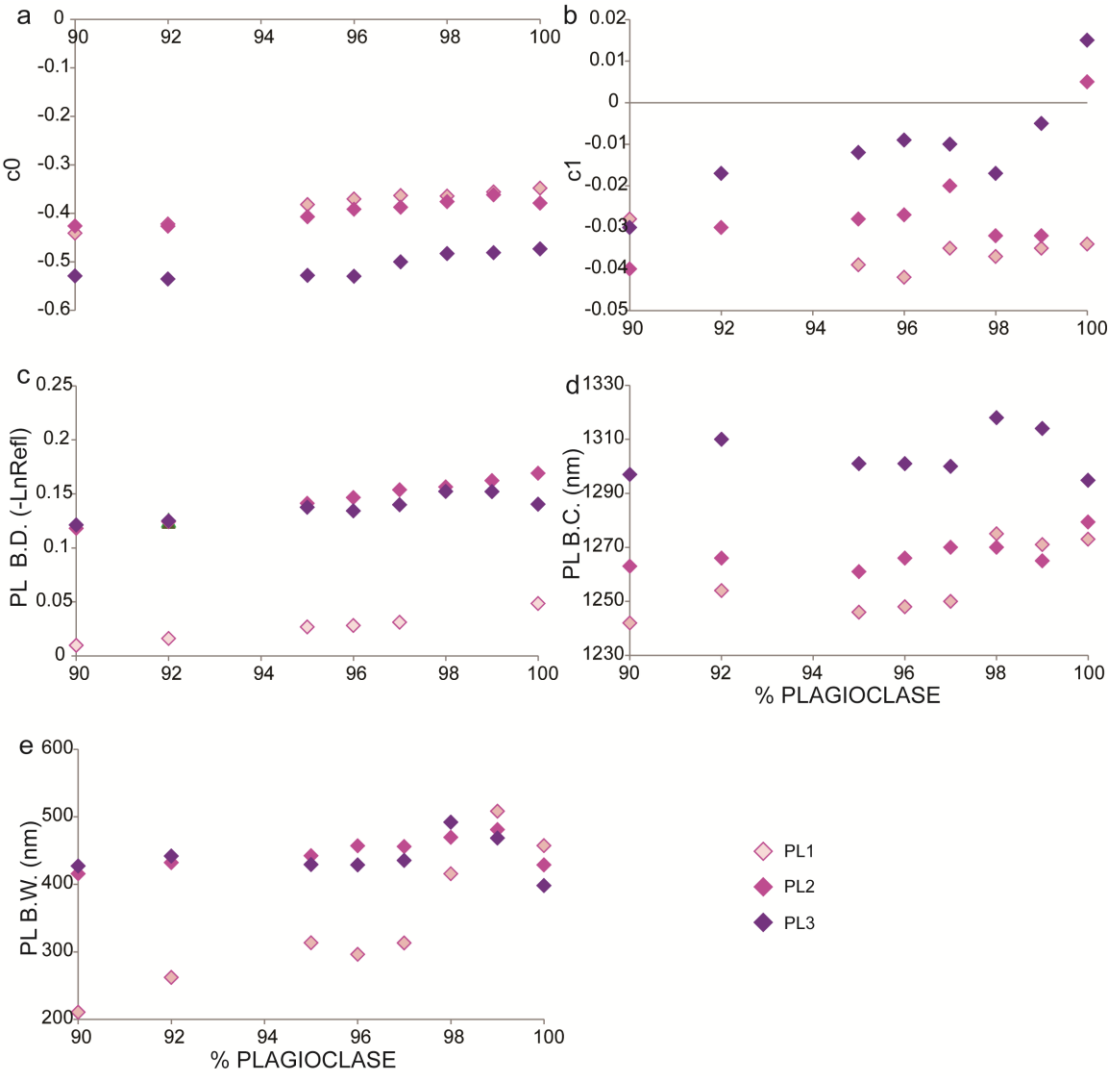

Fig. 10.3 The figure shows the spectral parameter variations in mixtures composed with E5 and PL (from Serventi et al., Accepted). In particular, with increasing PL content: a,b) c0 and, above all, c1, become less negative; c) the PL band depth deepens (with PL2 deeper than PL3); d) PL center does not show significant variations, even if 98% and 99% PL3-bearing mixture center are shifted towards longer wavelengths with respect to the other PL3-bearing mixtures; e) PL band width is almost unchanged in PL2 and PL3 mixtures while it widens in PL1-mixtures.B.C. : band center; B.D. : band depth; B.W.: band width.

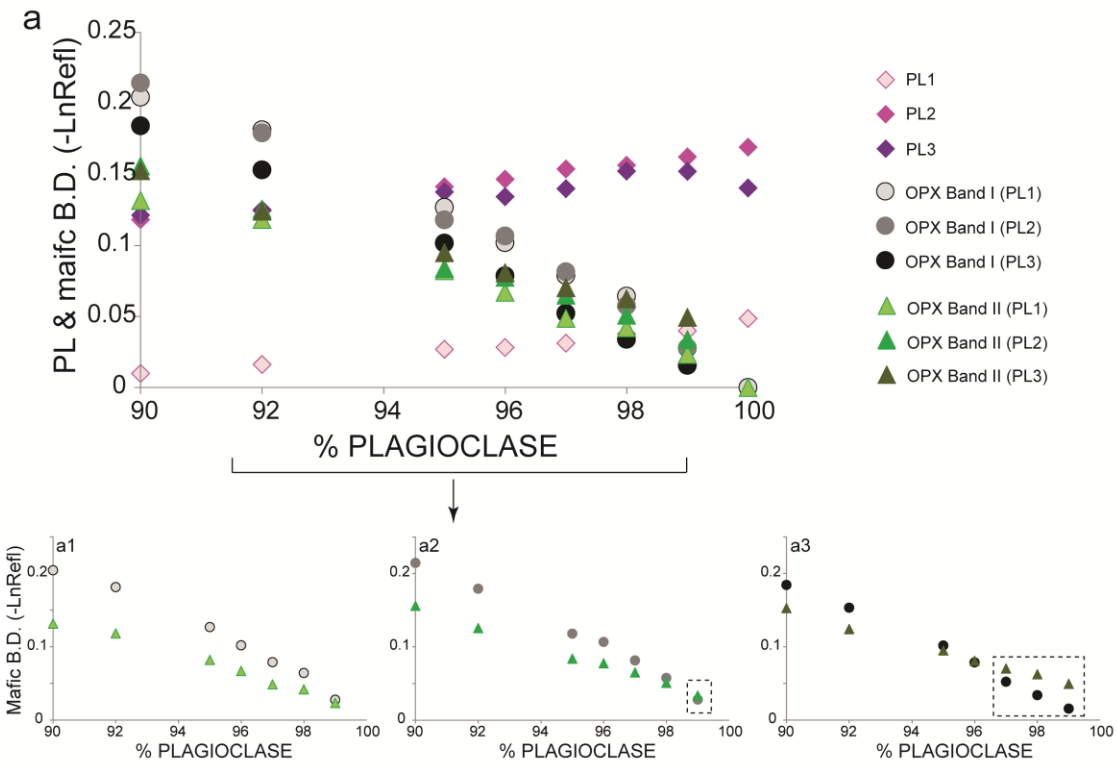

Fig. 10.4 The figure shows the band depth variation in mixtures composed with E5 and PL (from Serventi et al., Accepted). a) PL and mafic mineral depths; while PL deepens mafic band depth decrease. In particular, PL1 band dominates only for more than 99% PL, while PL2 and PL3 bands are the deepest from 95% PL. a1-a3) Enlargement of Fig. 5a: for PL1, PL2<98% and PL3< 96%, OPX band I is deeper than OPX Band II, while for PL2≥ 98% and PL3≥ 96% there is an overturn and the OPX band II become deeper (see squares).

10.2.2.2 E1+PL

E1 is a mixture of OPX and CPX; the spectral parameter variations are similar to the previous mixtures, but some consideration must be added:

1) The continuum parameters, c0 and c1, have less negative values than E5-mixtures (Fig. 10.5a,b) and, differently from previous mixtures, c1 in PL2-mixtures is less negative than in PL3-mixtures;
2) PL1 is deeper than CPX from 97% PL and deeper than OPX from 99% PL; PL2 and PL3 dominates from 92% PL (Fig. 10.6a);
3) The depth overturn between OPX band I and Band II occurs for PL2> 97% and PL3>92% (see squares in Fig. 10.6a1- a3);
4) PL band center (Fig. 10.5d) and PL width, with the exception of PL1-mixtures (Fig. 10.5e), are almost unvaried.

In these mixtures some behaviors already explained in the previous section are emphasized. In particular, Fig. 10.5c,e show very similar depth for PL2 and PL3 (PL≥ 95%) and a total overlap between PL2 and PL3 width, while Fig. 5d displays how PL1 and PL2 center are very similar. Furthermore, the OPX overturn between Band I and Band II occurs at lower PL % than in E5-mixtures (Fig. 10.6a).

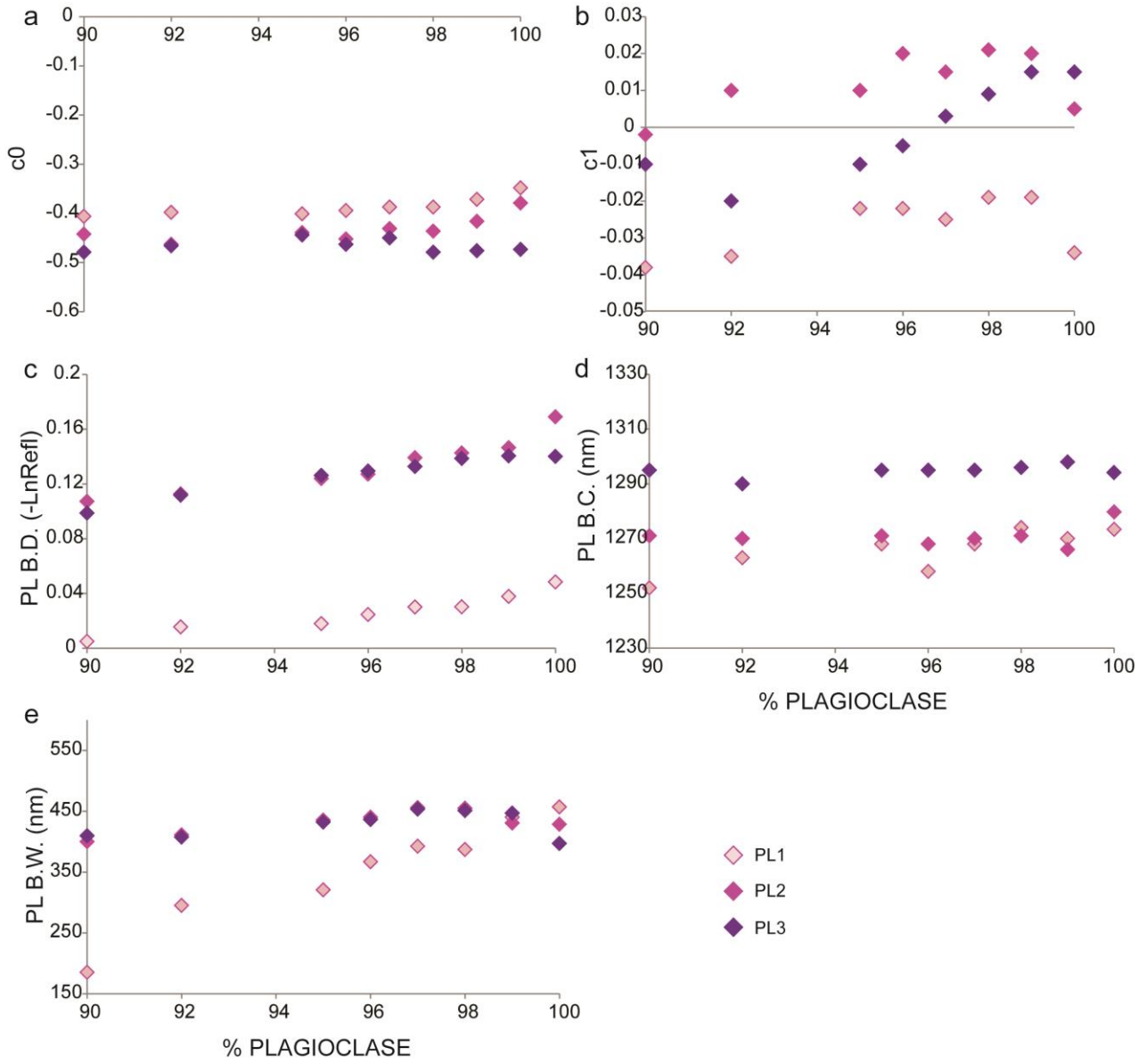

Fig. 10.5 The figure shows the spectral parameter variations in mixtures composed with E1 and PL (from Serventi et al., Accepted). In particular, with increasing PL content: a,b) c0 and, above all, c1, become less negative; c) the PL band depth deepens (with PL2 slightly deeper than PL3);d) PL center does not show significant variations; f) PL band width is almost unchanged, while in PL1-mixtures PL band widens. B.C. : band center; B.D. : band depth; B.W.: band width.

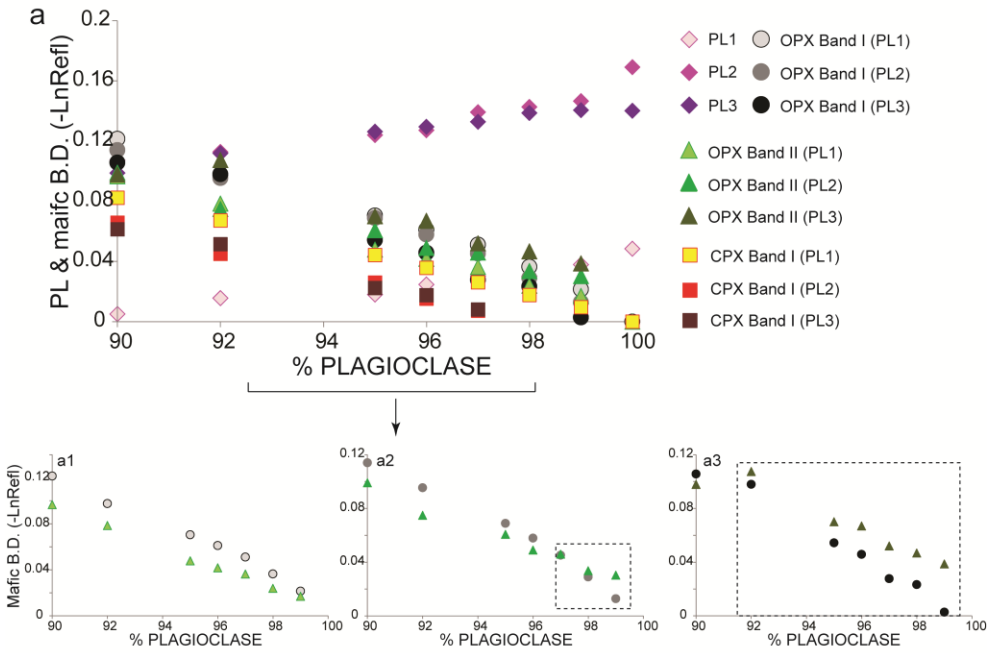

Fig. 10.6 The figure shows the band depth variation in mixtures composed with E1 and PL (from Serventi et al., Accepted). a) PL and mafic mineral depths; while PL deepens mafic band depth decrease. In particular, PL1 band dominates for more than 97% PL, while PL2 and PL3 bands are the deepest from 92% PL. a1-a3) Enlargement of Fig. 5a: for PL1, PL2<97% and PL3< 92%, OPX band I is deeper than OPX Band II, while for PL2>97% and PL3> 92% there is an overturn and the OPX band II become deeper (see squares).

10.2.2.3 E4+PL

These mixtures include the OL end-member; in spite of considering, as in previous sections, the PL absorption band, we analyze the COMP band due to the overlapping OL band 3and PL in the 1200 nm spectral region.

In particular, with increasing PL content:

1) The continuum parameter c0 is almost unaffected, while c1 becomes less negative (Fig. 10.7a,b);
2) COMP band becomes less deep but is always deeper than OL band 1 and 2 (Fig. 10.7c); a 1250 nm band deeper than the PL end-member means the presence of OL, even if not visible in the spectrum. PL2 COMP band is deeper than PL3;
3) COMP band center (Fig. 10.7d) shifts towards the longer wavelengths; and
4) COMP band width is slightly narrow (Fig. 10.7e).

Differently from the previous mixtures, 1250 nm band depth becomes less intense and band width narrower; this is related to the presence of OL that, iron richer than PL, spectroscopically dominates the COMP band. This differs from E4-mixtures analyzed in chapter 8, where we have demonstrated how, considering coarse particle sizes, the COMP band becomes less intense till a vol. FeO% value, after which the COMP band deepens.

E4 does not contain PX: for this reason no absorptions are expected in the 1800 nm spectral region. Nevertheless, spectra show a reflectance decrease in that region. In order to describe it, a Gaussian has been added with free spectral parameters, called the 1800 nm Gaussian. Fig. 10.7f,g and h, show that increasing the PL content in mixtures, the 1800 nm Gaussian deepens, as the 1250 nm band assigned to the PL absorption (see Fig. 10.3c, 10.5c), and widens. Also, depth and width increase with increasing FeO content in PL. On the contrary, the 1800 nm band moves towards shorter wavelength, with the exception of 99% PL3 and 100% PL3.

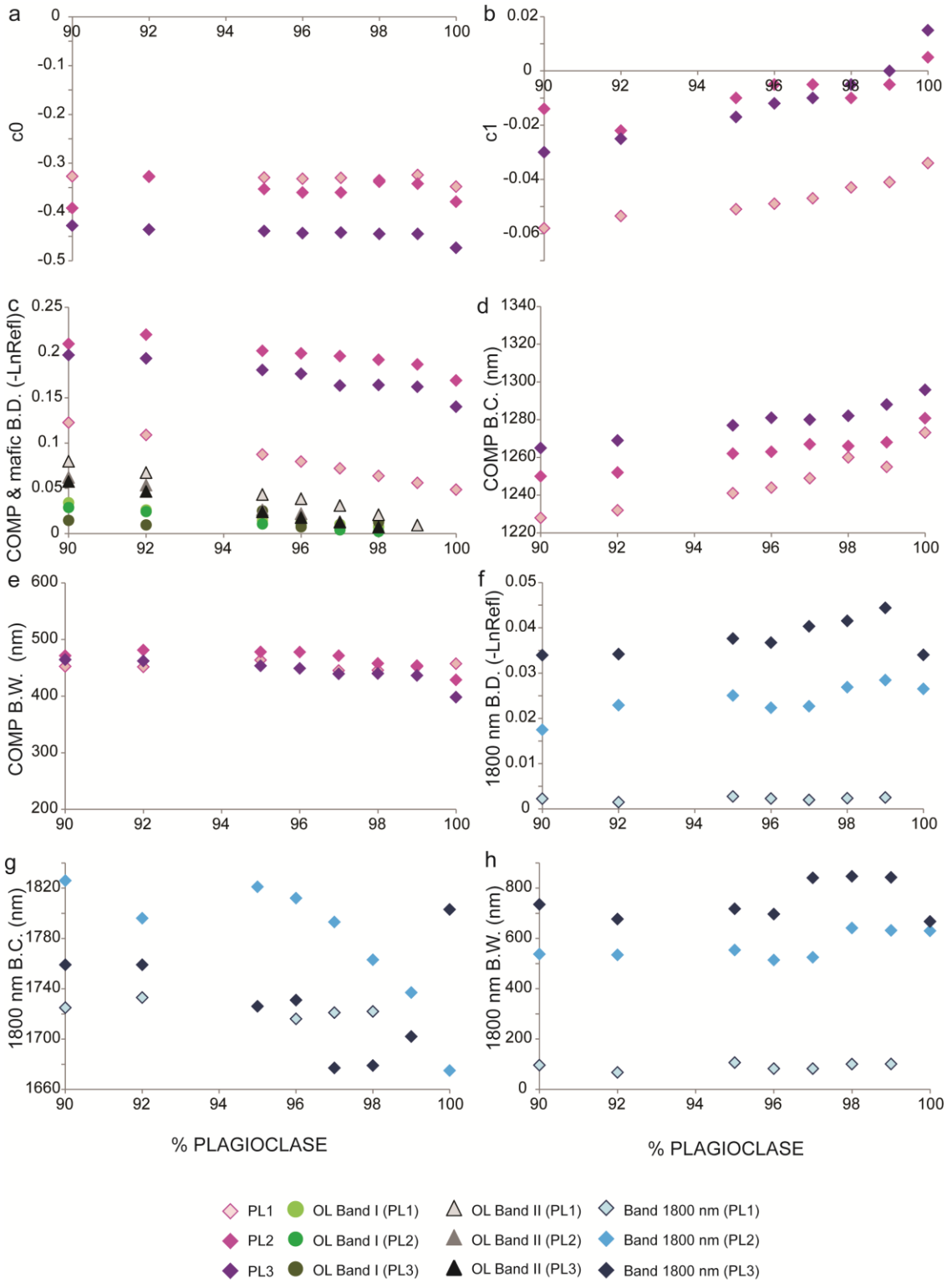

Fig. 10.7 The figure shows the spectral parameter variations in mixtures composed with E4 and PL (from Serventi et al., Accepted). In particular, with increasing PL content: a,b) c0 is almost unaffected, while c1 becomes less negative; c) COMP band becomes less deep but is always deeper than OL band 1 and 2; d) COMP band center moves towards the IR region; e) COMP band width is slightly narrow; f) 1800 nm band deepens; g) 1800 nm band moves towards shorter wavelengths; h) 1800 nm band widens. B.C. : band center; B.D. : band depth; B.W.: band width.

10.2.2.4 Comparison

Spectral parameters, extrapolated from MGM application, vary with PL% and PL chemistry. However, these variations resulted to be also related to the mafic endmember.

In fact, 1) COMP band depth decreases in OL-bearing mixtures; 2) PL band deepens when PL is mixed with PX; 3) PL band is deeper in E5 OPX-bearing mixtures with respect to OPX-CPX-bearing E1 mixtures; and 4) PL2 band is slightly deeper than PL3 band, even if iron-richer PL are expected to be deeper than iron-poor PL (Cheek et al., 2011). We interpret this behavior as probably due to an effect of saturation in FeO-rich PL3 (Fig. 10.8a), as also indicated by the presence of a strong 1800 nm band.

Regarding the band center positions, Fig. 10.8b shows that increasing PL modal abundances PL band centers generally move towards longer wavelengths for PL1-bearing mixtures, while considering PL2/PL3-mixtures band centers do not show significant variations. In PL-OL mixture, COMP band is centered at shorter wavelength (blue circles in Fig. 10.8b) with respect to the PL band center in PX-bearing mixtures, as an effect of the presence of OL; the difference is reduced from 90% PL to 99% PL. More specifically, in PX-mixtures:

1) in PL1-bearing mixtures, OPX+CPX-mixture band centers are at longer wavelengths than OPX-mixtures (light green and pink diamonds in Fig. 10.8b);
2) in PL2-bearing mixtures, OPX+CPX-mixture and OPX-mixture band centers are at similar wavelength (green and fuchsia empty diamonds in Fig. 8b); and
3) in PL3-bearing mixtures, OPX-mixture band centers are 10.at longer wavelengths than OPX+CPX-mixtures (dark green and violet diamonds in Fig. 10.8b).

Fig. 10.8c displays that increasing the PL content PL band width only slightly varies, with the exception of PL1 in E1 and E5-mixtures where PL band substantially widens.

In any cases all the spectral parameters for the PL converge to the considered PL end-member spectral parameters (grey and black diamonds in Fig. 10.8).

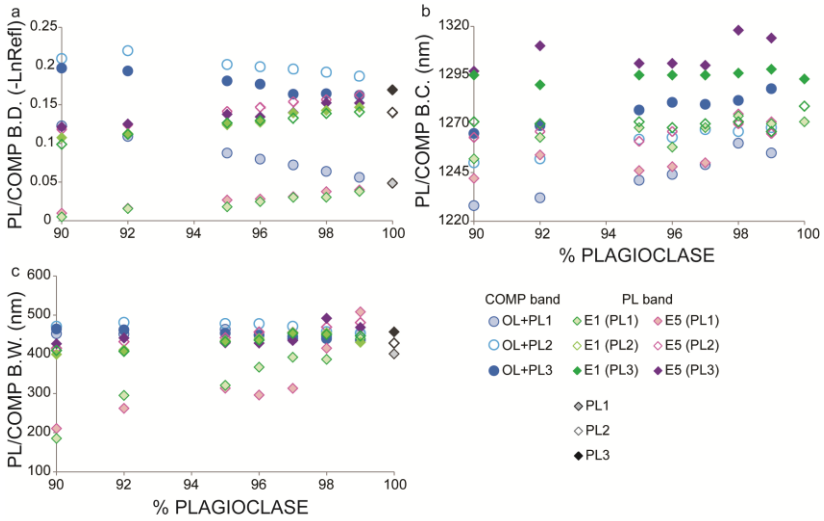

Fig. 10.8 The figure shows the comparison between all the mixtures analyzed in this paper (from Serventi et al., Accepted). a) PL band depth decreases in OL-mixtures, while it deepens in PX-mixtures; in general, PL band is deeper in E5-mixtures with respect to E1-mixtures, and PL2 band is deeper than PL3 band; b) COMP band is centered at shorter wavelength in OL-mixtures with respect to the PL band center in PX-mixtures. In PX-mixtures: 1) in PL1-bearing mixtures, OPX+CPX-mixtures are at longer wavelength than OPX-mixtures; 2) in PL2-bearing mixtures, OPX+CPX-mixtures and OPX-mixtures are at similar wavelength; and 3) in PL3-bearing mixtures, OPX-mixtures are at longer wavelength than OPX+CPX-mixtures; c) PL band width only slightly varies, with the exception of PL1 in E1 and E5-mixtures where PL band substantially widens. B.C. : band center; B.D. : band depth; B.W.: band width..

11. New contributions to plagioclase reflectance spectroscopy: concluding remarks

Thanks to the improvements in the recent missions, a more detailed interpretation of the planetary surfaces can now be delineated. However, on a planetary surface, several factors such as the mineral chemistry, the presence of different minerals that absorb in a narrow spectral range, the particle size, the space weathering etc., act in unpredictable ways on the reflectance spectra. The analysis of terrestrial analogues is fundamental to study the combined effects of these factors. A very detailed spectral library of terrestrial analogues can be found in the literature, above all for the mafic minerals. However, plagioclase has been poorly analyzed in the literature, because, due to the very low iron content in its crystal structure, has always been considered a transparent, featureless mineral.

The recent discoveries from the lunar surface and the detection of a well-defined absorption band due to Fe^{2+} transition in plagioclase crystal structure, makes it fundamental to study plagioclase in more detail.

In this thesis, we have analyzed the behavior of plagioclases with increasing iron content when mixed with mafic, iron-richer and more absorbing minerals, to understand (1) how the plagioclase absorption band changes with increasing the iron content, (2) whether plagioclase can be recognized when mixed with mafic minerals, (3) what happens when different minerals (e.g., plagioclase and olivine) absorb in the same spectral range, (4) what is the detection limit under which plagioclase cannot be detected, (5) which is the detection limit of mafic mineral, when plagioclase content is very high, and (6) which are the effects produced by different particle sizes on the plagioclase absorption band. In the previous chapters, these questions have been approached and the results obtained from our analyses have been shown. Here we report our main conclusions.

(1) Increasing the FeO wt.% in pure plagioclase, the reflectance decreases and the slope becomes bluer; at the same time, the 1250 nm absorption band deepens, widens and shifts towards longer wavelengths.

(2) The detection of plagioclase when mixed with mafic minerals is controlled in different ways by the plagioclase chemistry and modal abundance and by the kind of mafic mineral in the mixtures. Generally, plagioclase band is resolvable in mixtures with pyroxene, while when mixed with olivine, plagioclase band and the olivine band 3, absorbing in the same region, generate a composite (COMP) band.

(3) Regarding the plagioclase-pyroxene bearing mixtures, Fe^{2+} in the two phases generates absorption bands in well distinct spectral regions. In general, iron-poor plagioclase can be detected only for very high plagioclase content, while iron-richer plagioclases are recognizable even if small amounts.

Iron-poor plagioclase produces a flattening in the 1250 nm spectral region for at least 90%, while lower abundances of iron-richer plagioclase (ca. 30-50%) are needed to detect the flattening and about 70% to recognize the plagioclase band. MGM, moreover, shows that all the spectral parameters of the Gaussian describing the plagioclase absorption vary with the volumetric content due to plagioclase in the mixture. In particular, with increasing volumetric iron content, the band deepens, widens and shifts towards longer wavelengths.

Considering mixtures with plagioclase ranging between 90-99%, in iron-rich mixtures the plagioclase band is deeper than the pyroxene absorptions. MGM shows that, for these plagioclase

rich mixtures, only the plagioclase band depth varies, while band center and band width are almost unvaried.

(4) Regarding the plagioclase-olivine bearing mixtures, the composite band (COMP band, see point 2) has to be considered. Even when plagioclase band cannot be discriminated, the composite band center shifts from the typical olivine values (ca. 1050 nm) to the plagioclase values (ca. 1250 nm) in mixtures with high plagioclase content.
Although MGM is widely used as a powerful technique in order to derive quantitative information from reflectance spectroscopy, allowing the resolution of absorption bands due to chemistry and structural characteristics of single minerals, this model was not able to discriminate between the 1250 nm PL absorption band and the olivine band III in the 1200 nm region in our mixtures. In spite of this, we demonstrated that the spectral parameters of the1250 nm COMP band vary depending on plagioclase content in mixtures, but we also pointed out the FeO concentration in plagioclase affects the olivine band 3 for different olivine content in mafic assemblages.
In fact, increasing the volumetric FeO content due to the plagioclase, the COMP band depth reduces in olivine-rich mixtures, while the depth decreases and then increases in olivine-poor mixtures. Furthermore, the composite band is wider in olivine-rich mixtures than in olivine-poor ones. Regarding the composite band center, the band is at shorter wavelengths in olivine-poor mixtures for low volumetric FeO content in plagioclase, while increasing the volumetric FeO content, the composite band is at longer wavelengths than olivine-rich mixtures.

(5) Regarding mafic detection limit in plagioclase-bearing mixtures: a) the pyroxene detection limit is 1% pyroxene, and b) the olivine contribution is no more distinguishable below 5% olivine. This has important implications regarding the lunar anorthosites: FAN contains more than 90% plagioclase, while PAN regions are composed with more than 98% plagioclase. The PAN identification is therefore possible if plagioclase is mixed with pyroxene, while if olivine is present the distinction between FAN and PAN is more difficult.

(6) From the literature, it is acknowledged that pyroxene 900 nm band is deeper than 1800 nm band and that olivine does not show absorption band in the 1600-200 nm spectral region. However, analyzing plagioclase-dominated mixtures two unexpected behavior have been observed: starting from 95% iron-rich plagioclase, the pyroxene 1800 nm band becomes deeper than the 900 nm band, while the deconvolution of olivine-bearing mixtures required an additional Gaussian in order to describe a possible but not defined absorption band/asymmetry in the 1600-1800 nm spectral region, here reported as the 1800 nm band. The 1800 nm spectral parameters show a consistent variation with increasing vol. FeO% in PL. This additional band has not been interpreted in literature; nevertheless, also considering the unexpected behavior of the pyroxene bands, we preliminary suggest that the 1800 nm spectral region may be affected by high Fe^{2+} content in the PL crystal structure.

(7) We pointed out how plagioclase is size dependent; plagioclase band is deeper at the 125-250 μm size, while a very fine particle size significantly reduces the absorption band depth. Very fine plagioclase is characterized by absorption band depth close to 0, giving a new, possible significance to the featureless spectra. We also demonstrated how particle size and FeO wt.% act in the same way: both produce deeper bands, shifted towards longer wavelengths.

12. Lessons from the Earth: how to interpret the mineralogy of a planetary surface

12.1 The cases of Proclus crater and Nili Fossae

In this, and in the following chapters, we show how terrestrial analogues can help in the mineralogical interpretation of planetary surfaces. Two examples will be discussed: the PL-rich Proclus crater (Moon) and the more mafic Nili Fossae (Mars).

12.2 Data

Proclus crater have been interpreted through M^3 images, while OMEGA data have been selected for the analysis of Nili Fossae.

M^3 is a pushbroom imaging spectrometer launched on October 22, 2008, onboard India's Chandrayaan-1. It covers the 0.43-3.0 μm spectral region and acquired data in two modes, with different spectral and spatial resolution: target, with 260 spectral bands and 70 m/pixel for 25-50% of the lunar surface and global, with 85 spectral bands and 140 m/pixel for the entire surface.

In this paper we have selected the *m3g20090202t024131* image, already calibrated.

OMEGA is an imaging spectrometer working in the 0.38-1.08μm visible and near-infrared range (VNIR channel) and in the 0.92-2.69μm and 2.52-5.08μm short wavelength IR range (SWIR-C and SWIR-L channel, respectively). OMEGA has 352 spectral channels, from visible to thermal infrared and a spectral resolution of 7.5nm in the VINR, 14nm in the SWIR-C and 20nm in the SWIR-L (Bonello et al., 2005). The OMEGA spatial resolution varies between 300 m and 4 km, depending on altitude of the spacecraft. The image here analyzed has a mean spatial resolution of 3 km. Due to the goals of this work, here we analyzed spectra in the 0.5-2.5 μm spectral range.

Regarding Mars, a fundamental step is to separate the atmospheric effects from surface reflectance to obtain a correct interpretation of Mars mineralogical composition. In fact, Mars is characterized by a relative tenuous atmosphere whose spectral characteristics are contained in remote sensed data of the surface, and water, OH- and $(CO_3)^2$ in minerals absorb in the same spectral region of water and CO_2 in the atmosphere.

Among the different methods that have been developed and applied to reflectance spectra from Mars surface, the standard approach used to remove the atmospheric contribution is to divide spectra by a scaled atmospheric spectrum measured across MO (Langevin et al., 2005; McGuire et al., 2009); then the target spectrum is divided by a low spectral contrast reflectance spectrum without relevant features and with a smooth continuum.

Geminale et al. (2015) proposed a new method, called SAS, based on the principal component analysis (PCA) and target transformation (TT), that removes the noise and atmospheric components from the reflectance spectra. The authors obtained surface reflectance spectra similar to the spectra after MO method, but characterized by a reduced noise, thus permitting a better evaluation of the spectral features in particular around 1900-2300nm spectral region (see fig. 16 in their paper).

12.3 Methods

The analysis process is divided in four steps: (1) end-member selection, (2) mapping of the end-members using the Spectral Angle Mapping-SAM (Kruse et al., 1993), (3) deconvolution of the mean spectrum from each classified region via MGM, and (4) comparison with terrestrial analogues.

12.3.1 End-member selection

End-members have been selected following two different procedures, (1) manual selection in the case of Proclus crater, and (2) an iterative method, for Nili Fossae, based on the Linear Spectral Mixing Analysis (LSMA, Boardman, 1989).

LSMA is a widely used technique in remote sensing to estimate areal fractions of materials present in an image pixel, where reflectance is assumed to be a linear combination of the reflectance of each material present within the pixel. In order to produce accurate abundance results, linear spectral unmixing generally requires two constraints, which are the abundance sum-to-one constraint and the abundance non-negativity constraint. The number of selected end-members must be less than the number of spectral bands. Linear spectral unmixing also produces a root mean square (RMS) image, and the analysis of the error for each pixel gives information about the goodness or not of the end-member selection. LSMA assumes that spectra from mixed regions are a linear combination of spectrum from sub-areas compositionally homogenous.

For the end-member selection, LSMA has been first applied using two starting spectra, selected from a bright and a dark region, respectively, assuming that pixel with extreme reflectance values would be compositionally different. LSMA return one image for each end-member and a RMS image: higher RMS values in the RMS image correspond to worse classified regions. Then, we run the LSMA adding a spectrum selected from the region characterized by the highest RMS value; spectra will be added till the RMS values are minimized to values <0.0005.

12.3.2 SAM

SAM is an automated, supervised, method that determines the spectral similarity by calculating the angular distance between an unknown spectrum and end-member spectra, considering spectra as vectors in an n-dimensional space, where n is the number of bands. SAM is insensitive to illumination and albedo, but is sensitive to mineral diversity and slope variations. The SAM products are RULE images, one for each endmember, and a “threshold map”, where for each pixel is considered the best fitted endmember with a value lower the threshold. We choose as threshold an angle of 0.025 radians. Pixels with no endmember classified under the threshold are unclassified pixels. RULE images permit to evidence the variation of the angular distance for all the no-mapped endmember for each pixel or to reclassify using new thresholds for unclassified pixels or for regions not correctly classified.

12.3.3 MGM

An averaged spectrum has been calculated for each spectral unit, and deconvolved applying the MGM. The MGM is a statistic-base method based on the assumption that different absorptions can be described with a modified Gaussian distribution superimposed on to a continuum (for further details, please refer to Section 2.4 and to Sunshine et al., 1990).

12.3.4 Comparison with terrestrial analogues

Spectral parameters after MGM deconvolution have been compared with terrestrial analogues described in the previous chapters. Terrestrial and planetary spectra are characterized by a different continuum due to different environment conditions, such as space weathering, temperature etc., and, for this reason, we compare spectra after continuum removal.

13.Proclus Crater: a "fresh" view into the composition of lunar Highlands

13.1 Introduction

Proclus crater (16.1° N, 47.0° E) is a Copernican age, 28 km, simple and fresh crater, located on the northwest rim of Crisium basin and east of Palus Somni. In the past, it has been mapped and described from different Apollo missions (XI, XV, and XVII). In particular, the Apollo XV mission reported that the inner walls are almost white and exhibit debris and large blocks, the outer ring is light gray, and the floor is very irregular and rough, medium gray, with few ridges and domes (PSR, 1972). Proclus is also characterized by a ray system of ejecta that extends for a distance of over 600 kilometers all around the crater with the exception of a "ray-excluded" zone. This zone has been explained either with the low obliquity of the projectile (<15°) causing the crater or with the presence of a fault zone predating the crater (Apollo XV, PSR, 1971).Pieters (1986) and Blewett et al. (1995) shown spectra from the rim and walls of Proclus compatible with noritic anorthosites. Data from Mg/Al X-ray fluorescence for Proclus are comparable with Apollo XVI soils and anorthositic-gabbro samples (Schonfeld, 1981). Recently, pure anorthosite (PAN) regions have been recognized by Othake et al. (2009), and Donaldson Hanna et al. (2014) detected pure crystalline PL in the crater's northern wall, as well as PX and OL, both adjacent and separated from PL regions.

On the Moon, PL is the most abundant phase, and combined with mafic mineralogy (i.e. OL and PX) can solve key questions about the lunar crust formation; however, even if widespread, PL absorption was not detected for decades and it has been often associated to featureless, red-slope spectrum regions. The absence of characteristic absorptions has been explained with the low amount of iron in PL crystal structure, or with the presence of shock metamorphism (Adams et al. 1979).

Recently, Visible Near-Infrared (VNIR) observations Spectral Profiler and from M^3 have recognized a unique absorption band centered at about 1250-1300 nm, interpreted to be due to the electronic transition of low abundances of iron in the crystal structure of PL (Adams and Goulland, 1978).

13.2Data and methods

13.2.1 End-member selection

11 end-member spectra characterized by different spectral behavior have been selected both on wall and on floor of Proclus crater (Fig. 13.1a). The spectra are characterized by a red slope (i.e., the reflectance increases from the visible-VIS to the Near-Infrared-NIR spectral region), probably due to space weathering and accumulation of metallic nanophase iron. To best appreciate the different spectral characteristics, here we also show the continuum-removed end-members (Fig. 1b). Continuum has been removed using the software ORIGIN® considering the continuum line as the line that joins the reflectance maxima (Clark and Roush, 1984).

We have recognized 6 principal classes of end-members, and, for some of them, sub-classes have been defined. In particular:

1) Class A is characterized by an absorption band at ca. 1250-1300 nm. The band is asymmetric towards the NIR region in A1, and asymmetric towards the VIS region in A2. A1 also shows a reflectance decrease in the 1600-1800 nm spectral region;
2) Class B shows three absorption bands, at ca. 1000, 1250 and 1950 nm, respectively. These bands have different relative depth and the difference between 1000 and 1250 nm band depths is reduced from B5 to B2 and in B1 the 1250 nm band is deeper than 1000 nm band, thus revealing a different relative abundance of different minerals;
3) Class C displays two absorption bands at ca. 950 and 1950 nm;

4) Class D is characterized by a broad absorption at ca. 1050 nm asymmetric towards the NIR;
5) Class E is characterized by an absorption centered at ca. 1040 nm and similar to end-member D, but shallower in the 1300 nm spectral region, and by a very tenuous 2000 nm absorption; and
6) Class F is almost featureless with only a very shallow absorption at ca. 2000 nm; this unit will not be discussed in the paper, because we focus on spectra characterized by an absorption around 1000 nm region.

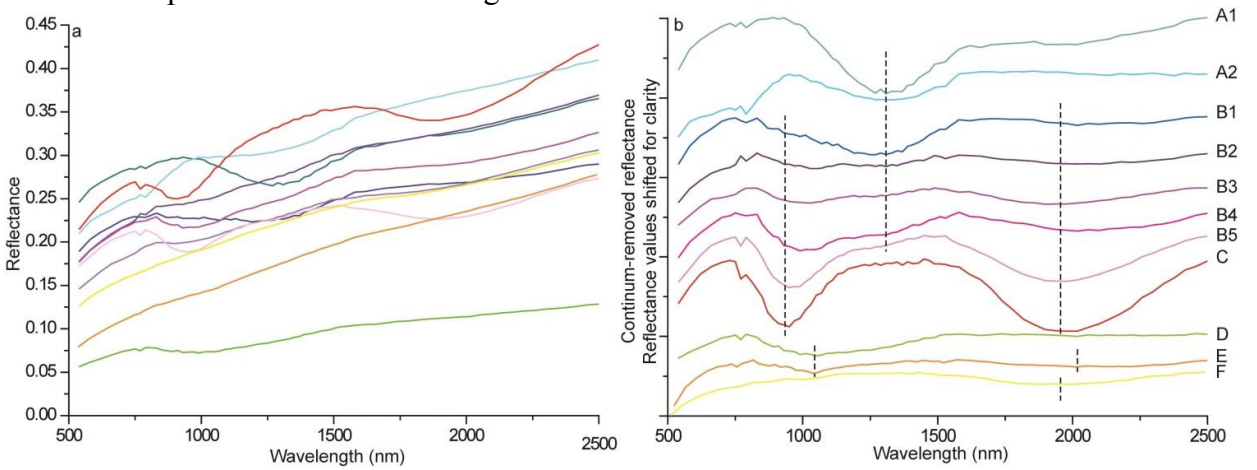

Fig. 13.1 a,b) Reflectance (left panel) and continuum-removed (right panel, following Clark and Roush, 1984) end-member spectra. A1 and A2 are characterized by an absorption bands at ca. 1250-1300 nm; B1, B2, B3, B4 and B5 show three absorption bands, around 1000, 1250 and 1950 nm; C displays two absorption bands at ca. 950 and 1950 nm; D is characterized by a broad absorption at ca. 1050 nm; E is characterized by two absorption, around 1040 nm and 2000 nm; and F is almost featureless, and not considered in this manuscript for mineralogical interpretation.

13.2.2 Spectral mapping

SAM has been efficiently used to compositionally map lithologies on different planetary bodies (e.g. Giacomini et al, 2011; Kodikara et al., 2016). Here we preliminarily considered an angle of 0.02 radians that represents the threshold between classified and unclassified data (Fig. 13.2a). Then, for each end-member, we analyzed RULE images, images that show the pixel values used to create the classified image. We evaluated classification results and reclassify each unit with ad hoc angle, in order to assigning new thresholds and improve the classification (Fig. 13.2b).

13.2.3 Mineralogical Analysis

An averaged spectrum has been calculated for each spectral unit, and deconvolved applying MGM. MGM is a statistic-base method based on the assumption that different absorptions can be described with a modified Gaussian distribution superimposed on to a continuum. A number has been assigned to each Gaussian, as described in Tab. 13.1.

Gaussian	Center (nm)	Mineralogical interpretation
G1	1250	Fe^{2+} in PL
G2	1800	Fe^{2+} in M2 site of OPX Fe^{2+} in PL
G3	2000-2300	Fe^{2+} in M2 site of CPX; Mg spinel
G4	990-1050	Fe^{2+} in M2 site of CPX Fe^{2+} in M1 and M2 site of OL
G5	900	Fe^{2+} in M2 site of OPX

Tab. 13.1 Table shows the Gaussians used for the end-member deconvolution; a number has been assigned to each Gaussian. Table also shows the mineralogical interpretation proposed for each Gaussians.

13.2.4 Terrestrial analogues

The end-members selected for the spectral mapping of Proclus crater have been compared to both mafic and PL-bearing terrestrial analogues, with compositions plausible for the lunar surface. The selected PL-bearing analogues include mixtures composed of PL (with variable composition) and different mafic mineralogy (OPX, CPX and OL), with PL content varying between 20-99%, a three different particle sizes, 36-63 μm, 63-125μm and 125-250μm. For further details, please refer to Serventi et al. (2013; 2015; accepted).Since terrestrial and lunar spectra are characterized by a different continuum due to different environment conditions (i.e. space weathering,), we compared spectra after continuum removal. Furthermore, while band center gives information about the crystal field transition in a specific mineral (Burns, 1993), band depth can be influenced not only by the chemistry but also by other factors, such as the particle size, the presence of darkening agents, the space weathering etc., in the comparison between lunar and laboratory spectra and in the mineralogical interpretation of Proclus crater we focused mainly on the band center. Regarding spectra characterized by multiple absorption bands (e.g., spectral unit B), instead of the absolute band depth, we considered the ratio between different band depths, called Band Depth Ratio (B.D.R) index.

13.3 Spectral classification of Proclus crater

13.3.1 Mineralogical mapping

Fig.13.2a shows the first SAM results highlighting the areal distributions of the different mineralogical associations present on Proclus (evidenced in Fig.13.1). Fig.13.2b shows SAM results after the application of new thresholds in order to better characterize the mapped areas. The threshold has been enlarged for the spectral units C (0.025) and D (0.033), while has been reduced for spectral units B2 (0.01), B4 (0.01) and E (0.01). From Fig. 13.2b it is clear how the classified spectral units are exposed mainly on the crater walls (with the exception of the southern west portion), while only few regions have been mapped in the crater floor. SAM classification shows that spectral unit A (green and cyan) is located in the northern wall (Fig. 13.2b), spectral unit B (blue, dark violet, light violet, fuchsia and pink) is widespread in the wall (Fig. 13.2b), spectral unit C (red) in limited areas in the wall and in the floor (Fig. 13.2b), spectral unit D (green) located in three defined and restricted regions, the bigger area is in the south-eastern wall, smaller regions (few pixels) are in the western wall and in the northern floor (Fig. 13.2b), and spectral unit E appears in the crater floor (south-east) (Fig. 13.2b). Spectral unit E is partially mapped also out from the crater.

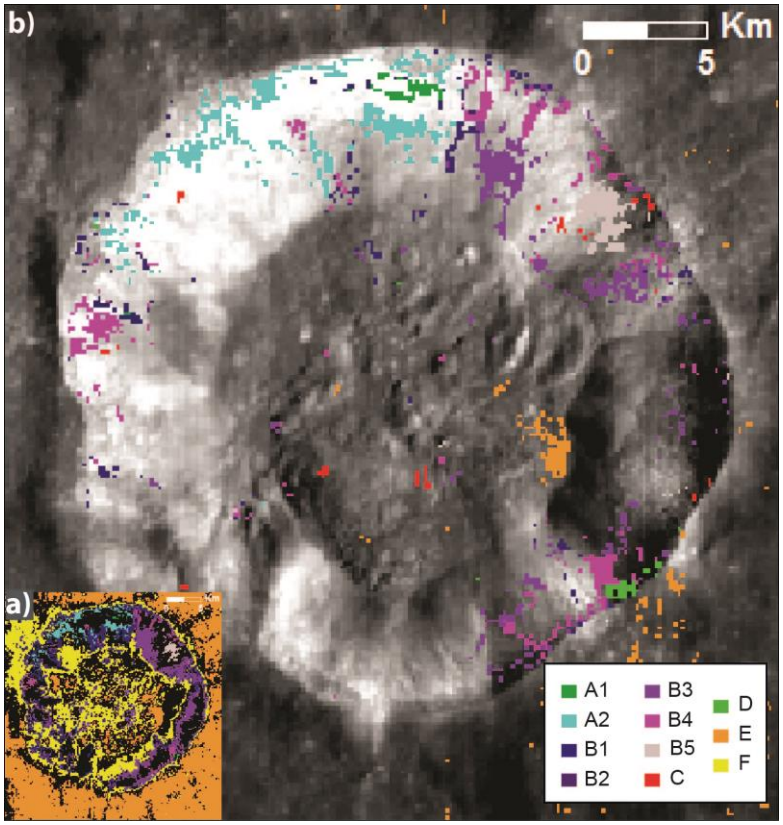

Fig. 13.2 Figure shows the SAM results. a) SAM results with threshold <0.02, in black are pixel not classified; b) SAM results for investigated units applying the new selective thresholds. Thresholds have been modified for spectral units B2 (0.01), B4 (0.01), C (0.025) and D (0.033), and E (0.01), for other units the 0.02 threshold was already suitable. Unit F (yellow in a) box) has been omitted (see text for more details).

13.3.2 Mineralogical interpretation of the units

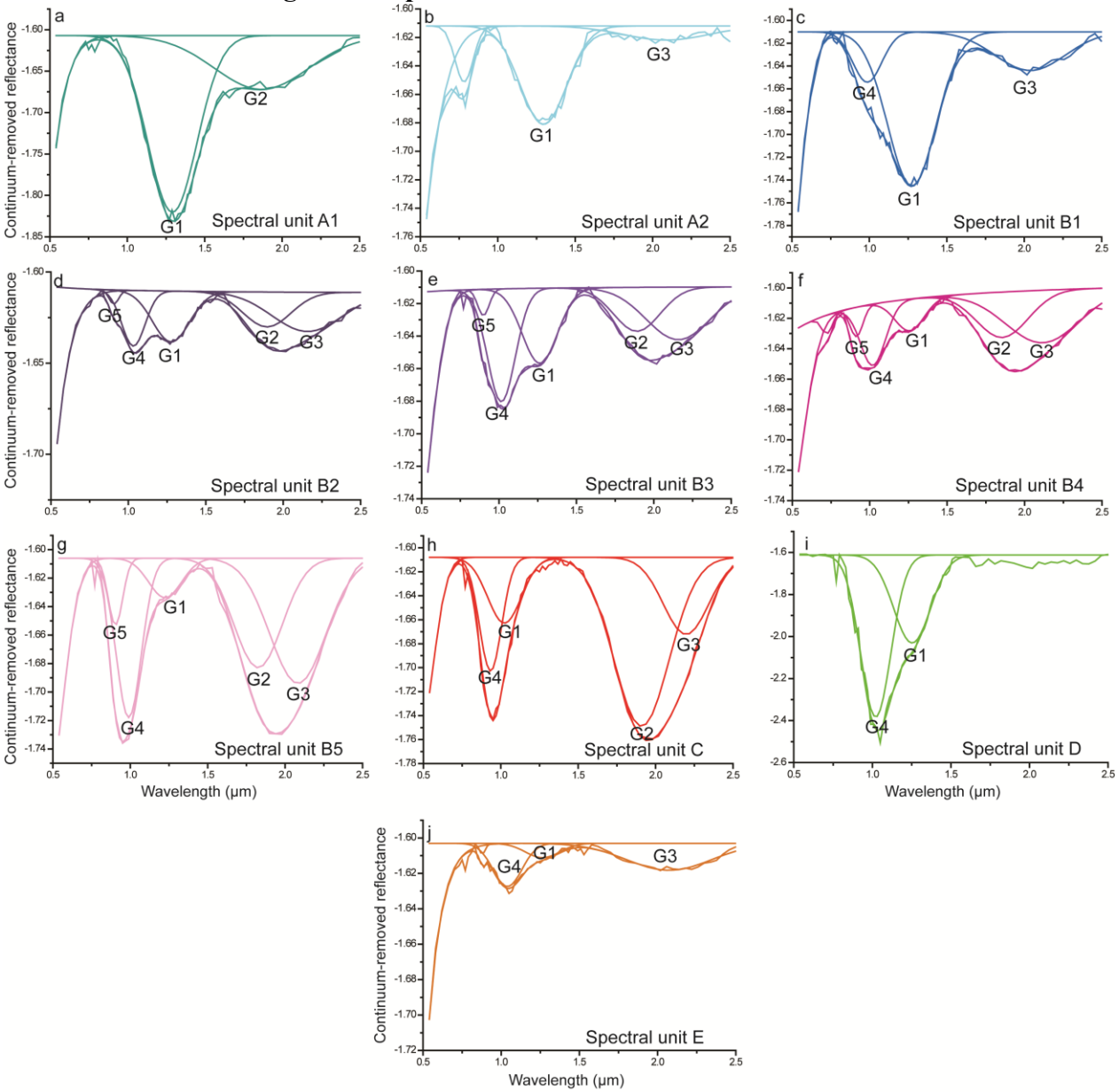

Fig. 13.3 MGM deconvolution of the mean spectrum of each classified spectral unit. In table 1 are listed the corresponding Gaussians. a,b) Unit A; G1: 1290 nm; G2: 1868 nm; G3: 2090 nm. c-g) Unit B: G4 and G3 in spectral unit B1 show positions comprised between the G4 and G5 and between the G2 and G3 positions of the other spectral units. h) Unit C: G5: 934 nm; G4: 1024 nm; G2: 1909 nm; G3: 2197 nm; i) Unit D: G4: 1021 nm; G1: 1253 nm; j) Unit E: G4: 1040nm; G1: 1265 nm; G3: 2074 (see the text for more details).

Spectral unit A

Spectral unit A has been deconvolved using two Gaussians, G1 centered at 1290 nm and G2/G3 at 1868 and 2090 nm, in spectral unit A1 and A2, respectively (Fig. 13.3a,b). G1 has been attributed to the Fe^{2+} transition in the PL crystal structure; G2 in spectral unit A1 can be compared to the 1800 nm band described by Pieters et al. (1996), Hiroi et al. (2012), and Serventi et al. (2015) and can probably be related to the iron in the PL. G3 in spectral unit A2 is shifted towards longer wavelengths with respect to G2 in spectral unit A1 and can be attributed to low amount of CPX (Klima et al., 2007) or Mg-spinel (Cheek and Pieters, 2014).

Fig. 13.4 shows how spectral unit A1 can be compared with a PL 0.5 wt.% FeO, 36-63 µm, while spectral unit A2 is very similar to a PL 0.1 wt.% FeO, 36-63 µm, even if with a slightly shallower band.

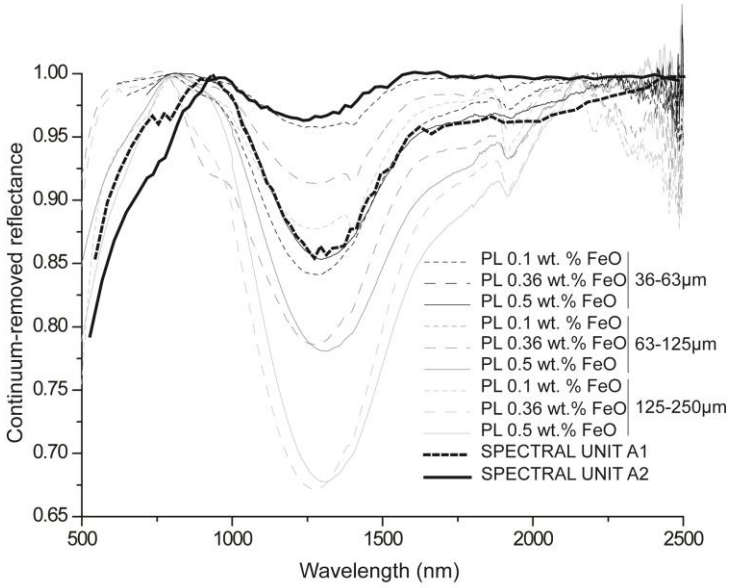

Fig. 13.4Spectral unit A1, A2 has been plotted with three PL with increasing iron content, at three different particle sizes, 36-63, 63-125 and 125-250 µm; a match can be found between A1 and PL 0.5wt.% FeO, 36-63 µm, and between A2 and PL 0.1wt.% FeO, 36-63 µm.

Spectral unit B

Spectral unit B has been decomposed using 3 to 5 Gaussians (Fig. 13.3c-g); these Gaussians allow to identify PX and PL, and their different combination permits to recognize five compositional sub-units. All the sub-units of the unit B are decomposed with G1, centered at ca. 1250 nm, which can be attributed to the Fe^{2+} transition in the PL crystal structure, as seen in unit A. Unit B1 PX absorptions are both described by one Gaussian, G4 centered at 986 nm and G3 centered at 2039 nm. Two Gaussians are needed for each absorption in the other spectral units (B2 to B5), G5 centered at ca. 900 nm and G4 between 990 and 1033 nm, and G2 centered at ca. 1850 nm and G3 at 2100 nm. The positions of G4 and G3 in B1are included between the G4 and G5 and between the G2 and G3 positions of the other spectral units. These Gaussians have been attributed to the Fe^{2+} transition in the M2 site of OPX (G5 and G2, Burns, 1993) and CPX (G4 and G3, Burns, 1993; Klima et al., 2007).

As it has been stated in the Section 2, band depth can be influenced not only by the chemistry but also by the particle size and crystal size, the presence of darkening agents, space weathering etc. For this reason, here, we do not consider the absolute depth of the Gaussians but an index (B.D.R) was proposed to evaluate the relative PX and PL percentage:

$$B.D.R = \frac{G1\ B.D.}{G1\ B.D. + G5\ B.D. + G4\ B.D.} * 100 \qquad (13.1)$$

where B.D. is the depth of each Gaussian after MGM deconvolution.

B.D.R. increases progressively from spectral unit B5 to spectral unit B1, thus revealing an increasing of PL abundance (Fig. 13.5a). Fig. 13.5c also shows the M^3 spectra (dashed lines) and relative terrestrial analogues (solid lines, from Serventi et al., 2015; accepted) with closer B.D.R, distributed from bottom to top with increasing B.D.R. In particular, spectral unit B4 shows the

900 nm (described with G4 and G5) absorption deeper than the 1250 nm absorption (fitted with G1), while in spectral unit B1the 1250 nm absorption is the deepest.
Band position is directly related to the chemistry (i.e., Fe^{2+} in crystal lattice); anyway, considering composite bands, the variation of the mineral modal abundance can induce shifts in the neighbor, weaker absorptions. So, the PL G1 center can shift with the relative PL abundance (see Serventi et al., 2013; 2015; accepted). In spectral unit B, G1 center shifts towards longer wavelengths from spectral unit B5 to spectral unit B1, in accordance with the B.D.R index.
A good correspondence can be find with B.D.R and G1 position between terrestrial analogues and M^3 spectra for the spectral units B4 to B1 (Fig. 13.5a-c).

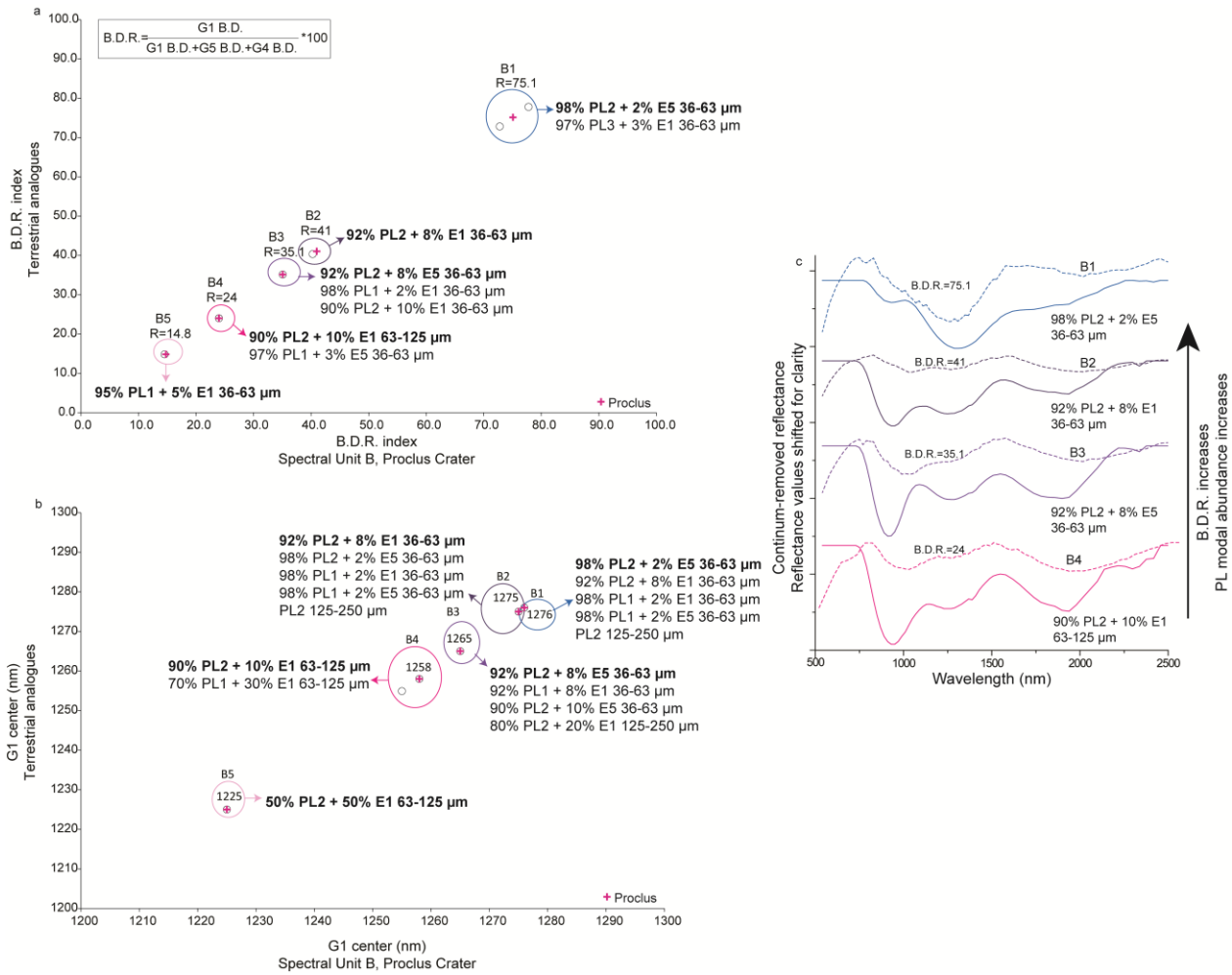

Fig. 13.5 The figure shows the comparison between spectra from Proclus crater and spectra acquired on terrestrial analogues. a) B.D.R index from Proclus crater Vs. B.D.R index from terrestrial analogues. B.D.R increases from spectral unit B5 to spectral unit B1. B.D.R. values from Proclus craters are labeled above the symbols. Good correspondence is present with some terrestrial analogues; b) G1 (1250 nm band) center from Proclus crater Vs. G1 (1250 nm band) center from terrestrial analogues. G1 moves toward longer wavelengths from spectral unit B5 to spectral unit B1. G1 values from Proclus craters are labeled above the symbols. a,b) Fuchsia cross: Proclus crater; Black, empty circles: terrestrial analogues. Compositions of terrestrial analogues with similar B.D.R values or G1 center are written on the right of the symbols. The composition reported in bold character indicate those compositions presented for both B.D.R and G1 position, which spectra are displayed in c); c) Continuum removed reflectance spectra from Proclus crater (dotted lines) are compared with the spectra of terrestrial analogues (solid lines) with composition in bold in Fig. 13.5a,b.

In particular:

1) Spectral unit B4: 90% PL with 0.36% FeO + 10% of a mixture composed of 44% CPX and 56% OPX, 63-125 μm;
2) Spectral unit B3: 92% PL with 0.36% FeO + 8% OPX, 36-63 μm;
3) Spectral unit B2: 92% PL with 0.36% FeO + 8% E1 of a mixture composed of 44% CPX and 56% OPX,36-63 μm;
4) Spectral unit B1: 98% PL with 0.36% FeO + 2% OPX, 36-63 μm.

Regarding spectral unit B5, the B.D.R. index and the G1 position are compared to two different terrestrial analogues; for this reason, we interpret G1 in B5 as due to the Fe^{2+} transition in M1 site of OPX (Klima et al., 2011).
Fig. 13.5c shows that the 900 nm band in the terrestrial analogues is shifted towards shorter wavelengths, thus implying a different PX composition (iron, and/or calcium, content).

Spectral unit C

Spectral unit C spectra are decomposed with 4 Gaussians: G5 and G4 centered at 934 and 1024 nm to describe the 900 nm band and G2 and G3 centered at 1909 and 2197 nm to describe the 1900 nm band (Fig. 13.3h). These Gaussians have been attributed to the Fe^{2+} transition in the M2 site of OPX (G5 and G2; Burns, 1993) and CPX (G4 and G3; Burns, 1993; Klima et al., 2007).
Comparing spectral unit C with PX studied in the literature (e.g., Sunshine and Pieters, 1998; Klima et al., 2007; Serventi et al., 2013; 2015), in Fig. 13.6 a good match is observed regarding the band center, although the spectral contrast (i.e. absorption band depth) is very different and reduced in lunar spectra.

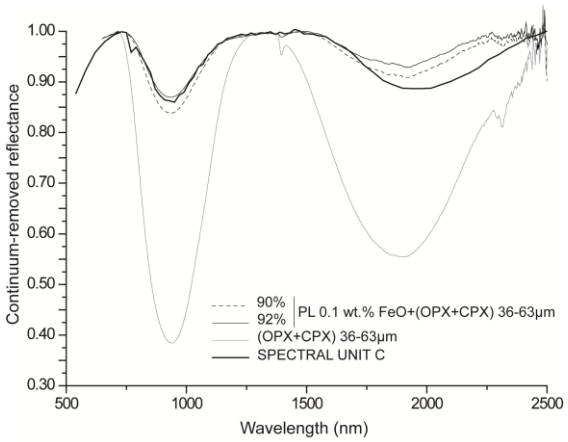

Fig. 13.6 Spectral unit C has been plotted with a mafic mixture (OPX-CPX), 36-63 μm, and with two mixtures, 90% and 92% PL 0.1wt.% FeO+(OPX-CPX). Spectral unit C shows two absorption bands centered at the same wavelengths of the mafic mixture but with a reduce depth; on the other hand, it can be compared also with the 92% mixture.

This discrepancy could be justified considering that lunar surface is affected by the space weathering, a process where formation of nanophase iron particles causes (1) the darkening of overall reflectance, (2) the spectral reddening, and (3) the weakening of absorption bands (e.g., McCord and Adams, 1973; Fisher and Pieters, 1994). Moreover, it has been demonstrated how mixing mafic minerals with even only few percentage of darkening, strong absorbing agents or with high amount of transparent material (Serventi et al., 2013; 2015; accepted; Cheek and Pieters, 2014), can significantly reduce the mafic band depth.
A very fine crystal size can also cause darkening and a reduction of the band depth. For example, powders of intrusive rocks show higher reflectance and deeper mafic band depth than powders of effusive rocks with analogue mineral chemistry and abundance (e.g. Carli et al., 2015).

In spectra from unit C, the 1250 nm band due to PL is missing (Fig.13.3h, 13.6), but reflectance is comparable to unit A. Serventi et al. (accepted) demonstrated how the spectrum acquired on a mixtures composed with 90% iron-poor PL and 10% OPX-CPX mixture (particle size: 36-63 μm) does not show the PL band at 1250 nm, but PX absorption bands with a reduced depth compared with the PX end-member (Fig. 13.6). Nevertheless, spectrum in Fig.13.6 shows a 2000 nm band deeper and shifted at higher wavelength than expected: this may imply the presence of relative low abundance of material absorbing in that spectral region, such as Mg-spinels (Cheek and Pieters, 2014).Carli et al. (2014) also showed how the presence of spinel (i.e., chromite) shifts the PX 2000 nm band towards longer wavelengths.
Thus, spectral unit C could be interpreted as a mixture of PL, PX and probably low abundance of spinel, even if we can't completely rule out the possibility of (1) a PX region affected by space weathering, (2) the presence of a strong darkening agent, or (3) the presence of material with a basaltic-like fine texture.

Spectral unit D

Spectra from unit D have been deconvolved with 2 Gaussians, G4 at 1021 nm and G1 at 1253 nm. Absorption at 2000 nm is lacking and, because the 1000 nm absorption offset is at ca. 1600 nm, G4 and G1 have not been attributed to Fe^{2+} transition in M2 CPX site and in PL, respectively; spectra of this unit behave as typical of OL. However, differently from the literature (e.g., Sunshine and Pieters, 1993; Isacsoon et al., 2010), where OL is MGM deconvolved with 3 Gaussians due to the Fe^{2+} transition in the OL M1 and M2 site (Burns, 1993), here we need only two Gaussians to model the absorption. We suppose that G4 accounts for the OL absorption band 1 (Fe^{2+} in M1 site) and band 2 (Fe^{2+} in M2 site), while G1 is the OL band 3 (Fe^{2+} in M1). OL shows a reduced spectral contrast if compared to terrestrial analogues, and a reduced spectral contrast can be explained by a series of reasons as indicated also for unit C spectra (e.g. space weathering). However, PL-rich, OL-bearing mixtures spectra can be compared with unit D spectrum (Fig. 13.7a)(e.g., 92% PL 0.1wt.% FeO and 8% OL, 36-63 μm, from Serventi et al., accepted) and G1 can be considered the expression of a composite band of PL and OL (see Serventi et al., 2013; 2015). Furthermore, Serventi et al. (accepted) demonstrated how the Gaussian fitting the OL band 1 is not needed increasing the PL content in the mixture.

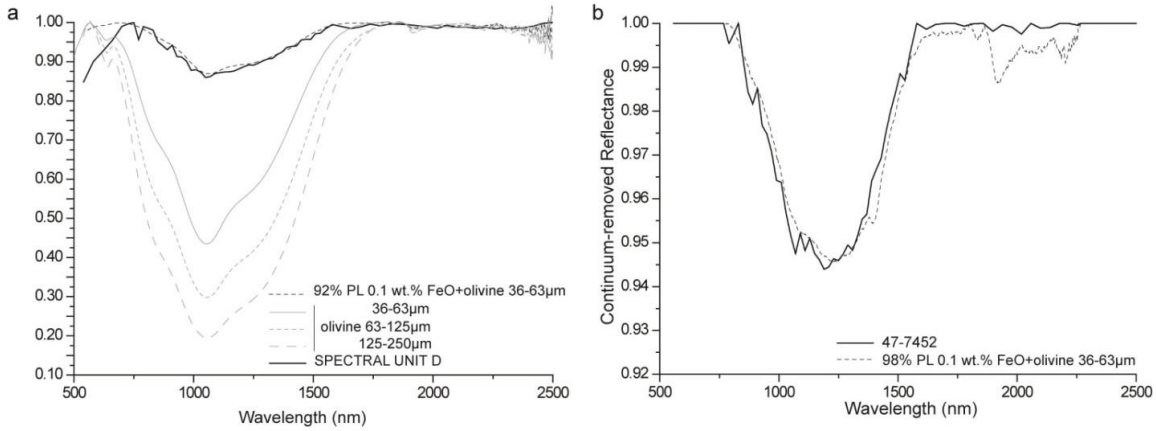

Fig.13.7 a)Spectral unit D has been plotted with OL at three different particle sizes, 36-63, 63-125 and 125-250 μm, and with a mixture, 92% PL 0.1 wt.% FeO+OL, 36-63μm . Spectral unit D shows a broad absorption band centered at the same wavelength of E4 but with a reduced depth; on the other hand, it can be compared also with the 90% mixture; b) Black, solid line: reflectance spectrum from Proclus crater; black, dotted line: reflectance spectrum of a terrestrial analogues composed with 98% PL 0.1 wt.% FeO and 2% OL.

The threshold of this spectral unit has been slightly enlarged (to 0.033 rad, see Fig. 13.2) because a manually selection of spectra around the OL regions evidenced spectra in the northern-west region that was previously mapped by the spectral unit A1, but characterized by a wider band, shifted towards shorter wavelengths. Comparing them to terrestrial analogues (Serventi et al., 2013; 2015; accepted), a good match is found with mixtures composed with 98% PL 0.1% FeO and 2% OL, at the 36-63 μm particle size (Fig. 13.7b).

Spectral unit E

Spectral unit E is deconvolved with three Gaussians, G4 at 1040 nm, G1 at 1265 nm and G3 at 2064 nm. G4 and G1 can be attributed to the Fe^{2+} transition in CPX and PL, respectively. However, if G4 is attributed to CPX, G3 should be shifted toward longer wavelengths (Klima et al., 2011). G4 and G1 can also be attributed to the OL as in the previous end-member, but in this case we will expect a band shoulder shifted towards longer wavelengths. We compared spectral unit E with the spectrum corresponding to a composition characterized by PL, OL, PX and Mg-spinel from Gross et al. (2014; please refer to their Fig. 7). A good match can be displayed for the 1000 nm absorption, while 2000 nm absorption are deeper in Gross et al. (2014); this can be explained with an higher content of spinel that affect primarily the longest wavelengths.

14. Spectral classification and mineralogical characterization of Nili Fossae

Nili Fossae is located in the northwest of Isidis Basin on Mars. Using data from TES, Hamilton et al. (2003) interpreted Nili Fossae as dominated by basalts with OL-rich materials. Hoefen et al. (2003), analyzing TES results, discovered and mapped OL in Nili Fossae and concluded that the southwestern region contains OL with composition within Fo_{60}-Fo_{70}, while in the northeast region OL varies between $<Fo_{40}$ and Fo_{60}.

Considering the OMEGA data, several authors revealed that the surface mineralogy of Nili Fossae spans between mafic silicates and hydrated minerals (Bibring et al., 2005; Gendrin et al., 2005; Mustard et al., 2005; Poulet et al., 2005). In particular, low-calcium and high calcium PX, OL and phyllosilicates have been recognized, while sulfates have not been detected.

Different mineralogical maps of Nili Fossae have also been presented for the mafic mineralogy (low-Ca PX, high-Ca PX and OL) and for hydrate minerals using spectral parameters applied to the OMEGA data (e.g., Bibring et al. 2005; Mangold et al. 2007; Mustard et al. 2007). In particular, in this region, Bibring et al. (2005) detected hydrate minerals around an old impact crater (see Fig. 6 D,E in their paper) and the largest exposure of OL on Mars. Mustard et al. (2007) showed that OL and phyllosilicates occur in spatially distinct outcrops and that, to the south and west of them, lies a unit with spectral signature dominated by the absorptions of low- and high-calcium PX, where high-calcium PX dominates. Surfaces dominated by low-calcium PX are observed in isolated regions of Nili Fossae typically associated with the rims, walls, and ejecta of impact craters. Mangold et al. (2007) noted the association of phyllosilicate rich surfaces with Noachian-aged outcrops and in the ejecta and walls of craters formed in these same-aged materials.

The mineralogical classifications described above make use of spectral parameters, a systematic method which considers few distinct wavelengths. Moreover, this method requires that the measured spectrum has to be divided by a reference spectrum of the same session in order to remove residuals due to atmospheric components (after Mons Olympus-MO (Langevin et al., 2005) method is applied) and instrumental systematic artifacts.

Here, we classify and map the mineralogy of Nili Fossae studying the OMEGA data acquired during MEX orbit number 0422_4.

14.1Spectral mapping

14.1.1 End-member selection

A total of 12 spectra, shown in Fig. 14.1, have been selected. Regions characterized by these end-members can be considered as spectral units, and we have recognized 5 principal spectral units, and for some of them sub-units have been defined. To better appreciate differences between sub-units from spectral units A, B and C, Fig. 14.1a1-c1 shows the end-members normalized at 750 nm. The normalization wavelength has been chosen out from the region where the iron crystal field absorptions in crystallographic sites of mafic minerals occur.

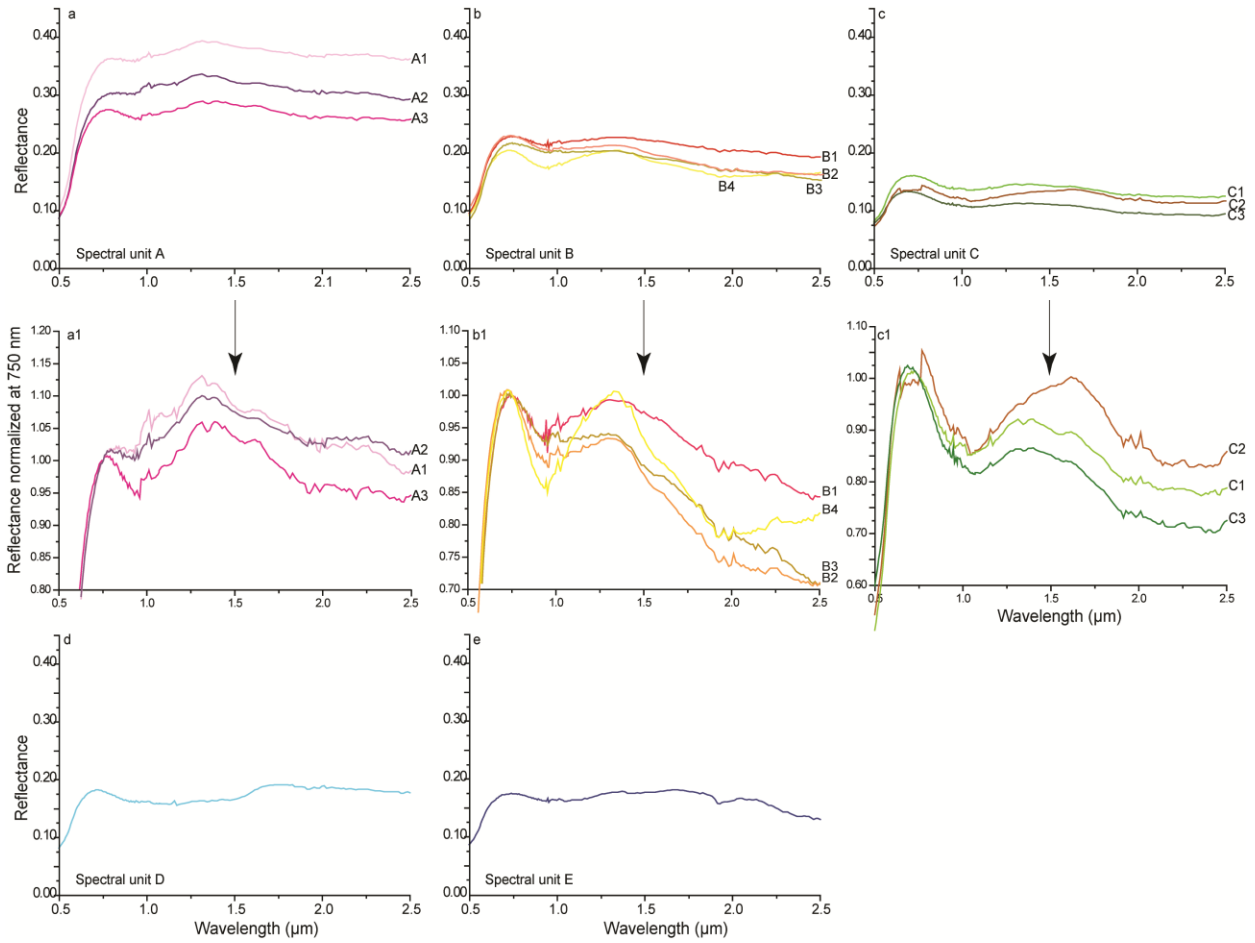

Fig. 14.1The figure shows the end-members selected for the spectral classification of Nili Fossae. a) spectra are characterized by red slope and high reflectance, where the reflectance increases from A3 to A1, and by two absorption bands at ca. 950 (BI) and 2000 nm (BII); b) spectra show sub-horizontal slope and intermediate reflectance values, and two absorption bands at ca. 950 (BI) and 2000 nm (BII). B1 shows the most reduced spectral contrast while B2 is characterized by the deepest absorptions; c) spectra characterized by low reflectance and blue slope and by two absorption bands at 1050 (BI) and 2300 nm (BII); d) spectrum, with intermediate reflectance values, shows a broad absorption band from 750 to 1650 nm (BI); e) spectrum displays an intermediate reflectance value, a weak absorption band at 1000 nm (BI) and two narrower absorptions at 1900 (BIV) and 2300 nm (BV). a1-c1) Spectra normalized at 750 nm.

In particular:

1. spectral unit A is characterized by red slope and high reflectance spectra and sub-units show decreasing albedo and a less red slope from A1 to A3. Spectra show two absorption bands, at 950 (BI) and 2000 (BII) nm related to electronic processes. BI and BII depth (the difference between the reflectance of the center and the reflectance of the continuum at the center wavelength) increases from A1 to A3;
2. spectral unit B shows intermediate reflectance spectra and reflectance decreases from B1 to B4. Spectra B1 to B4 showed two principal absorption BI and BII at ca. 950 and 2000 nm. B1 and B4 endmembers have a sub-horizontal slope and B1 has a reduced spectral contrast (or band depth) compared to B4; B2 and B3 have a blue slope and B2 has deeper absorption bands than B3;
3. spectral unit C is dominated by low reflectance spectra and reflectance decreases from C1 to C3. C1 and C3 have a blue slope and show two absorption bands BI (1000 nm) and BII (2000 nm). C2 have a sub-horizontal slope and the two absorption bands are shifted at longer

wavelength, BI at 1050 nm and BII at 2300 nm, respectively. The BI shoulder in C2 is shifted at longer wavelength with respect to C1 and C3, 1600 nm vs. 1300 nm;

4. D and E spectral units, even if with sub-horizontal spectral slope and acquired from unit B, have been classified separately. D shows a broad absorption band (BI) from ca. 750 nm to 1650 nm, while E is characterized by a weak BI (1000 nm) and narrower absorptions at 1900 nm and 2300-2500 nm, BIV and BV, respectively. BIV and BV can be associated to vibrational processes.

14.1.2 SAM classification and rule images

The end-members identified above have been used to map Nili Fossae region applying the SAM classification method, with an angle<0.025 radians; results are displayed in Fig. 14.2b. Black areas correspond to unclassified regions. The northern areas of the image are dominated by spectral unit A, while the southern regions by spectral unit C. Spectral unit B is localized geographically between spectral unit A and C, and in the impact craters. Spectral units D and E are located in more restricted areas: spectral unit D is located in the south of Nili Fossae, while spectral unit E in the center of an impact crater in the south-west part of the region.

The applied spectral classification maps only one area as composed with spectral unit E (in blue in Fig. 14.2b). Because spectral unit E is characterized by two narrow overtone absorptions and SAM considers all the reflectance spectrum, it is possible that some areas are mapped by other units dominated by electronic process even if overtone could be present but too weak. For this reason we deeply investigate the RULEs in particular for the spectral unit E to see its distribution. Fig. 14.2 shows the rule image for the spectral unit E (data range: 0-0.045; Fig. 14.2c) and the spectral unit D (data range: 0-0.069; Fig. 14.2d). Rule images recognize more areas classified with spectral unit D and E. Circles represent areas where both the spectral units can be identified.

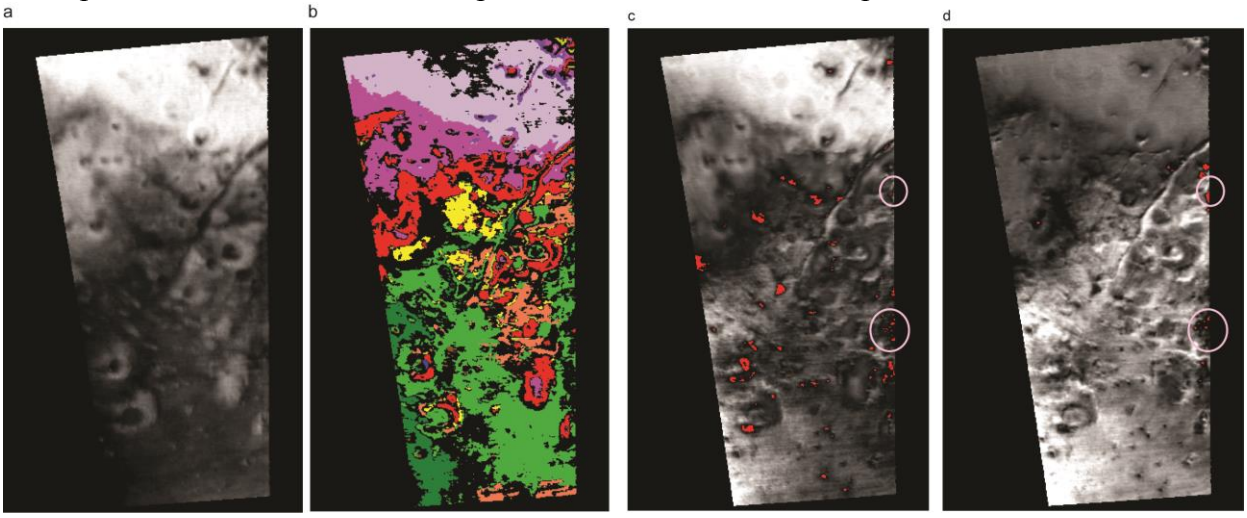

Fig. 14.2 a) Nili Fossae region as mapped by OMEGA; b) spectral classification of Nili Fossae, after SAM with the 12 end-members shown in Fig.1, 2. Black regions correspond to unclassified areas. Spectral unit A dominates the northern area, while spectral unit C the southern; spectral unit D dominates an area in the south-east of Nili Fossae, while spectral unit E (blue) appears only in the center of an impact crater in the south-west part of the image; c)RULE image for spectral unit E: the unit is more represented than after SAM classification; d) RULE image for spectral unit D. Pink circles show areas where both spectral unit D and spectral unit E can be recognized.

14.2 Spectral deconvolution

14.2.1 MGM results

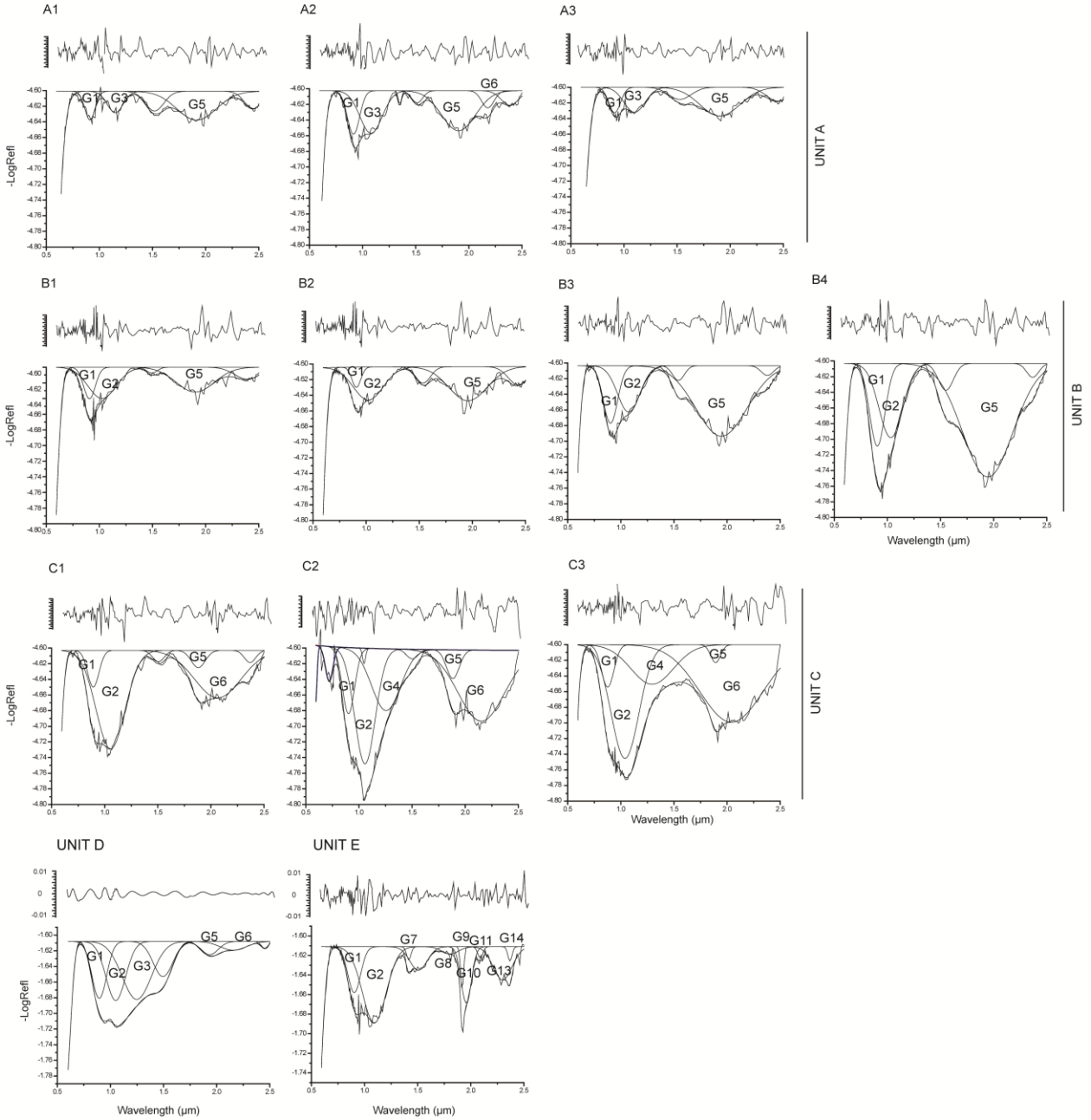

Fig. 14.3 The figure shows the MGM deconvolution of the select end-members, as well as the residuals (on the top of each deconvolution).

Fig. 14.3 shows the MGM deconvolution and the Gaussians used to fit BI and BII. The residuals are also reported on the top of each figure. A number has been assigned to each Gaussian, as explained in Tab. 14.1.

Gaussian	Position (nm)	Significance/interpretation
G1	900-950	Fe^{2+}/M2 OPX; Fe^{2+}/M1 OL; Fe^{3+} HYD; Fe^{2+} PHY
G2	1000-1050	Fe^{2+}/M2 CPX; Fe^{2+}/M2 OPX; Fe^{2+} PHY
G3	1100-1200	Fe^{2+}/M1 CPX; Fe^{2+}/M1 OPX; (Fe^{2+}/M1 OL)+ (Fe^{2+}/PL); Fe^{2+}/PL; Fe^{3+} HYD; Fe^{2+} PHY
G4	1250-1300	Fe^{2+}/M1 CPX; Fe^{2+}/PL
G5	1900-1950	Fe^{2+}/M2 OPX
G6	2000	Fe^{2+}/M2 CPX
G7	1400	H_2O overtone
G8	1800	adsorbed H_2O chl./serp.; adj.
G9	1920	H-O-H
G10	1950	H-O-H
G11	2050	adj.
G12	2200	Al-OH
G13	2300	Fe^{3+}-OH
G14	2350-2400	Fe^{2+}-OH; adj.

Tab. 14.1 Table shows the Gaussians position as well as the mineralogical interpretation.

Generally, absorption bands deepen from bright regions and red slope spectra (unit A) to dark regions and blue slope spectra (unit C).

In spectral units A and B the BI is generally deconvolved with 2 Gaussians, called G1 and G2/G3. G1 center shifts between 900 and 910 nm, G2 is located between 1020 and 1080 nm while G3 is centered in the 1100-1140 nm range.

In spectral unit C1, the BI is decomposed with two Gaussians: G1 at ca. 890 nm, and G2 centered at ca.1056 nm. Spectra from C2 and C3 have been fitted with three Gaussians: G1 at ca. 900 nm, G2 at 1050 nm, and G4 at ca. 1250 nm.

BII, in spectral units A, B and C, is generally deconvolved with more than one Gaussian. However, in the following discussion we do not consider Gaussians centered at ca. 1500 nm because it can be an instrumental artifact that depends on the flux received by the instrument.

In spectral units A1 and A3, BII is deconvolved with G5 centered at ca. 1900 nm, while A2 with G5 and G6, at 1900 and 2170 nm, respectively. BII in spectral unit B is deconvolved with a dominant Gaussian, G5, that shifts from 1900 to 1960 nm. In spectral unit C, BII is fitted with the dominant G6 (2040-2150 nm) and with G5 (1880 nm).

In unit D, BI has been fitted with three Gaussians, G1, G2 and G4, at ca. 895, 1050 and 1248 nm, while G5 and G6 at 1930 and 2150 nm fitted the BII.

Unit E spectrum is deconvolved with an higher number of Gaussians compared to the other unit spectra; BI is modeled by G1-G3 that account for electronic bands due to crystal field iron transitions, while Gaussians G7-G13, in the 1500-2500 nm spectral range, fit vibrational bands due to OH^- and to X-OH overtones.

In order to better define spectral unit E, we selected a set of spectra from hydrate regions and applied the MGM in order to recognize different hydrate mineralogies (Fig. 14.4). BIV is generally deconvolved with G8 (1720-1780 nm), G9 (1910-1930 nm), G10 (1940-1990 nm) and G11 (2040-2090 nm), while BV is fitted with Gaussians G12 (2180 nm), G13 (2290-2300 nm) and G14 (2350-2390 nm).

Fig. 14.4i shows a spectrum acquired from an area in the circle of Fig. 4; the spectrum has been deconvolved with three Gaussians in the NIR and with four Gaussians in the SWIR, with G13 slightly shifted toward longer wavelengths than G13 in E spectral unit.

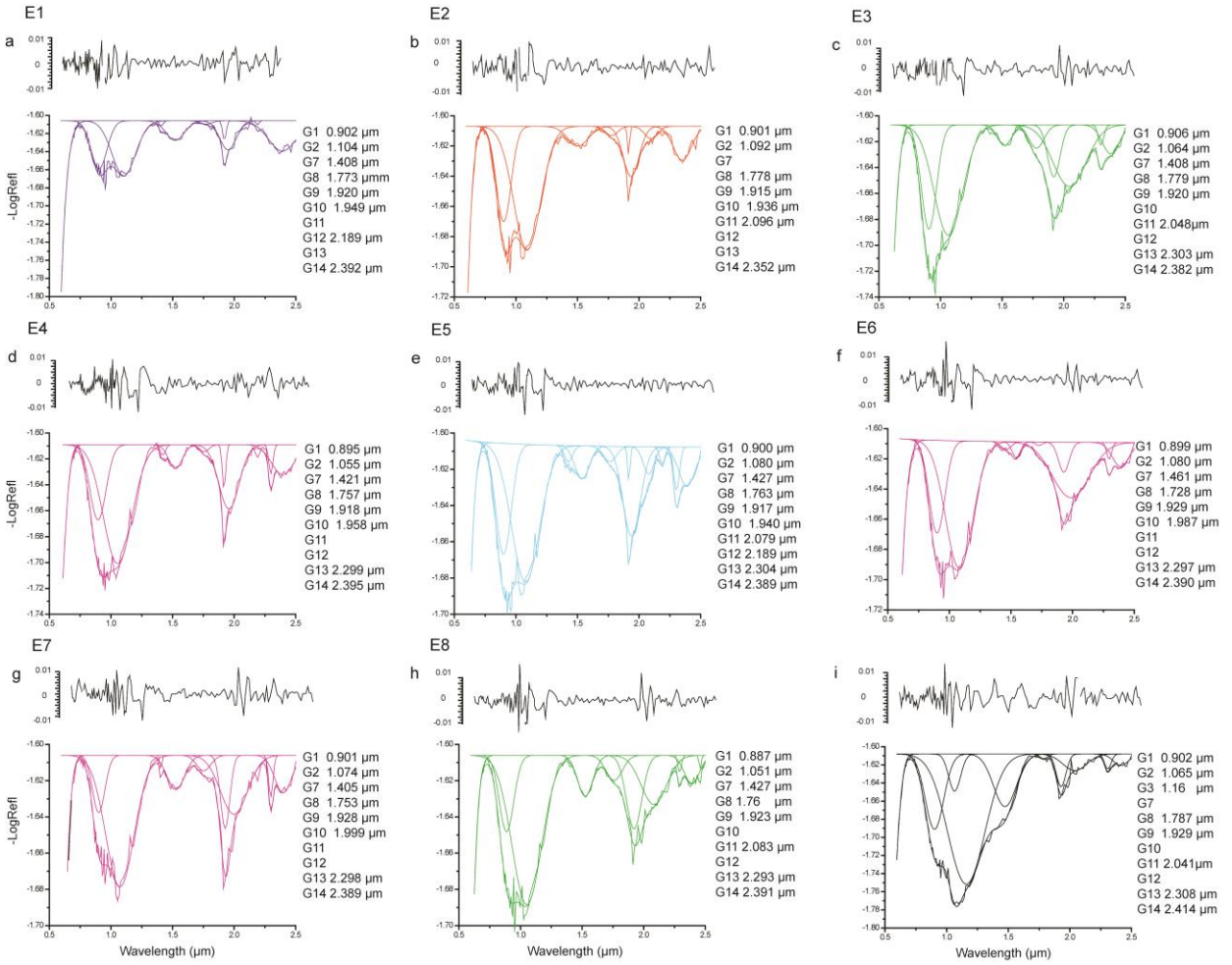

Fig. 14.4 The figure shows the MGM deconvolution of a set of spectra selected from spectral unit E, as well as the residuals (on the top of each deconvolution).

14.2.2 Gaussian interpretation

In this section we describe the spectroscopical significance of each Gaussian that fitted end-member spectra, while only in the next section we propose a mineralogical interpretation.

G1 can be attributed to (1) the Fe^{2+} transition in OPX M2 site (Burns, 1993), (2) the Fe^{2+} transition in OL M1 site (Burns, 1993), (3) the Fe^{3+} transition in iron hydroxides, such as limonite, and (4) the Fe^{2+} in iron bearing phyllosilicates, e.g., nontronite (Bishop et al., 2008b).

G2 can be attributed to: the Fe^{2+} transition in the CPX M2 site (Burns, 1993), the Fe^{2+} transition in OL M2 site (Burns, 1993), or the Fe^{2+} in iron bearing phyllosilicates, e.g., chamosite (Bishop et al., 2008b).

G3 can be attributed to: (1) the Fe^{2+} transition in the high-Ca PX, (2) the Fe^{2+} transition in OPX M1 site (Klima et al. (2007) deconvolved a set of OPX with increasing iron content and the center of the 1200 nm band varies between 1136 and 1231 nm), (3) the Fe^{2+} transition in OL M1 site when OL is mixed with PX (Serventi et al., 2013; 2015), (4) the Fe^{2+} transition in PL, when low abundances of PL are mixed with OL (Serventi et al., 2013; 2015), (5) the Fe^{3+} transition in iron hydroxides, such as limonite (see Fig. 7a), and (6) the Fe^{2+} in iron bearing phyllosilicates, e.g., chamosite (Bishop et al., 2008b).

G4 can be related to Fe^{2+} in high-Ca PX, the Fe^{2+} transition in OL M1 site (Burns, 1993), or to Fe^{2+} in iron-bearing PL.

G5 can be interpreted either as the Fe^{2+} transition in OPX M2 site, or as the Fe^{2+} transition in a mixtures of OPX and PX, while G6 as the Fe^{2+} transition in CPX M1 site.
G7 represents the H_2O overtone, while G9 and G10 the H-O-H combination of stretching and bending vibrations (Bishop et al. 2008b). G11 can be defined as an adjustment Gaussian, even if Bishop et al. (2008b) recognized bands at ca. 2000 nm due to adsorbed H_2O in chlorite and serpentine spectra. G8 has not been described in the literature and can be interpreted as an adjustment Gaussian for the BIV.
The position of G9-G11 can also be attributed to the Fe^{2+} transition in CPX and OPX M2 sites.
G12-G14 are associated to OH combination bands and the position depends on the cation in the octahedral site (Bishop et al., 2002). In particular, as reported in Bishop et al., (2008b), G12 is related to Al-OH in montmorillonite, G13 to Fe^{3+} in nontronite, while G14, if centered at 2350 nm, to Fe^{2+}-OH in chamosite. With the exception of E2, where G14 center is at 2350 nm, in the other spectra G13 is shifted at ca. 2390 nm and have been considered an additional band (Bishop et al., 2008b, see their Tab. 3).

14.3 Discussion and mineralogical interpretation of Nili Fossae

14.3.1 Spectral unit A

In spectral units A1 and A3, G1 and G5 concur to interpret BI and BII with the Fe^{2+} transition in OPX M2 site. G1 and G5 centers also reflect a composition En_{70-80}.
The assignment of G3 required an exclusion process: (1) Fe^{2+}/M2 in high-Ca PX is excluded because we will expect G4 (see Fig. 7a); (2) Fe^{2+}/M1 in OPX is excluded because G3 is deeper than the Gaussians used by Klima et al. (2007) with the same position; (3) Fe^{2+}/M1 in OL and Fe^{2+} in PL are excluded, because the BI shoulder is not at 1600 nm; and (4) Fe^{2+} in phyllosilicate is excluded since we would expect deeper vibrational bands at 1900 and 2300 nm.
The Fe^{3+} transition in iron oxides, such as limonite, seems the more reliable hypothesis, for the interpretation of G3; limonite shows an additional band at 940 nm that can be included in G1.
G6 in spectral unit A2 and a deeper G2 with respect to G3 in A1 and A3 suggest the presence of CPX. The G2 position, at longer wavelengths if compared with Klima et al. (2011), also suggests a possible mixing of CPX with hydroxides.
Therefore, spectral unit A is dominated by OPX and iron hydroxides, such as limonite, with minor amount of CPX in defined areas.

14.3.2 Spectral unit B

G1 has been interpreted with the Fe^{2+} transition in OPX M2 site and G2 with the Fe^{2+} transition in CPX, as confirmed by the presence of a G5 shifted at longer wavelength respect to G5 in spectral unit A. G1 and G2 positions suggest an OPX En_{80} and a diopside- CPX. Using the equation by Kanner et al. (2007) on the BI, we define the relative percentage of each PX. In B1, B3 and B4 OPX is ca. 55%, while in B2 is 41%.
Spectral unit B is composed of a mixture of OPX and CPX.

14.3.3 Spectral unit C

In spectral unit C, G1 has been interpreted with the Fe^{2+} transition in OPX M2 site and G2 with the Fe^{2+} transition in CPX, as confirmed by the presence of G5 and G6. G1 and G5 suggest an OPX with composition En_{80-100}. Differently from spectral unit B, G2 is deeper than G1, as well as G6 is deeper than G5, thus revealing a higher content of CPX than OPX. Applying the equation by Kanner et al. (2007), OPX is 39% in C1 while the content diminishes till 33% in C2 and C3. However, while G1 and G5 can be compared with Klima et al. (2011), G2 and G6 do not have a match. Two hypotheses can be advanced: (1) G2 is in the right position and G6 is at too short

wavelengths, or (2) G6 is in the right position and G2 is at too long wavelengths. G2 is wider than Gaussians assigned to CPX by Sunshine and Pieters (1993); for this reason, we propose the second hypothesis, suggesting that G2 can be interpreted as a composite band of CPX and other material. The interpretation of G4 in spectral units C2 and C3 has been quite misleading: while the presence of OL can be rejected (G4 center implies an extreme fayalitic OL), it is not possible to distinguish between high-Ca PX and PL. A possible choice can be driven only by the adjacent mineralogy, so making the high-Ca PX hypothesis the more reliable one.

14.3.4 Spectral unit D

G1, G2 and G4, supported by the BI shoulder at 1600 nm, can be interpreted with the presence of OL. Gaussians have a similar depth, while Sunshine and Pieters (1998) showed how G4 is deeper than G1 and G2. However, G5 and G6 suggest the presence of OPX and CPX, and this can explain the depths of G1 and G2.
Comparing the Gaussian centers with Sunshine and Pieters (1998), G1 and G3 indicate a ~Fo_{60-70} OL for a <45 μm particle size. Spectral unit D is dominated by OL with variable amounts of PX.

14.3.5 Spectral unit E

The absence of G5 and G6 and the narrow shape of the 1900 nm band suggest that G1 and G2 can be related to iron electronic transitions in phyllosilicates, and not crystal field transitions in PX. Gaussian G7-G14 positions are fundamental to characterized an hydrate mineralogy, while G12-G14 discriminate between phyllosilicates characterized by different cations in the octahedral environment; for this reason a set of sub-spectra have been selected and deconvolved, as shown in Fig. 6 and as explained in section 5.2. Considering G12-G14 centers, we recognized different groups:

1) E1: G12 is related to Al-OH modes, and G13 lacks. E1 can be interpreted as montmorillonite;
2) E2: G14 can be explained with Fe^{2+}-OH, and G12 and G13 lack. E2 can be interpreted with chamosite;
3) E3, E4, E6, E7 and E8: G13 is due to Fe^{3+}-OH, while G12 lacks. The spectra can be related to nontronite; and
4) E5: G12 is related to Al-OH modes, while G13 is due to Fe^{3+}-OH and therefore E5 can be interpreted with a mixture of nontronite and montmorillonite.

15. Lessons from the Earth: concluding remarks

In the previous chapters, we have shown how terrestrial analogues can be used to obtain important information about the mineralogy of a planetary surface. Two examples have been reported, one for a plagioclase-rich body (Moon) and one for a mafic-rich planet (Mars). We have analyzed reflectance spectra from Proclus crater and from Nili Fossae applying SAM classification and MGM deconvolution. We also compared lunar and martian data with spectral libraries consisting of well characterized terrestrial analogues (both as mineral chemistry and particle size), analyzed in this thesis as well as from the literature. It is known that different factors can act on a reflectance spectrum (e.g., space weathering, mineral mixtures, particle size); so, the comparison with terrestrial analogues does not mean that the identified units must have the exact compositions of the suggested corresponding terrestrial analogues, but that similar compositions (mineral phases and abundances) and sizes can be reasonable. This, however, without overlooking the fact that the comparison with terrestrial analogues shows how a unique interpretation is not always possible.
Here we report our preliminary conclusions.

(1) Proclus crater: Moon

All the spectral units expose mainly on the crater walls, at comparable quote, and can be considered as representative of fresh mineralogy, so strengthening the evidence that end-members can be indicative of autochthon material. Only spectral units C and E have been detected on the crater floor.
The choice of a narrow and ad hoc angle for each sub-unit of the SAM permitted us to define restricted regions with low spectral variability: these regions can be considered as exposure of a high-plagioclase association, as evidence by the comparison with terrestrial analogues. Pure anorthosite (spectral unit A) and plagioclase-rich (plagioclase>90%, spectral unit B) regions are the most abundant components, in agreement with the fact that Proclus is a small (28km) crater surrounded by the Highlands. Both the MGM deconvolution on averaged spectra and the comparison with terrestrial analogues suggest the presence of a relative Mg-rich mafic mineralogy, compatible with Highland rock chemistry, like Ferroan Anorthosites, Norites, Gabbronorites and Troctolites (e.g., Lucey et al., 2006, and references therein).
Spectral unit C and D can be interpreted as units with moderate signature of pyroxene and olivine, respectively. Thus, these spectral units can be explained as dominated by mafic absorptions, but with relative weak intensities probably due to space weathering effects, or with the presence of a different, spectrally not dominant phase. In particular, for unit C, where the reflectance is similar to unit A, we propose the second hypothesis as more reliable, even if some effects of space weathering cannot be ruled out.
Unit E seems to indicate the presence of mafic mineralogy and spinel-like phases, that could indicate a deeper lithology probably uplifted to the floor by the Proclus-forming impact. Moreover, crater floor and ejected materials (spectral unit F) are generally characterized by a 2000 nm absorption and no or weak (weaker than unit E) absorptions around 1000 nm. Even if we do not discuss these units, because they do not show plagioclase or mafic absorptions, spectra could be explained with the presence of a spinel-like phase (also present in spectral units C and E) mixed with other, probably shocked minerals in a more mature regolith.
The recognized mineralogies from Proclus crater show similar characteristics with those proposed by Pieters et al. (2011) for the Moscoviense Basin, where the OOS (orthopyroxene, olivine and spinel) exposures have been interpreted as differentiation products of plutonic events that intruded the magmatic material in the lower part of an anorthositic crust. However, Proclus is ten times smaller than Moscoviense Basin, therefore the presence of possible autochthon material

with variable compositions and at similar quote seems unlike to indicate the excavation of a shallow chamber or the rise of material from different small magma chambers; on the contrary, it is more reliable to explain Proclus mineralogies with a Magma Ocean evolution, where partially heterogeneous areas could be possible.

(2) Nili Fossae: Mars

Generally, our results for this are consistent with the spectral maps by Bibring et al. (2005), Mangold et al. (2007) and Mustard et al. (2007).

The MGM has been applied to obtain a more detailed mineralogical interpretation. In particular, we recognized: (1) spectral unit A, in the northern part of the area, dominated by orthopyroxene En_{70-80}, iron hydroxides and low amounts of clinopyroxene in defined regions; (2) spectral unit B, in the south of Nili Fossae, composed with orthopyroxene and clinopyroxene with enstatitic and diopsidic compositions; (3) spectral unit C, in the southern part of the region, dominated by an orthopyroxene with iron content slightly lower than in spectral unit A and clinopyroxene with possible contribution from high-Ca pyroxene and/or plagioclase; (4) spectral unit D, located in an area in the south-east of Nili Fossae, with olivine (Fo_{60-70}) and minor amount of orthopyroxene and clinopyroxene; and (5) spectral unit E characterized by the presence of phyllosilicates. Deconvolving a set of spectra from spectral unit E with the MGM algorithm, different typologies of phyllosilicates have been recognized: montmorillonite, nontronite and chamosite seem to be a plausible mineralogy.

As suggested for the spectral unit C, a unique interpretation is not possible: the comparison with terrestrial analogues gives evidences that both pyroxene and plagioclase can explain the spectral behavior in the 1200 nm spectral region. However, choosing one of the possible interpretations require that reflectance spectroscopy is interpreted with data from additional experiments.

16. General conclusions and implication for Mercury

In the first part of this work (chapters 7-10), we have demonstrated how plagioclase, always considered a transparent mineral, can play an important role in the reflectance spectroscopy also influencing the mafic, iron-richer mineral absorption bands. Therefore, reflectance spectra of plagioclase-bearing mixtures measured and equipped by complete analyses, can be useful to implement already well characterized spectral libraries with plagioclase-bearing mixtures.
In the second part of the work (chapters 12-14), we have shown how terrestrial analogues can be helpful for the interpretation of planetary surfaces. For example, it is possible to recognize plagioclases with different iron content, to discriminate between FAN and PAN and to identify different type of phyllosilicates. The comparison with terrestrial analogues also evidenced how the spectral convergence of materials with different compositions could lead to non-unique interpretations. For example, spectra from Proclus crater can be interpreted either as fresh, plagioclase-rich material or as more mature, mafic-rich material; in the same way, spectra from Nili Fossae can be explained with the presence of either high-Ca pyroxene or plagioclase. These results stress the need to be careful in the mineralogical interpretation of planetary material.
Our study also provides new constraints and new ideas for future analyses of the Hermean surface. On the basis of MASCS results, the hermean surface is characterized by reflectance spectra with no clear absorption bands and almost featureless shape. Mid-infrared spectra (e.g., Sprague et al., 2009) have shown the presence of plagioclase and low-FeO pyroxene and recent measurements from MESSENGER limited the iron content to be less than 6 wt.% (Solomon et al., 2008), with FeO <2-3 wt.% in silicates (Robinson et al., 2008; McClintock et al., 2008). Considering that plagioclase and pyroxene are suitable candidates for the hermean surface mineralogy, the results from this thesis could be applied to reflectance spectra from the surface of Mercury.
The BepiColombo mission (launch expected on January, 2017), with the Visible Infrared Hyperspectral Imager Channel **(**VIHI, Capaccioni et al., 2010) spectrometer onboard, will provide data about the Hermean surface composition in a larger VNIR spectral range (400-2000 nm) than MESSENGER and with high spectral resolution(256 channels with 6.25 nm spectral sampling). So, as in the lunar case, where new spectrometers with high spectral resolution were able to resolve spectra always considered featureless recognizing the plagioclase band, we will expect that data from VIHI spectrometer could give more information about the Hermean surface. We hope that the comparison of our plagioclase-bearing terrestrial analogues with reflectance spectra detected by VIHI can improve the geologic knowledge of this planet.
Brown and Elkins-Tanton (2009) proposed models for the endogenous formation of the crust of Mercury, based on the magma ocean theory, as for the lunar surface. Therefore, it will be interesting to revalue these models considering that part of the total FeO may also enter in plagioclase, and understand what implications it may have on the crust formation.

References

Adams, J.B., 1968. Lunar and Martian surfaces: petrologic significance of absorption bands in the near-infrared. Science, 159, 1453-1455

Adams, J.B., 1975. Interpretation of visible and near infrared diffuse reflectance spectra of pyroxenes and other rock-forming minerals. Infrared and Raman Spectroscopy of lunar and terrestrial minerals, Karr, C., Jr., Ed, 91-demic Press, N. Y.

Adams, J. B., Goulland, L. H., 1978. Plagioclase feldspar: visible and near infrared diffuse reflectance spectra as applied to remote sensing. PLPSC, 3, 2901-2909

Adams, J. B., Hörz, F., Gibbons, R. V., 1979. Effects of shock-loading on the reflectance spectra of plagioclase, pyroxene and glass. Lunar. Planet. Sci. 10. 1-3.

Bandfield, J.L., 2002. Global mineral distribution on Mars. JGR, 107, doi: 10.1029/2001JE001510

Bell,P .M., Mao, H .K., 1972. Crystal-field studies of lunar samples. Carnegie Inst. Yearb., 71, 480-489

Bell,P .M., Mao, H .K.,1973. Measurements of the polarized crystal field spectra of ferrous and ferric iron in seven terrestrial plagioclases. Carnegie Institution of Washington Year Book 72,574-576

Benkhoff, J., van Casteren, J., Hayakawa, H., Fujimoto, M., Laakso, H., Novara, M., Ferri, P., Middleton, H. R., Ziethe, R., 2010. BepiColombo - Comprehensive exploration of Mercury: mission overview and science goals, Planet. Space Sci., 58, 2-20.

Beran, A., Voll, D., Schneider, H., 2004.: IR spectroscopy as a tool for the characterization of ceramic precursor phases. In Beran, A. & Libowitzky, E. (eds.): Spectroscopic Methods in Mineralogy /EMU Notes in Mineralogy, 6/. Budapest: Eötvös University Press, 189–226

Bibring, J.P. et al., 2004. OMEGA: Observatoire pour la Minéralogie, l'Eau, les Glaces et l'Activité. Mars Express: The scientific payload. In: Wilson, Andrew. (Ed.), Scientific Coordination. ESA Publications Division, Noordwijk, Netherlands, pp. 37–49, ISBN 92-9092-556-6.

Bibring, J.-P. et al., 2005. Mars surface diversity as revealed by the OMEGA/Mars Express observations. Science 307 (5715), 1576–1581. http://dx.doi.org/ 10.1126/science.1108806.

Bishop, J.L. et al., 2008a. Phyllosilicate diversity and past aqueous activity revealed at MawrthVallis, Mars. Science 321 (5890), 830–833. http://dx.doi.org/10.1126/science.1159699.

Bishop, J.L. et al., 2008b. Reflectance and emission spectroscopy study of four groups of phyllosilicates: Smectites, kaolinite-serpentines, chlorites and micas. Clay Miner. 43, 35–54.

Bishop, J.L., Murad, E., Dyar, M.D., 2002. The influence of octahedral and tetrahedral cation substitution on the structure of smectites and serpentines as observed through infrared spectroscopy. Clay Miner. 37, 617–628.

Blewett, D.T., et al., 2002. Lunar pure anorthosite as a spectral analogue for Mercury. Meteoritics&Planetary Sciences 37, 1245-1254.

Blewett, D.T., et al., 2009. Mercury pyroclastics: color, morphology, and volatile content. Lunar Planet. Sci. 40, Abstract 1793.

Bokobza, L., 2002. Origin of Near-Infrared Absorption Bands, in Near-Infrared Spectroscopy: Principles, Instruments, Applications (eds H. W. Siesler, Y. Ozaki, S. Kawata and H. M. Heise), Wiley-VCH Verlag GmbH, Weinheim, Germany. doi: 10.1002/9783527612666.ch02

Boardman, J.W. 1989.Spectral and spatial unmixing: applications of singular value decomposition. Proceedings of Image Processing 1989, Reno, NV.

Bonello, G.; Bibring, J.P.; Soufflot, A.; Langevin, Y.; Gondet, B.; Berthé, M.; Carabetian, C., 2005. The ground calibration setup of OMEGA and VIRTIS experiments: description and performances. Planetary and Space Science, Volume 53, Issue 7, p.711-728. Doi: 10.1016/j.pss.2005.02.002

Brown, S.M., Elkins-Tanton, L.T., 2009. Composition of Mercury's earliest crust from magma ocean models. EPSL, 286, 446-455

Brown, A.J., et al., 2010. Hydrothermal formation of clay—carbonate alteration assemblages in the Nili Fossae region of Mars. Earth Planet. Sci. Lett., 297, 174-182

Brown, S. M., Elkins-Tanton, L. T., 2009. Composition of Mercury's earliest crust from magma ocean models. Earth Planet. Sci., 286, 446-455.

Burns, R.G., 1993. Mineralogical applications of crystal field theory. Cambridge University Press, Cambridge. 551 pp.

Bussey, D.B.J., Spudis. P.D., 2000. Compositional studies of the Orientale, Humorum, Nectaris, and Crisium lunar basins. J. Geophys. Res 105, 4235–4243.

Capaccioni, F., et al., 2010. VIS-NIR Imaging Spectroscopy of Mercury's Surface: SIMBIO-SYS/VIHI Experiment. IEEE Trans. Geoscience remote sensing, Vol. 48, No. 1 Onboard the BepiColombo Mission

Carli, C., 2009. Analisi spettroscopica nel VNIR di rocce ignee: caratterizzazionre composizionale della superficie dei pianeti terrestri. PhD thesis, University of Parma

Carli, C., Sgavetti, M., 2011. Spectral characteristics of rocks: effects of composition and texture and implications for the interpretation of planet surface composition. Icarus, 211, 1034-1048

Carter, J., Poulet, F., 2013. Ancient plutonic processes on Mars inferred from the detection of possible anorthositic terrains. Nat. Geosci. 6, 1-4

Cheek, L. C., et al., 2011. Spectral characteristics of plagioclase with variable iron content: application to the remote sensing of the lunar crust. Lunar. Planet. Sci. 42. Abstract 1617

Cheek, L. C., Donaldson Hanna, K.L., Pieters, C.M., Head, J.W., Whitten, J.L., 2012. The distribution and mineralogy of anorthosite in the Orientale Basin: new perspective from M^3 data. Second conference on the lunar highland crust. Abstract 9022.

Cheek, L.C., Pieters, C.M., 2012. Variations in anorthosite purity at Tsiolkovsky crater on the Moon. Lunar. Planet. Sci. 43. Abstract 2624.

Cheek, L. C., Pieters, C. M., 2014. Reflectance spectroscopy of plagioclase-dominated mineral mixtures: implication for characterizing lunar anorthosites remotely. Am. Min., 99, 1871-1892.

Cheek, L.C., Pieters, C.M., 2012. Variations in anorthosite purity at Tsiolkovsky crater on the Moon. Lunar. Planet. Sci. 43. Abstract 2624.

Christensen, P. R., et al., 1992. Thermal Emission Spectrometer Experiment: Mars Observer Mission, J. Geophys. Res., 97, 7719– 7734

Christensen, P. R., et al., 2004. The thermal emission system (THEMIS) for the MARS 2001 Odyssey Mission, Space Science Review, 110, 85-130

Clark, R. N., Chapter 1: Spectroscopy of Rocks and Minerals, and Principles of Spectroscopy, in Manual of Remote Sensing, Volume 3, Remote Sensing for the Earth Sciences, (A.N. Rencz, ed.) John Wiley and Sons, New York, p 3- 58, 1999.

Clark, R.N., Roush, T.L. (1984). Reflectance Spectroscopy: Quantitative Analysis Techniques for Remote Sensing Applications. J. Geophys. Res. 89, 6329-6340.

Clenet, H., et al., 2011. A new systematic approach using the Modified Gaussian Model: insight for the characterization of chemical composition of olivines, pyroxenes and olivine-pyroxene mixtures. Icarus, 213, 404-422

Clenet, H. et al., 2013. A systematic mapping procedure based on the Modified Gaussian Model to characterize magmatic units from olivine/pyroxenes mixtures: Application to the Syrtis Major volcanic shield on Mars. J. Geophys. Res. 118, 1632–1655. http://dx.doi.org/10.1002/jgre.20112

Cloutis, E. A., Gaffey, M. J., Jackowski, T.L., and Reed, K. L. (1986). Calibrations of phase abundance, composition, and particle size distribution for olivine-orthopyroxene mixtures from reflectance spectra. JGR, 91, 11641Cloutis, E.A., et al., 2008. Ultraviolet spectral reflectance properties of common planetary minerals. Icarus 197, 321–347

Cloutis, E.A., Gaffey, M.J., 1991. Pyroxene spectroscopy revisited: spectral-compositional combinations and relationships to geothermometry. J. Geophys. Res. 96, 22809-22826

Craig, M.A., Cloutis, E.A., Bailey, D.T., 2007. The effects of grain size, <45-1000 μm, on the reflectance spectrum of planetary analogs from 0.35-2.5 μm. Lunar. Planet. Sci. 38. Abstract 1356.

Crown, D.A., Pieters, C.M., 1987. Spectral properties of plagioclase and pyroxene mixtures and the interpretation of lunar soil spectra. Icarus, 72, 492-506.

Denevi, B.W., 2013. The distribution and origin of smooth plains on Mercury. JGR, 118, 89+1-907

Domingue, L., et al., 2009. Processes affecting Mercury's spectrum and color: space weathering. MBC09- The surface composition of Mercury from ultraviolet-visible-infrared spectroscopy: State of the art and future strategies- Joint thematic Workshop on Messenger-BepiColombo mission to Mercury. Programme with abstracts.

Donaldson Hanna, K. L., et al., 2014. Global assessment of pure crystalline plagioclase across the Moon and implications for the evolution of the primary crust. J. Geophys. Res. Planets. 119, doi:10.1002/2013JE004476.

Ehlmann, B.L., et al., 2011. Subsurface water and clay mineral formation during the early history of Mars. Nature, 479, 53-60

Evans, L.G., et al. 2012. Major-element abundances on the surface of Mercury: results from the MESSENGER Gamma-Ray Spectrometer. JGR, 117, doi: 10.1029/2012JE004178

Fischer, E. M., Pieters, C. M., 1994. Remote Determination of Exposure Degree and Iron Concentration of Lunar Soils Using VIS-NIR Spectroscopic Methods. Icarus, 111, 475-488, http://doi.org/10.1006/icar.1994.1158

Geminale, A. et al., 2015. Removal of atmospheric features in near infrared spectra by means of principal components analysis and target transformation on Mars: I. Method. Icarus, 253, 51-65

Gendrin, A. et al., 2005. Sulfates in martian layered terrains: The OMEGA/Mars Express view. Science 307 (5715), 1587–1591. http://dx.doi.org/10.1126/ science.1109087.

Giacomini, L., Carli, C., Sgavetti, M.,Massironi, M., 2012. Spectral analysis and geological mapping of DaedaliaPlanum lava field (Mars) using OMEGA data. Icarus, 220, 679-693

Green, R. O., et al., 2011. The Moon Mineralogy Mapper (M^3) imaging spectrometer for lunar science. Instrument description, calibration, on-orbit measurements, science data calibration and on-orbit validation. J. Geophys. Res., 116, E00G19.

Gross, J., Isaacson, P. J., Treiman, A. H., Le, L., Gorman, J. K., 2014. Spinel-rich lithologies in the lunar highland crust: linking lunar samples with crystallization experiments and remote sensing. Goldsten, J. O., et al., 2007. The MESSENGER Gamma-ray and Neutron spectrometer. Space Sci. Rev., 131, 339-391

Hamilton, V. E., Christensen, P. R., McSween, H. Y., Bandfield, J. L., 2003. Searching for the source regions of martian meteorites using MGS TES: Integrating martian meteorites into the global distribution of igneous materials on Mars. Met. & Planet. Sci., 38, 871-885

Hawke, B.R., et al., 2003. Distribution and modes of occurrence of lunar anorthosite. J. Geophys. Res., Vol. 108, doi:10.1029/2002JE001890.

Heisenger, H., Head, J., W. III, (2006). New views of lunar geosciences: an introduction and overview. Rev. in Mineralogy and Geochemistry, 60, 1-81.

Hiroi, T., et al., 2012. Diversity in the visible-NIR absorption band characteristics of lunar and asteroidal plagioclase. Lunar. Planet. Sci. 43. Abstract 1168

Hoefen, T. M., Clark, R. N., bandfield, J. L., Smith, M. D., Pearl, J. C., Christenses, P.R., 2003. Discovery of olivine in the Nili Fossae region of Mars. Science, 302-627-630. DOI: 10.1126/science.1089647

Hofmeister, A.M., Rossman, G.R., 1983. Color in feldspar. Reviews in Mineralogy 2, 271-80

Izenberg, N.R., 2014. The low-iron, reduced surface of Mercury as seen in spectral reflectance by MESSENGER. Icarus, 228, 364-374

Izenberg, N.R., et al., 2008. High-spatial-resolution visible to near-infrared reflectance of Mercury's surface obtained during the first MESSENGER flyby. Lunar. Planet. Sci. 39, 1276.

Kanner, L. C., Mustard, J. F., Gendrin, A., 2007. Assessing the limits of the Modified Gaussian Model for remote spectroscopic studies of pyroxenes on Mars. Icarus 187, 442-456.

Kato , M., Sasaki, K., Tanaka, K., Iijima, Y., Takizawa, Y., 2008. The Japanese lunar mission SELENE: Science goals and present status. Adv. Space Res., 42, 294-300

Klima, R., L., Pieters, C. M, Dyar, D. M., 2007. Spectroscopy of synthetic Mg-Fe pyroxenes I: Spin-allowed and spin-forbidden crystal field bands in the visible and near-infrared. Meteoritcs & Planetary Science, 42, 235-253

Klima, R., L., Dyar, D. M., Pieters, C. M, 2011. Near-infrared spectra of clinoyroxenes: effect of calcium content and crystal structure. Meteoritcs & Planetary Science, 46, 379-395

Kodikara, G.R.L., Champati ray P.K., Chauhan, P., Chatterjee, R.S., 2016. Spectral mapping of morphological features on the moon with MGM and SAM. International Journal of Applied Earth Observation and Geoinformation 44, 31-41

Kramer, G. Y., Kring, D. A., Mahm, A. L., Pieters, C. M., 2013. Spectral and photogeologic mapping of Schrödinger Basin and implications for post-South Pole-Aitken impact deep subsurface stratigraphy. Icarus, 223, 131-148

Kruse, F. A., et al., 1993, The Spectral Image Processing System (SIPS) - Interactive Visualization and Analysis of Imaging spectrometer Data. Remote Sensing of Environment, v. 44, p. 145 - 163.

Langevin, Y. et al., 2005. Sulfates in the north polar region of Mars detected by OMEGA/Mars Express. Science 307 (5715), 1584–1586. http://dx.doi.org/ 10.1126/science.1109091.

Laul, J.C.,Vaniman, D.T., Papike, J.J., Simon, S.B., 1978. Chemistry and petrology of size fractions of Langevin, Y. et al., 2005. Sulfates in the north polar region of Mars detected by OMEGA/Mars Express. Science 307 (5715), 1584–1586. http://dx.doi.org/ 10.1126/science.1109091.Apollo 17 deep drill core 70009-70006. Proc. Lunar Planet Sci. Conf. 9th, 2065-2097

Laul, J.C., Lepel, E.A., Vaniman, D.T., Papike, J.J., 1979. The Apollo 17 drill core: chemical systematics of grain size fractions. Proc. Lunar Planet Sci. Conf. 10th, 1269-1298

Laul, J.C.,Papike, J.J., 1980. The lunar regolith: comparative chemistry of the Apollo sites. Proc. Lunar Planet Sci. Conf. 11th, 1307-1340

Lucey, P. et al., 2006. Understanding the lunar surface and Space–Moon interactions. Rev. Mineral. Geochem. 60, 83–219.

Mangold, N. et al., 2007. Mineralogy of the Nili Fossae region with OMEGA/Mars Express data: 2. Aqueous alteration of the crust. J. Geophys. Res. 112 (E8). http://dx.doi.org/10.1029/2006JE002835

Matsunaga, T., et al., 2008. Discoveries on the lithology of lunar crater central peaks by SELENE Spectral Profiler. Geophys. Res. Let., 35, L23201, doi:10.1029/2008GL035868

McClintock, W.E., Lankton, M. R., 2007. The Mercury Atmospheric and Surface Composition Spectrometer for the MESSENGER mission. Space Science Reviews, 131, 481-521, DOI:10.1007/s11214-007-9264-5.

McClintock, W.E., et al., 2008. Spectroscopic Observations of Mercury's Surface Reflectance During MESSENGER's First Mercury Flyby. Science 321, 62-65.

McCord, T. B., Adams, J. B., 1973. Progress in remote optical analysis of lunar surface composition. The Moon 7, 453-474

McEwen A. S., Pieters, C. M., 1997. Mapping the Moon by Clementine. Adv. Space Res. 19, 1523-1533

McGuire, P.C. et al., 2009. An improvement to the volcano-scan algorithm for atmospheric correction of CRISM and OMEGA spectral data. Planet. Space Sci. 57 (7), 809–815. http://dx.doi.org/10.1016/j.pss.2009.03.007.

McKay, D.S., Fruland, R.M., Heiken, G.H., 1974. Grain size and the evolution of lunar soils. Proc. Lunar Planet Sci. Conf. 5th, 1, 887-906

Murchie, S., et al., 2007. Compact Reconaissance Imaging Spectrometer for Mars (CRISM) on Mars Reconaissance Orbiter (MRO). J. Geophys. Res., 112, E5

Mustard, J.F. et al., 2005. Olivine and pyroxene diversity in the crust of Mars. Science 307, 1594–1597.

Mustard, J.F. et al., 2007. Mineralogy of the Nili Fossae region with OMEGA/Mars Express data: 1. Ancient impact melt in the Isidis Basin and implications for the transition from the Noachian to Hesperian. J. Geophys. Res. 112 (E8). http:// dx.doi.org/10.1029/2006JE002834.

Nash, D.B., Conel, J.E., 1974. Spectral reflectance systematics for mixtures of powdered hypersthene, labradorite, and ilmenite. J. Geophys. Res. 79, 1615-1621.

Noble, S. K., Pieters, C. M., Hiroi, T., Taylor, L. A., 2006. Using the modified Gaussian model to extract quantitative data from lunar soils. JGR, 111, E11009, doi:10.1029/2006JE002721Ogawa, Y., et al., 2011. The widespread occurrence of high-calcium pyroxene in bright-ray craters on the Moon and implications for lunar-crust composition. Geophys. Res. Let. 38, L17202, doi:10.1029/2011GL048569

Ohtake M., et al., 2008. Performance and scientific objectives of the SELENE (KAGUYA) Multiband Imager. Earth, Planets and Space, 60, 257-267

Ohtake, M., et al., 2009. The global distribution of pure anorthosite on the Moon. Nature 461, doi:10.1038/nature08317

Papike, J., L. A. Taylor, and S. Simon 1991. Lunar minerals, in The Lunar Sourcebook, edited by G. Heiken, D. Vaniman, and B. French, pp. 121 – 181, Cambridge Univ. Press, New York.

Pieters, C. M. (1983), Strength of mineral absorption features in the transmitted component of near-infrared reflected light: First results from RELAB, J. Geophys. Res., 88, 9534 – 9544.

Pieters, C.M., 1986. Composition of the lunar highland crust from near-infrared spectroscopy. Rev. Geophys., 24, 557-578.

Pieters, C. M., Fischer, E. M., Rode, O., Basu, A., 1993. Optical effects of space weathering: the role of the finest fraction. J. Geophys. Res., 98, 20,817-20,824.

Pieters, C. M., 1996. Plagioclase and maskelynite diagnostic features. Lunar. Planet. Sci. 27, Abstract 1031

Pieters C.M. 1978 - Mare basalt types on the front side of the Moon. Proc. Lunar Planet. Sci. Conf. IX, 2825-2849

Pieters, C. M., et al., 2009. The Moon Mineralogy Mapper (M^3) on Chandrayaan-1. Current Science, 96, 500-505

Pieters, C.M., et al., 2011. Mg-spinel lithology: A new rock type on the lunar farside. JGR, 116, E00G08, doi:10.1029/2010JE003727

Pinet, P., et al. (2006) Detection and regional mapping of mafic minerals across Syrtis Major from OMEGA/Mars Express observations in the visible-near infrared domain by means of MGM deconvolution, paper presented at European Planetary Science Congress 2006, Eur. Planet. Network, Berlin.

Pompilio, L., 2005. Reflectance spectroscopy (VNIR) of igneous rocks: characterization of the Bjerkreim-Sokndal cumulates. PhD thesis, University of Parma

Pompilio, L., Sgavetti, M., Pedrazzi, G., 2007. Visible and near-infrared reflectance spectroscopy of pyroxene-bearing rocks: new constraints for understanding planetary surface compositions. JGR, 112, E01004, http://dx.doi.org/10. 1029/2006JE002737

Poulet, F. et al., 2005. Phyllosilicates on Mars and implications for early martian climate. Nature 438 (7068), 623–627. http://dx.doi.org/10.1038/nature04274.

Poulet, F., et al., 2007. Martian surface mineralogty from Observatoire pour la Minèralogie, l'Eau, les Glaces et l'Activitè on board the Mars Express spacecraft (OMEGA/Mex): global mineral maps. JGR, 112, doi:10.1029/2006JE002840

Robinson, M.S., et al., 2008. Reflectance and Color Variations on Mercury: Regolith Processes and Compositional Heterogeneity. Science, 321, 66.

Sasaki, S., Kurahashi, E., 2004. Space weathering on Mercury. Advances in Space Research, 33, 2152-2155.

Schlemm, C. E., II, et al. (2007), The X-Ray Spectrometer on the MESSENGER spacecraft, Space Sci. Rev., 131, 393–415, doi:10.1007/ s11214-007-9248-5

Schonfeld, E., 1981. High spatial resolution Mg/Al maps of Wester Crisium and Sulpicius Gallus regions. Proc. Lunar Planet., Sci., Conf., 12th, 809-816

Smith, J. V., et al., 1970. Petrologic history of the Moon inferred from petrography, mineralogy, and petrogenesis of Apollo 11 rocks. Proceedings of the Apollo 11 Lunar Sci. Conf., 1, 897-925.

Solomon, S.C., et al., 2001. The MESSENGER mission to Mercury: scientific objectives and implementations. Planet. Space Sci. 49, 1445-1465.

Solomon, S.C., 2003. Mercury: the enigmatic innermost planet. Earth Planet. Sci. Lett., 216, 441-7455

Solomon, S.C., et al., 2008. Return to Mercury: a global perspective on MESSENGER's first Mercury flyby. Science, 321, 59.

Serventi, G., Carli, C., Sgavetti, M., Ciarniello, M., Capaccioni, F., Pedrazzi, G., 2013. Spectral variability of plagioclase-mafic mixtures (1): effects of chemistry and modal abundance in reflectance spectra of rocks and mineral mixtures. Icarus, 226, 282-298.

Serventi, G., Carli, C., Sgavetti, M.: 2014. Laboratory analysis (reflectance spectroscopy) of terrestrial analogues. Encyclopedia of lunar science, pp. 1-9

Serventi, G., Carli, C., Sgavetti, M., 2015. Spectral variability of plagioclase-mafic mixtures (3): quantitatively analysis applying the MGM algorithm. Icarus, 254, 34-55 doi:10.1016/j.icarus.2015.03.024.

Serventi, G., Carli C., Sgavetti, M. Deconvolution of mixtures with high plagioclase content for the remote interpretation of lunar plagioclase-rich regions. Accepted on Icarus

Sgavetti, M. et al., 2015. Spectral reflectance characteristics of the Hamar Laghdad hydrothermal sequence, Morocco: Implications for the methane origin on Mars. Icarus 245, 184–197. http://dx.doi.org/10.1016/j.icarus.2014.09.027.

Sprague, A.L., Kozlowski, R.W.H., Witteborn,F.C., Cruikshank, D.P., Wooden, D.H., 1994. Mercury: Evidence for anorthosite and basalt from mid-infrared (7.3–13.5 μm) spectroscopy. Icarus, 109, 156–167

Sprague, A.L., et al., 2009. Spectral emissivity measurements of mercury's surface indicate Mg- and Ca-rich mineralogy, K-spar, Na-rich plagioclase, rutile, with possible perovskite, and garnet. Planet. Spa. Sci., 57, 364-383

Spudis, P.D., Hawke, B.R:, Lucey, P.G., 1984. Composition of Orientale Basin Deposits and Implications for the Lunar Basin-Forming Process. J. Geophys. Res., Vol. 89, 197-210

Stockstill-Cahill, K. R., McCoy, T. J., Nittler, L. R., Weider, S. Z., & Hauck, S. A. II (2012), Magnesium-rich crustal compositions on Mercury: Implications for magmatism from petrologic modeling. *J. Geophys. Res*, *117*, E00L15.

Streckeisen, A. (1976). To each plutonic rock its proper name. Earth Science Review 12, 1-33.

Sunshine, J.M., et al., 1990. Deconvolution of mineral absorption bands: an improved approach. J. Geophys. Res., Vol. 95, 6955-6966

Sunshine, J.M., Pieters, C. M., 1993. Estimating modal abundances from the spectra of natural and laboratory pyroxene mixtures using the Modified Gaussian Model. J. Geophys. Res., Vol. 98, 9075-9087

Sunshine, J.M., Pieters, C. M., 1998. Determining the composition of olivine from reflectance spectroscopy. J. Geophys. Res., Vol. 103, 13675-13688

Taylor G.J., Warren P., Ryder G., Delano J., Pieters C.M., Lofgren G., 1991 - Lunar rocks. In: Heiken G., Vaniman D.T., French B.M. (eds.), Lunar sourcebook, University of Cambridge, U.K., 183-284

Taylor S.R., 2007 - The Moon. In: McFadden L.A., Weissman P.R., Jhonson T.V. (eds.), Encyclopedia of the Solar System, second edition, Elsevier, 227-250

Taylor, A.T., et al., 2009. Lunar magma ocean crust: implication of FeO contents in plagioclase. Lunar. Planet. Sci. 40. Abstract 1304

Vilas, F., Leake, M.A., Mendell, W.W., 1984. The dependence of reflectance spectra of Mercury on surface terrain. Icarus, 59, 60-68

Vilas, F., 1985. Mercury: absence of crystalline Fe^{2+} in the regolith. Icarus, 64, 133-138

Vilas, F., 1988. Surface composition of Mercury from reflectance spectrophotometry. F Vilas, C.R Chapman, M.S Matthews (Eds.), Mercury, University of Arizona Press, Tucson (1988), pp. 59–76

Warren, P.H., 1985. The magma ocean concept and lunar evolution. Annu. Rev. Earth Planet. Sci., 13, 201-240

Weider, S, Z., et al., 2012. Chemical heterogeneity on Mercury's surface revealed by the MESSENGER X-Ray Spectrometer. JGR, 117, doi: 10.1029/2012JE004153

Wood, J.A., Dickey, J.S:, Marvin, U.B., and Powell, B.N., 1970. Lunar anorthosites and a geophysical model of the Moon. Proc. Apollo 11 Lunar Sci. Conf., 965-988.

Yamamoto, S., et al., 2010. Possible mantle origin of olivine around lunar impact basins detected by SELENE. Nature, 3, DOI: 10.1038/NGEO897

Acknowledgments
Ovviamente sto scrivendo questi ringraziamenti poche ora prima della consegna della tesi, quindi mi vorrete scusare per la brevità!

Prima di tutto vorrei ringraziare la prof. Mariolina Sgavetti, per essere una persona davvero unica, dal punto di vista lavorativo e umano. Grazie per avermi fatto appassionare ad una materia così entusiasmante, per avermi dimostrato tanta fiducia sin dall'inizio, per aver capito e supportato i miei periodi di crisi, per avermi convinta a non lasciare tutto e a continuare, ma soprattutto grazie per avermi dato la possibilità di dedicarmi alla famiglia, anche se questo ha significato dedicare meno ore al lavoro.
Grazie al Dott. Cristian Carli, per avermi spronata sempre con nuove idee e per avermi aiutata in qualsiasi momento avessi bisogno.
Grazie alla mia famiglia, alla mia mamma, al mio papà e al mio fratellone per aver fatto di tutto per darmi la possibilità di arrivare dove sono arrivata.
Grazie alle mie fedelissime compagne di avventura, la Eli e la Ari, come farò adesso senza di voi??? Come farò a stemperare la tensione con una seduta di nail art??? E soprattutto…con chi farò del sano speteguleeeesss???
Grazie alla Sere, la mia fantastica compagna di ufficio, siamo state separate parecchio in questo periodo ma adesso staremo insieme per un bel po'!!!
Grazie alla compagnia del Rancio per l'ora di svago quotidiano.
Grazie agli amici di una vita, la mia Silvietta (con la piccola Alice), il mio Gallino, la mia sempre zovine Cora e Marziolino.
E infine grazie agli uomini più importanti della mia vita, Tommaso e Marco…siete voi a darmi ogni giorno la voglia di sorridere.